NORTHWESTERN UNIVERSITY

Ionic Structure at Dielectric Interfaces

A DISSERTATION

SUBMITTED TO THE GRADUATE SCHOOL

IN PARTIAL FULFILLMENT OF THE REQUIREMENTS

for the degree

DOCTOR OF PHILOSOPHY

Field of Applied Physics

By

Yufei Jing

EVANSTON, ILLINOIS

December 2016

Abstract

Ionic Structure at Dielectric Interfaces

Yufei Jing

The behavior of ions in liquids confined between macromolecules determines the outcome of many nanoscale assembly processes in synthetic and biological materials such as colloidal dispersions, emulsions, hydrogels, DNA, cell membranes, and proteins. Theoretically, the macromolecule-liquid boundary is often modeled as a dielectric interface and an important quantity of interest is the ionic structure in a liquid confined between two such interfaces. The knowledge gleaned from the study of ionic structure in such models can be useful in several industrial applications, such as biosensors, lithium-ion batteries double-layer supercapacitors for energy storage and seawater desalination.

Electrostatics plays a critical role in the development of such functional materials. Many of the functions of these materials, result from charge and composition heterogeneities. There are great challenges in solving electrostatics problems in heterogeneous media with arbitrary shapes because electrostatic interactions remains unknown but depend on the particular density of charge distributions. Charged molecules in heterogeneous media affect the media's dielectric response and hence the interaction between the charges is unknown since it depends on the media and on the geometrical properties of the interfaces.

To determine the properties of heterogeneous systems including crucial effects neglected in classical mean field models such as the hard core of the ions, the dielectric mismatch and interfaces with arbitrary shapes. The effect of hard core interactions accounts properly for short range interactions and the effect of local dielectric heterogeneities in the presence of ions and/or charged molecules for long-range interactions are both analyzed via an energy variational principle that enables to update charges and the medium's response in the same simulation time step. In particular, we compute the ionic structure in a model system of electrolyte confined by two planar dielectric interfaces using molecular dynamics(MD) simulations and compared it with liquid state theory result. We explore the effects of high electrolyte concentrations, multivalent ions, and dielectric contrasts on the ionic distributions. We observe the presence of non-monotonous ionic density profiles leading to structure deformation in the fluid which is attributed to the competition between electrostatic and steric (entropic) interactions. We find that thermal forces that arise from symmetry breaking at the interfaces can have a profound effect on the ionic structure and can oftentimes overwhelm the influence of dielectric discontinuity. The combined effect of ionic correlations and inhomogeneous dielectric permittivity significantly changes the character of effective interaction between two interfaces. We show that, in concentrated electrolytes with confinement, it is imperative to take into account the finite-size of the ions as well as proper description of electrostatic interactions in heterogeneous media, which is not fully fulfilled by Poisson-Boltzmann based approaches.

The effect of electric field at interface between two immiscible electrolyte solutions is studied as well. The classical Poisson-Boltzmann theory has been widely used to describe the corresponding ionic distribution, even though it neglects the polarization and ion correlations typical of these charged systems. Using Monte Carlo simulations, we provide an enhanced description of an oil-water interface in the presence of an electric field without needing any adjustable parameter,

including realistic ionic sizes, ion correlations, and image charges. Our data agree with experimental measurements of excess surface tension for a wide range of electrolyte concentrations of LiCl and TBATPB (tetrabutylammonium-tetraphenylborate), contrasting with the result of the classical non-linear PoissonBoltzmann theory. More importantly, we show that the size-asymmetry between small Li^+ and large Cl^- ions can significantly increase the electric field near the liquid interface, or can even reverse it locally, at high salt concentrations in the aqueous phase. These observations suggest a novel trapping/release mechanism of charged nanoparticles at oil-water interfaces in the vicinity of the point of zero charge.

In addition, we study the effects of size asymmetry and charge asymmetry on ion distribution at a dielectric interface using coarse-grained MD based on an energy variational principle. The goal is to explore charge amplification with exact consideration of surface polarization. We find that both size asymmetry and charge asymmetry lead to charge separation at the interfaces. In addition, charge separation is enhanced by interface polarization. We are currently extending the research to charged interfaces that has broad applications such as batteries and supercapacitors for energy storage.

Acknowledgements

First and foremost, I want to thank my advisor, Professor Monica Olvera de la Cruz, for supporting me during these past five years. It has been an honor and pleasure to do my graduate research with her. I appreciate all her contributions of time, ideas, and guidance both on research and life that makes my Ph.D. life productive and exciting.

I would also like to thank my entire thesis committee, Prof. Erik Luijten and Prof. Chris Wolverton for their time, interest, and insightful suggestions Much of my success is due to the encouraging environment of the Monica Olvera de la Cruz group. I would especially thank Prof. Guillermo Iván Guerrero-García and Prof. Vikram Jadhao for mentoring my first three years at Northwestern. I was extremely lucky to have them that led me into the field. Additionally, I would like to thank my collaborators Prof. Jos Zwanikken, Dr. Meng Shen and Honghao Li. I thank them for the terrific ideas and fascinating projects they proposed to collaborate with me. Many thanks as well to Prof. Prateek Jha, Dr. Baofu Qiao, Dr. Kevin Kohlstedt, Prof. Charles Sing, Dr. Arjan Quist, Prof. Zhenwei Yao, Dr. Rebecca McMurray, Dr Neils Boon, Shuangping Liu, Dr. Joshua Dempster, Dr. Victor Pryamitsyn, Dr. Mykola Tasinkevych, Dr. Trung Nguyen, Dr. Aykut Erbas, Dr. Jaime Andres Millan, Dr. Kyle Hoffmann, Dr. Pablo Vazquez Montejo, Ha-Kyung Kwon, Dongxu Huang, Jack Edelbrock, Martin Girard, Yaohua Li, Debadutta Prusty, Boran Ma and Saijie Pan, for all the help and joy they gave me.

Last but not least, I want to thank my parents and my brother for their endless love, support, and understanding. My fiancé, Dr. Tian Jiang, shines her joyfulness and optimism on me every day.

Contents

List of Tables

List of Figures

CHAPTER 1

Introduction

1.1. Background and Motivation

The assembly of molecules and nanopariticles into robust nanostructures to perform specific functions is an exceptionally active and rapidly expanding field in science. Nature utilizes charged molecules and ions to self-assemble its components into structures that spontaneously adopt various shapes to carry out important functions[**7**]. Indeed, ions and charged molecules are responsible of the organization and functions of various synthetic materials and biological systems. Molecules with electrical charges self-assemble into structures with diverse symmetries by unknown mechanisms. The understanding of assembling paradigms that determine the shape and composition through tuning chemical and physical interactions using electrostatics should then enable the design of inhomogeneous structures for various technological applications.

Many biological materials such as DNA and proteins as well as synthetic systems such as colloidal dispersions, polymeric gels, and emulsions are immersed in liquids that inhabit charged objects among which the most abundant are salt ions [**8, 9**]. In biology, the presence of these salt ions controls a variety of processes. For example, calcium ions play a key role in the pumping action of the heart and concentration gradients of sodium and potassium ions help control nerve signaling [**10, 11**]. On the other hand, electrolyte ions help drive key processes involved in the generation and function of many synthetic materials such as the stabilization of colloidal dispersions and emulsions [**12, 13, 14**], morphological changes in hydrogels [**15**], and pattern formation

in nanostructures [**16, 17**]. Further, in some synthetic systems such as dielectric elastomers and supercapacitor devices, in addition to the charged macromaterial, counterions and salt ions, external electric fields are present. The electric field has been related to the proper performance of biological functions at the cellular level[**18, 19**], displaying the ability to accelerate or improve wound healing when it is applied externally[**20**]. The knowledge of the electric field at liquid interfaces is also crucial for the development of enhanced devices to store energy safely and efficiently, such as double layer supercapacitors[**21**], or to improve the ion transfer and electro-assisted solvent extraction of metal ions from wastewater and industrial fluids[**22**].

The enormously increasing applications indicate the importance of electrostatics in developing new materials. Besides the role of electrostatics in the development of membranes for water filtration[**23**], fouling-resistant surfaces for the preparation of filtration membranes[**24**], nucleotide functionalized gold nanoparticles for diagnostic and therapies[**25, 26**], complexes for drug delivery and gene therapy[**27**] and nanogels for drug delivery[**28**], new applications include the fabrication of lithium-ion batteries[**29, 30**] and transistors[**31, 32**]. Much of the new functions of these materials derived by the development of charge heterogeneities. Therefore, understanding the charge distributions in complex electrolytes solution can provide guidance to generate novel functional materials.

Electrostatic interactions drives the assembly of oppositely charged molecules into structures which properties can be tuned by changing the ionic concentration[**33, 34, 35, 36, 37, 38, 39, 40, 41**]. Knowledge of ionic distributions near such liquid-liquid or liquid-solid interface is useful to examine a variety of processes in the biological context as well as in physicochemical processes. The structural and functional properties of many biological macromolecules like DNA and ion channel proteins are fundamentally affected by the distribution of counterions and salt ions near the macromolecule surface. Similarly, the stabilization of synthetic soft materials such as colloidal

dispersions and oil-water emulsions is governed by the ionic structure surrounding the colloid-solvent and oil-water interfaces. In hydrogels and thin shells, this soft structure can be tuned by varying the pH or salt concentration which often gives rise to interesting phenomena like swelling of gels and faceting in the latter case. Therefore, investigation of the properties of these soft-matter systems requires an accurate description of the ionic structure.

There are great challenges in solving electrostatics problem in complex electrolytes computationally. Basically, detailed atomistic description are more accurate but limited to computational costs. Therefore, it is necessary to develop a coarse-grained scheme that is detailed enough to capture relevant physical processes while still possible to simulate. The so-called primitive model for electrolytes is widely used, where the electrolytes media can be treated in the continuum approximation and the ions are treated as discrete particles. In this framework, the long-range interaction between charges depends on the dielectric media that host these charges, and the way the media respond to these charges depends on where the charges are located. For point-ions restricted to one uniform medium, it is easy to obtain the medium's dielectric response and hence the interaction between the ions (Coulomb's law). However, in real situations in biology and materials there are more than one medium, whose dielectric properties differ from one another, forming interfaces and harboring ions. For example, in biology, proteins and complexes are surrounded by ionic solution and cell membranes separating intracellular media with different dielectric responses. Similarly many soft materials, such as charged nanoparticles or colloidal dispersions in salty solutions and gels of charged molecules, exhibit the situation where two or more different dielectric media form an interface with ions embedded in the media.The computational challenge is that the electrostatic polarization due to dielectric heterogeneity requires to solve the Poisson equation at each time step. Determination of the polarization field through analytical solution of Poisson equation is very difficult which are known only for specific simple geometries. For more general cases, these

many charged molecules in heterogeneous media the media's dielectric response and hence the interaction between the charges is unknown since it depends on the media and on the geometrical properties of the interfaces that media form. A suitably designed approach is needed to avoid explicitly solving the Poisson equation.

1.2. Theoretical models

Theoretically, an accurate extraction of electrolytes solution begins with the choice of the coarse-grained model to represent the associated real system. The primitive model is commonly used as mentioned above, where the constituent macromolecules and the solvent fluids are both considered as dielectric continua harboring charged particles such as ions or charged micromolecules and separated by thin boundaries. In many situations, the dielectric response of the macromolecule is different from the surrounding solvent medium which often affects the distribution of the ions near the macromolecule-solvent interface. It is crucial to include this dielectric heterogeneity in the calculation of the ionic structure as has been revealed by several recent studies[**42, 5, 43**]. The effect of polarizability that arise when ions reside in heterogeneous dielectric media is included as shown in Fig. 1.1.

The thermodynamic Debye and Hückel (DH) theory of electrolytes identify the mean electrostatic potential around an ion with the potential of mean force, which presumes negligible fluctuations. The theory includes many body interactions due to its self-consistent character, but assumes negligible ionic radius. Also, the theory is often approximated to the well known DH limiting law, where the Poisson-Boltzmann equation is linearized and mean activity coefficient is proportional to the square root of the ionic strength. DH theory appears to be accurate at millimolar concentrations in 1:1 aqueous electrolyte solutions, and deviations occur at higher concentrations and with electrolytes that produce ions of higher charges, particularly unsymmetrical electrolytes. It

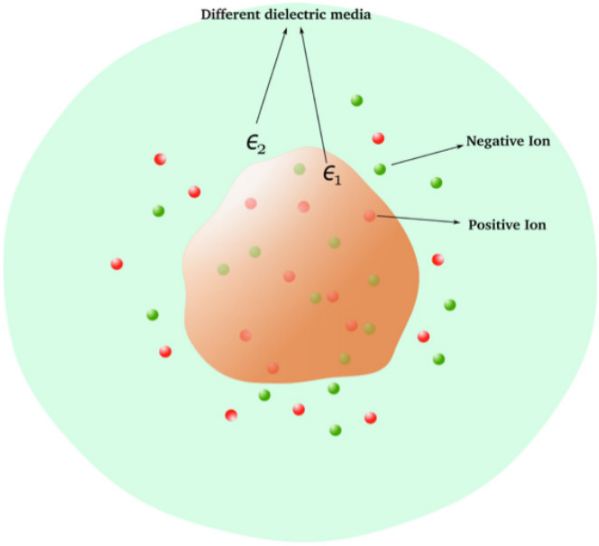

Figure 1.1. Ions in dielectric heterogenous media

is now well established that ionic distributions obtained from mean-field approaches based on the Poisson-Boltzmann theory that ignore the finite size of the ions can not be trusted; this is especially true in cases where multivalent ions (Calcium, Magnesium) are involved and for high values of salt concentrations. Thus theoretical and computational methods that incorporate the finite size of the ions and dielectric inhomogeneities in the system are likely to provide reasonably accurate results for the ionic structure near the soft interface of interest.

Our group compute the equations of state and phase coexistence of concentrated electrolyte solutions with a Debye-Hückel approach, where the self-consistent mean potential is obtained from the nonlinear Poisson-Boltzmann equation[**44**]. The non-linearized DH theory includes the effect of Bjerrum pairs, and predicts a coexistence between two dilute phases, and a critical temperature at micromolar concentrations, which might have implications for charged colloids and nanoparticles suspensions that involve organic solvents or multivalent salt ions. The equation of state within the full (non-linearized) DH theory, is practically invariant under the explicit inclusion of Bjerrum pairs, thus treats the effect of ion pairing in a consistent way, and reveals that the full DH theory

may be accurate for moderately dilute organic 1-1 electrolyte solutions, or for aqueous multivalent electrolyte solutions, which are characterized by strong couplings between the ions. Non-linear DH theory is used to estimate the cohesive effect of ion correlations on the effective interactions between nanoparticles, and in charged colloids.

For general charged systems, one of the major difficulties in simulation is to accurately measure the effects of dielectric medium on the charges and similarly the effects of charges on the medium's dielectric response. In a MD simulation, for example, only after one correctly figures out these coupled charge-medium interactions can the charge configuration be propagated. Typically, such information comes at the expense of computational costs that go into the solving of the Poisson equation, at each time step of the simulation. Our group has showed that such an explicit solution of the Poisson equation can be entirely avoided in simulations by adopting a suitably designed variational approach; thus leading to tremendous speed-ups in computing[**42**].

Variational principles are important in the investigation of large classes of physical systems. They can be used both as analytical methods as well as starting points for the formulation of powerful computational techniques such as dynamical optimization methods. Systems with charged objects in dielectric media and systems with magnetically active particles are important examples. In these examples and other important cases, the variational principles describing the system are required to obey a number of constraints. These constraints are implemented within the variational formulation by means of Lagrange multipliers. Such constrained variational formulations are in general not unique. For the application of efficient simulation methods, one must find specific formulations that satisfy a number of important conditions. An often required condition is that the functional be positive-definite, in other words, its extrema be actual minima. We developed a general approach to attack the problem of finding, among equivalent variational functionals, those that generate true minima. This method is based on the modification of the Lagrange multiplier

which allows us to generate large families of effective variational formulations associated with a single original constrained variational principle.

How to obtain variational formulations with extrema that are always minima is demonstrated in Ref. [**42**]. The electrostatic problem is formulated as an energy minimizing problem by constructing an energy functional of the polarized charge density induced by the free charges in medium. This functional allowed us to design a Car-Parrinello molecular dynamics(CPMD) scheme that enabled simulations of charges near a rigid interface of arbitrary shape[**45**] as compared to the conventional approach. In this redesigned MD simulation, instead of solving the Poisson equation, polarized charge is updated on on-the-fly, in tandem with the energy-conserving update of the charge configuration; thus bypassing all the effort that goes in the explicit solving of the differential equation.

1.3. Thesis work methodology

The new energy variational principle that enables us to update charges and the medium's response in the same simulation time step is derived in ref.[**42**]. We introduce a variational formulation of electrostatics that produced an energy functional of the polarization charge density given by

$$
\begin{aligned}
I[\omega] = & \frac{1}{2} \iint \rho_{\mathbf{r}} G_{\mathbf{r},\mathbf{r}'} \left(\rho_{\mathbf{r}'} + s[\omega] \right) d^3r' d^3r \\
& - \frac{1}{2} \iint s[\omega] G_{\mathbf{r},\mathbf{r}'} \left(\omega_{\mathbf{r}'} - s[\omega] \right) d^3r' d^3r,
\end{aligned}
\tag{1.1}
$$

where ω is the polarization charge density and $s[\omega]$ is both a functional of $\omega(\mathbf{r})$ and a function of $\mathbf{r}$, and is defined as

$$s[\omega] = \nabla \cdot \left(\chi_{\mathbf{r}} \nabla \int G_{\mathbf{r},\mathbf{r}'} \left(\rho_{\mathbf{r}'} + \omega_{\mathbf{r}'} \right) d^3 r' \right). \tag{1.2}$$

In the above equations χ is the susceptibility of the medium, ρ is the free charge density, and $G(\mathbf{r}, \mathbf{r}') = |\mathbf{r} - \mathbf{r}'|^{-1}$ is the Green's function in free space. We assumed that the medium polarization obeys linear response and also assumed the existence of Dirichlet boundary conditions, which are standard approximations for constructing electrostatic free energy functional. $I[\omega]$ is applicable to any configuration of free charges and works for arbitrary spatial variation in dielectric response.

We now consider the problem where charges are present in a dielectric that is only uniform in pieces and the pieces being separated by sharp boundaries. In other words, we have regions of space separated by infinitely thin interfaces such that each region acts as a uniform dielectric, but with a different permittivity as relative to its neighbor. Note that the interface is allowed to assume arbitrary geometry. Although this is just the next level of complexity to the uniform dielectric case, it is already a theoretically challenging problem for reasons discussed above.

In many cases, it is a reasonable assumption to represent the real system by a coarse-grained model where regions of different dielectric response are separated from each other by interfaces with negligent thickness. The functional $I[\omega]$ derived in ref works for any medium with linear but spatial variable dielectric response. but For example, in the problem of colloids in a polar solvent, modeling the colloid as one uniform dielectric continuum and the surrounding solvent as another uniform dielectric of different permittivity provides a good representation of the real system. Other examples where coarse-graining of this kind is often employed include: oil-water emulsions and biopolymers,such as lipid bilayers, in aqueous solution. We only consider the application of our

functional to the problem of ions present in a system exhibiting this piecewise-uniform dielectric response. We show that for this specific dielectric response the functional $I[\omega]$ reduces to a functional with only the interfacial induced charge density as the variational field.

In the case of different dielectric media separated by sharp interfaces $\mathcal{I}$, such that the gradient of permittivity vanishes everywhere except at the interface $\mathcal{I}$. We model the charges as point charges, with the density of charges given by

$$\rho(\mathbf{r}) = \sum_{i=1}^{N} q_i \delta\left(\mathbf{r} - \mathbf{r_i}\right) \tag{1.3}$$

for a system consisting of N charges. This problem of point charges near an arbitrarily shaped interface separating dielectrics of different permittivities, will be referred to the different dielectric problem. In the rest of this section and in appendix, the specific form of our functional for the different dielectric problem is dereived.

The derivation begins by identifying two distinct sources of induced charges in different dielectric problem. The first source comes from the point charges themselves. The contribution from this source to the total induced charge density is in fact known analytically. The second (and only other) source for induced charges is the discontinuity at $\mathcal{I}$ of the normal component of the electric field, which is itself brought about by the non-vanishing permittivity gradient at the interface. These induced charges reside only on $\mathcal{I}$ and their magnitudes are in general not known.Thus the total induced charge density splits into a known part, $\omega_{\mathcal{P}}(\mathbf{r})$, that is present on the point charges and an unknown part, $\omega_{\mathcal{I}}(\mathbf{r})$, which is located at the interface:

$$\omega(\mathbf{r}) = \omega_{\mathcal{P}}(\mathbf{r}) + \omega_{\mathcal{I}}(\mathbf{r}). \tag{1.4}$$

$\omega_{\mathcal{P}}(\mathbf{r})$ is analytically available:

$$\omega_{\mathcal{P}}(\mathbf{r}) = -\frac{\epsilon(\mathbf{r}) - 1}{\epsilon(\mathbf{r})}\rho\left(\mathbf{r}\right), \tag{1.5}$$

where $\epsilon(\mathbf{r})$ is the local dielectric constant around the charge that is located at $\mathbf{r}$. $\omega_{\mathcal{I}}(\mathbf{r})$ is in general unknown. However, since the interface $\mathcal{I}$ is a two-dimensional manifold and $\omega_{\mathcal{I}}(\mathbf{r})$ vanishes everywhere except on this surface $\mathcal{I}$, one can express $\omega_{\mathcal{I}}(\mathbf{r})$ as a surface integral:

$$\omega_{\mathcal{I}}\left(\mathbf{r}\right) = \int_{\mathcal{I}} \omega_S\left(\mathbf{r}\right)\delta\left(\mathbf{r}-\mathbf{s}\right)d^2s, \tag{1.6}$$

where ω_S is the unknown surface induced charge density. Then we get

$$\begin{aligned} s[\omega](\mathbf{r}) =& \chi\left(\mathbf{r}\right)\nabla_r^2 \int G\left(\mathbf{r},\mathbf{r}'\right)\left(\rho\left(\mathbf{r}'\right)+\omega\left(\mathbf{r}'\right)\right)d^3r' \\ &+ \nabla\chi\left(\mathbf{r}\right)\cdot\nabla_r \int G\left(\mathbf{r},\mathbf{r}'\right)\left(\rho\left(\mathbf{r}'\right)+\omega\left(\mathbf{r}'\right)\right)d^3r', \end{aligned} \tag{1.7}$$

which simplifies to

$$s[\omega](\mathbf{r}) = \frac{1-\epsilon\left(\mathbf{r}\right)}{\epsilon\left(\mathbf{r}\right)}\rho\left(\mathbf{r}\right) + \nabla_s\cdot\left[\chi\left(\mathbf{r}\right)\nabla_s\left(\int G\left(\mathbf{s},\mathbf{r}\right)\frac{\rho\left(\mathbf{r}\right)}{\epsilon\left(\mathbf{r}\right)}d^3r + \int G\left(\mathbf{s},\mathbf{s}'\right)\omega\left(\mathbf{s}'\right)d^2s'\right)\right]. \tag{1.8}$$

We define

$$\Omega\left(\mathbf{s}\right) = \nabla_s\cdot\left[\chi\left(\mathbf{r}\right)\nabla_s\left(\int G\left(\mathbf{s},\mathbf{r}\right)\frac{\rho\left(\mathbf{r}\right)}{\epsilon\left(\mathbf{r}\right)}d^3r \; + \int G\left(\mathbf{s},\mathbf{s}'\right)\omega\left(\mathbf{s}'\right)d^2s'\right)\right] \tag{1.9}$$

Considering

$$\epsilon\left(\mathbf{r}\right) = 1 + 4\pi\chi\left(\mathbf{r}\right), \rho\left(\mathbf{s}\right) = 0, \nabla\chi\left(\mathbf{r}\right) = 0 \text{ unless } \mathbf{r} = \mathbf{s},$$

the variational formulation (1.1) can be further simplified using (1.8)

$$
\begin{aligned}
I[\omega] = &+ \frac{1}{2}\iint \rho(\mathbf{r})\, G(\mathbf{r},\mathbf{r}')\, \frac{\rho(\mathbf{r}')}{\epsilon(\mathbf{r}')} d^3r d^3r' + \frac{1}{2}\iint \frac{\rho(\mathbf{r})}{\epsilon(\mathbf{r})} G(\mathbf{r},\mathbf{s})\, \Omega(\mathbf{s})\, d^3r d^2s \\
&- \frac{1}{2}\iint \frac{1-\epsilon(\mathbf{r})}{\epsilon(\mathbf{r})} \rho(\mathbf{r})\, G(\mathbf{r},\mathbf{s})\, \omega(\mathbf{s})\, d^3r d^2s - \frac{1}{2}\iint \Omega(\mathbf{s})\, G(\mathbf{s},\mathbf{s}')\, \omega(\mathbf{s}')\, d^2s d^2s' \\
&+ \frac{1}{2}\iint \Omega(\mathbf{s})\, G(\mathbf{s},\mathbf{s}')\, \Omega(\mathbf{s}')\, d^2s d^2s'.
\end{aligned} \tag{1.10}
$$

$I[\omega]$ gives the correct $\omega(\mathbf{r})$ when extremized and is an energy functional, thus becoming an ideal choice for a computational scheme employing dynamical optimization ideas. The particular forms for the functional in the case of one, two or more sharp, arbitrary shaped dielectric interfaces are shown in the Appendix A.

1.4. Relevant works on ionic structures

For electrolytes under confinement associated with dielectric heterogeneities, excluded volume effect is need for computing the accurate ionic distributions. Based on the work by Kjellander and Marčelja [**46, 47**], a theoretical approach is to evaluate the Ornstein-Zernike equation with the (anisotropic) hypernetted chain closure. It is employed recently to study the fluid structure in planar confinement.

In ref.[**4**], hard-sphere fluid is confined between two parallel hard interfaces. The anisotropic pair distribution of the fluid is analyzed using first-principles statistical mechanics of inhomogeneous fluids. Spatial confinement induces anisotropy in the pair correlations and modifies the fluids' density fluctuations, resulting in anisotropic structure factors(Fig. 1.2). When the distance between the confining surfaces is increased, an alternating sequence of strongly anisotropic versus more isotropic local order is observed. This observation highlights the importance of studying fluids under confinement.

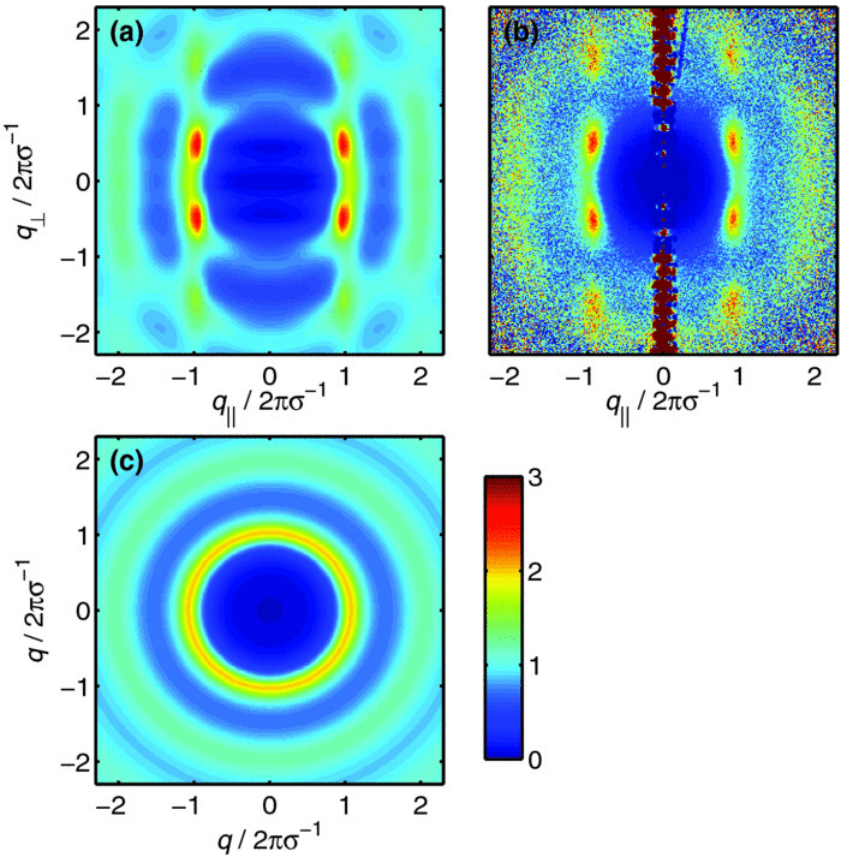

Figure 1.2. Anisotropic structure factor for a hard-sphere fluid confined between hard planar surfaces. (a) Theoretical and (b) experimental $S(q_\perp, q_\parallel)$ are shown for a reduced slit width of $L = 2.10\sigma$ and bulk number density $n_0 = 0.75\sigma^{-3}$. The dark red feature at $q_\parallel = 0$ in the experimental data is diffraction from the confining channel array, which should be neglected in the comparison. The experimental data are taken from Ref.[**3**]. (c) The corresponding isotropic bulk $S(q)$ for $n_0 = 0.75\sigma$ [**4**].

In Ref. [**5**], both the short-range repulsions and electrostatic forces are taken into consideration. The structure changes near polarizable interfaces and causes diverse attractions between confining walls. In electrolytes, the mean force caused by Coulomb interaction is induced by the anisotropic screening cloud around an ion near interfaces. In bulk, the cloud should be spherical on average, and its point of central charge should coincide exactly with the center of the ion. When close to the boundary, the ionic cloud symmetry breaks because of the geometric constraints or energetic considerations if the boundary has excess charge or an external field is applied. As a result, the

point of central charge may shift. For dielectric boundary, the polarization charge deform the screening cloud further more. For monovalent ions (green dashed line in Fig. 1.3), net forces caused by the anisotropic screening of ions is discovered, which enhanced or counteracted by the Coulomb force of induced charge of the dielectric boundary significantly. This phenomena cannot be recovered by traditional mean-field theories. In general, any boundary that breaks the symmetry in the geometric or energetic landscape changes the local ordering of ions that changes the ionic structure dramatically.

1.5. Outline of research

The objective of my thesis research is to develop MD simulation techniques designed specifically to efficiently simulate charges in the presence of inhomogeneous dielectric response and accurately extract the density profiles. The background and motivation of the project is reviewed in first two sections of Chapter 1. The original work begins in the methodology part in Chapter 1 by introducing an energy functional of the induced charge density that enables the replacement of the expensive solution of the Poisson equation at each simulation step with an on-the-fly computation of polarization effects. I have expand the functional for multiple arbitrary interfaces by writing the explicit forms of the functional. In Chapter 2, the functional is employed to successfully compute the ionic structure in a model system of electrolyte confined by two planar dielectric interfaces using MD simulations with liquid state theory verification. The effects of high electrolyte concentrations, multivalent ions, dielectric contrasts, and external electric field on the ionic distributions is also explored. In the following Chapter 3, using Monte Carlo simulations, an enhanced description of an oil-water interface in the presence of an electric field without needing any adjustable parameter is provided, considering realistic ionic sizes, ion correlations, and image charges. It agrees with experimental measurements of excess surface tension, contrasting with the

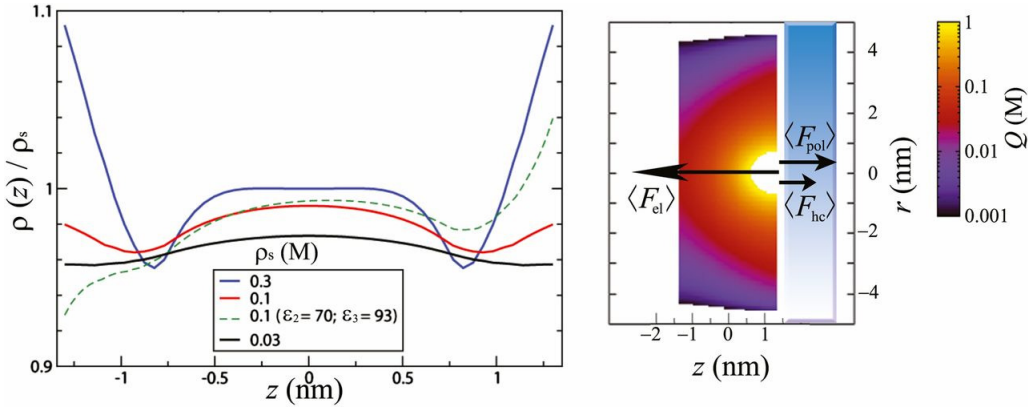

Figure 1.3. The normalized density of monovalent ions between two neutral, nonpolarized boundaries is shown in Left for several values of the reservoir concentration s (black, red, and blue at$\rho_s = 0.03M$, $0.1M$ and $0.3M$, respectively). The green dashed line corresponds to the density of monovalent ions between two dielectric discontinuities, with $\epsilon_2 = 70$, $\epsilon_3 = 93$, and $\rho_s = 0.1M$. At low densities, depletion near the boundaries is visible over a range of the order of the Debye length because of the anisotropic screening cloud that pulls ions away from the boundary. The subtle increase in density near contact at $\rho_s = 0.1M$ is a signature of hard-core correlations that tend to push ions against the walls, which are caused by anisotropic collisions. At densities above 0.3 M, the accumulation completely overcomes the depletion, and the Gibbs adsorption becomes positive. The green dashed curve shows additional effects caused by polarization; the right boundary attracts ions because of its polarization charge of opposite sign, whereas the left boundary repels the ions because of its polarization charge of similar sign. The local charge density around an anion at the right boundary is shown in Right, corresponding to the system with the two dielectric discontinuities and $\rho_s = 0.1M$ (green dashed lines) with an illustration of the mean forces that act on the ion. The screening cloud around an ion becomes anisotropic near the boundary because of geometric constraints and generates a mean force away from the boundary, which becomes relevant at distances shorter than the typical Debye length. The anisotropic collisions (short-range repulsions) cause a mean force to the wall within a distance of a few particle radii. The induced polarization charge generates a force directed away or to the wall, depending on the dielectric contrast, and is typically of slightly shorter range than the force induced by the anisotropic screening cloud. The typical range of the correlation functions in the direction parallel to the boundaries increases near the boundaries and is more affected by the geometry rather than the dielectric properties of the wall [**5**].

result of the classical non-linear Poisson-Boltzmann theory. The size-asymmetry between small cations and large anions can significantly increase the electric field near the liquid interface, or can even reverse it locally, at high salt concentrations in the aqueous phase. Chapter 4 discusses the effects of size asymmetry and charge asymmetry on ion distribution at a dielectric interface using

coarse-grained MD developed in Chapter 2. The goal is to explore charge amplification with exact consideration of surface polarization. In the end, Chapter 5 concludes with some recommended or undergoing future directions based on a summary of the models developed and results found in this thesis.

CHAPTER 2

Ionic structure in liquids confined by dielectric interfaces

2.1. Introduction

Electrostatic interactions drives the assembly of oppositely charged molecules into structures which properties can be tuned by changing the ionic concentration [**33, 34, 35, 36, 37, 38, 39, 40, 41**]. Charged gels generate patterns in aqueous solutions[**48, 49, 50**] by external changes of temperature and/or ionic concentration changes via pH, salt or osmotic pressure variations [**51, 52, 53, 54**], and electric field[**55**]. The physical properties of these heterogeneous hydrogels resemble those of biological chromosomes[**56**]. In particular, chromosomes and hydrogels undergo hypercondensation and decondensation re-entrant transitions observed when the concentration of divalent salt concentration increases.

The structure of the ion-containing liquid near charged or neutral materials determines how they assemble and interact, and often modifies their functional properties. The knowledge of this so-called soft, ionic structure is exploited in designing double-layer supercapacitor for energy storage [**57, 58**], stabilizing inks and paints, in water desalinization, and in the extraction of metal ions from wastewater [**59**]. It is thus crucial to extract this soft, ionic structure associated with the fluid near a relatively rigid object such as a colloid or a biological macromolecule. Therefore the computation of ionic structure has been the focus of recent experiments and theoretical studies [**60, 61, 62, 42, 5, 63, 64, 57, 43**].

Theoretically, the real system of macromolecules in an ion-containing liquid is often modeled in the following approximate way. The first approximation is to treat both the macromolecules

and the surrounding liquid (solvent) as continuous media, thus removing the discrete character associated with their constituents. To account for the polarizabilities of the macromolecules (say a colloid, protein, or oil droplet) and the surrounding solvent (often water), the continuous medium is characterized with a dielectric constant, which often leads to a model system where the permittivity is only piecewise-uniform due to the differences in the dielectric permittivities of the macromolecules ($\epsilon \sim 2 - 10$) and the surrounding solvent ($\epsilon \sim 80$). In the case when the density of macromolecules is high, the ionic structure is deformed as a result of the enhanced proximity of the macromolecules. In this scenario, the appropriate model to study involves an ion-containing liquid confined between two interfaces which represent the boundaries between macromolecule and the liquid medium.

The small distance between the interfaces leads to the competition between inter-ionic electrostatic interactions and hard-core or steric interactions between the ions and the interfaces and between the ions themselves. Considering the difference in sizes between the macromolecules and the associated ions, it often suffices to treat the interfaces as planar. Also, owing to the narrowness of the gap between the interfaces, it becomes imperative to take into account the finite-size of the ions in the theoretical investigation. This model of ions of a finite, fixed diameter moving in a continuum solvent confined between two planar dielectric interfaces is useful in analyzing several properties of the aforementioned biological and synthetic materials and has been employed in several recent studies [**65, 60, 5, 66**]. Working with this model approximation, a quantity of interest is the ionic distribution (which encodes the structural information) within the confined liquid for various electrolyte concentrations, stoichiometric ratios, ion sizes, interfacial dielectric contrasts, gap between the interfaces, and presence of external electric field. Another important investigation is the study of how this soft ionic structure arrives at its equilibrium conformation and how it evolves

dynamically in response to a change in external parameters such as pH, temperature or tuning of the electric field or dielectric contrast.

The presence of multiple interfaces and associated dielectric heterogeneities, and the necessity to suspend the assumption of point-size ions often complicates computing the desired ionic distributions. On the simulation side, while incorporating the finite size of the ions is relatively straightforward, treating the inhomogeneous dielectric response amounts to explicitly solving the Poisson equation at every step of the simulation in order to propagate the ionic degrees of freedom, which leads to very high computational costs. On the analytical side, while including the spatially-dependent permittivity function is relatively straightforward, taking into consideration the correlations between the ions presents serious challenges and computational costs raised by the evaluation of the required anisotropic pair-correlation functions. Due to these difficulties, many simulation studies of ionic structure near interfaces assume dielectric homogeneity and theoretical approaches that go beyond mean field or Poisson-Boltzmann theory often retain the assumption of a structureless fluid of ions, with strong coupling corrections limited to a thin boundary layer. At the same time, recent research efforts have also focused on alleviating these problems and accurately extracting the ionic structure by developing sophisticated simulation procedures [**67, 68, 69, 42, 45, 70, 71, 43**] and advanced theoretical methods [**46, 47, 5, 60, 4, 72, 73, 74, 75**].

In this article, we carry out a systematic study of ionic structure in an electrolyte solution confined by two planar dielectric interfaces (see Fig. 2.1) using molecular-dynamics-based simulations and liquid state theory. We study the effects of the competition between electrostatic and steric interactions by evaluating the profiles for different ion concentrations. We evaluate the role of ion correlations [**76, 77, 78, 79, 80**] in determining the ionic structure by considering electrolytes with different stoichiometric ratios (1:1, 2:1, 3:1). We also investigate in detail the role of dielectric mismatch at the interface by considering a variety of values for the permittivities in

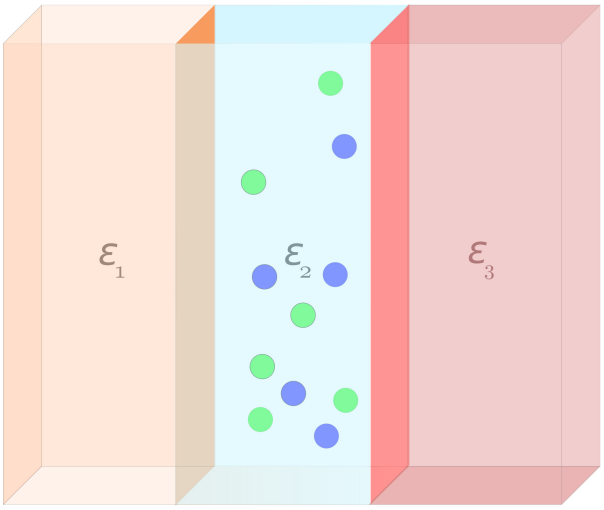

Figure 2.1. Sketch showing three uniform dielectric regions of permittivities ϵ_1, ϵ_2, ϵ_3 separated by two sharp planar interfaces. The figure also shows the presence of finite-sized positive (blue) and negative (green) ions in the medium confined between the two interfaces. In the case of dielectric mismatch, the interfaces carry polarized charge. Coarse-grained models of this kind are often employed to study effective interactions between two bio-macromolecules or colloidal particles.

the three regions (ϵ_1, ϵ_2, and ϵ_3; see Fig. 1). The effects of an external electric field on deforming the ionic structure are also studied. The case of zero dielectric contrast at both interfaces is simulated with standard molecular dynamics simulations. For the simulation of ions in media with piecewise-uniform dielectric response, we employ a recently developed MD method based on the Car-Parrinello idea[**81**] of dynamical optimization that allows for a faster, accurate, and stable computation of dielectric effects via an on-the-fly evaluation of the induced charge at the dielectric interfaces [**42, 45**]. On the theoretical front, we evaluate the Ornstein-Zernike equation with the (anisotropic) hypernetted chain closure (AHNC), based on the work by Kjellander and Marčelja [**46, 47**], which has been applied recently to extract the fluid structure in confined geometries [**5, 4**].

2.2. Model and Methods

2.2.1. Model

Our model system consists of an electrolyte solution confined within two planar surfaces (interfaces) parallel to each other (see Fig. 2.1) [**82, 76**]. The surfaces are also uncharged, that is, we do not consider any free charges residing on the surface (except for the case where we introduce a uniform electric field that can be considered as arising from the presence of free charges on the two interfaces).The surfaces themselves are considered to be infinite in extent. Two scenarios are examined in detail. First, we model the interfaces as unpolarizable which allows us to isolate the roles of interionic steric interactions, ion-interface steric interactions, and ion-ion electrostatic interactions in determining the ionic density distribution in the solvent confined within the interfaces. Second, we model the scenario where the two interfaces can get polarized due to differences in dielectric response of the media they separate. Further, we note that our system is closed, in other words, it is not in contact with an electrolyte reservoir. We highlight the role that induced charges at the interfaces play in deforming the ionic structure confined within the interfaces.

We choose $z = -H/2$ and $z = H/2$ planes as the interfaces and define H as the separation between them. For all the systems we study, $H = 3$ nm. We denote the $z = -H/2$ plane as interface I and $z = H/2$ plane as interface II. We often refer to interfaces I and II as left and right interface respectively. We consider impermeable interfaces, that is, no transport of ions is allowed across the interface. In all cases, we consider the solvent confined within the planar interfaces (interior medium) to be water. In our simulations, the ions are modeled as (soft) spheres of radius σ that interact via a purely repulsive Lennard-Jones (LJ) potential. We choose $\sigma = l_{\mathrm{B}}/2 = 0.357$ nm, where l_{B} is the Bjerrum length in water at room temperature. In our theoretical calculations, the ions are modeled as hard spheres of the same radius σ. For both methods of study, we model

the interaction between an ion and the interface via the purely repulsive LJ potential. The ions also interact with each other and with the interface, in the case when the latter is polarizable, with a Coulomb potential. For unpolarizable interfaces, the Coulomb potential energy between two ions is given by: $U_C = q_i q_j l_{\rm B}/r_{ij}$, where q_i and q_j are respectively the charges on the ion i and ion j, and r_{ij} is the distance between those ions.

We consider both symmetric and asymmetric electrolytes and study the following stoichiometric ratios (z_+:z_-) – 1:1, 2:1, 3:1, and 0:0. Note that all our ions have identical sizes; we do not take into account possible differences in ionic sizes, for example, between a monovalent anion and a trivalent cation. The 0:0 study corresponds to a simulation with only LJ interactions and acts as a reference case aiding in the comparison between the effects of Coulomb interaction against the steric interactions. We perform simulations for average negative (monovalent) ion concentrations of 0.1, 0.5, and 0.9 M. In all cases, the ions are present in the interior dielectric medium (water) with permittivity $\epsilon_2 = 80$. For the study of unpolarizable interfaces, the medium left to the interface I (left dielectric with permittivity ϵ_1) and the medium right to the interface II (right dielectric with permittivity ϵ_3) are taken to be water and we have $\epsilon_1 = \epsilon_2 = \epsilon_3 = 80$. For the study of polarizable interfaces, we study three cases ($\epsilon_1|\epsilon_2|\epsilon_3$): $20|80|20$, $20|80|160$, and $40|80|10$. All simulations and theoretical calculations are performed at room temperature $T = 298$ K.

Unless otherwise stated, we express lengths in the units of σ – the ionic radius in our model ($= 0.5 l_{\rm B}$). The unit of energy is $k_{\rm B}T$ where $k_{\rm B}$ is the Boltzmann constant, and the unit of mass is chosen to be the ionic mass m. In these reduced units, time is measured in $\tau = (m\sigma^2/k_{\rm B}T)^{1/2}$. The unit of charge is taken to be the charge of a proton e and we express concentrations and ionic densities in molars (M).

We employ this model to examine the deformation of the ionic structure near interfaces in response to changes in system attributes such as ion concentrations, ion valencies, external electric fields, and interfacial dielectric contrasts. In the next two subsections we provide the details associated with the simulation and theoretical methods that are used to study the model system.

2.2.2. Molecular dynamics simulations

We simulate ions confined by the dielectric interfaces using MD methods. We account for the infinite extension of the interfaces in the simulation by considering periodic boundary conditions in the x and y directions. The whole system of ions and solvent confined within the two surfaces is taken to be in a rectangular simulation box of volume $V = H \times L \times L$, where L is a length that characterizes the size of the interface along the x and y directions. In all our simulations L is taken to be significantly larger as compared to the ion radius σ and the Debye length λ_{D} in order to accurately simulate the unboundedness of the system in the x and y directions. The long-range the electrostatic potential is treated within the approximation of the minimum image convention and using the charged sheets method. The charged sheets method has been described in Refs. [**83, 84**] and was employed in the simulation of the primitive model describing two immiscible electrolytes separated by a planar interface where it was found that the simulation results were in good agreement with experimental data [**85**]. As a check, we simulated the model systems by employing the 3D-Ewald sums with dipole corrections and the results were found to be nearly identical to those obtained using the charged sheets method. The length L is chosen to be large enough to minimize any errors that stem from the above approximate treatment of the long-ranged Coulomb interactions. The total number of dissociated electrolyte ions that enter our main simulation cell is $N = N_{\mathrm{p}} + N_{\mathrm{n}}$, where N_{p} and N_{n} are the total number of positive and negative ions respectively. To impose the desired temperature in the system, we employ Nosé-Hoover thermostat chains.

Table 2.1. Model parameters and simulation variables

$z_+ : z_-$	c_n (M)	$\lambda_{\mathrm{D}}(\sigma)$	$L\,(\sigma)$	N_{p}	N_{n}	N
$1:1$	0.1	2.69	96	212	212	424
	0.5	1.20	42.9	212	212	424
	0.9	0.89	32	212	212	424
$2:1$	0.1	2.20	96	106	212	318
	0.5	0.98	42.9	106	212	318
	0.9	0.73	32	106	212	318
$3:1$	0.1	1.90	96	71	213	284
	0.5	0.85	42.9	71	213	284
	0.9	0.63	32	71	213	284

In order to compare the three asymmetric electrolyte systems (1:1, 2:1, 3:1) we change the valency of positive ions keeping the average concentration of negative monovalent ions in the slit, $c_n = N_{\mathrm{n}}/V$, fixed. Keeping c_n fixed across the three electrolyte systems generates distributions of positive ions with a relatively smaller spread in their volume fractions (as compared to the case if $c_p = N_{\mathrm{p}}/V$ was held fixed). In addition, it generates all the three electrolyte systems with equal total positive charge (and equal total negative charge) which is distributed differently among the ions associated with 1:1, 2:1, 3:1 electrolytes. Thus, a fixed c_n enables us to attribute (for the most part) the differences in the ionic structure of the three systems to the differences in the valency of the positive ions and the associated changes in the electrostatic interactions. This allows us to accurately compare the contributions of electrostatic and hard-core interactions in determining the ionic distributions for the 1:1, 2:1, and 3:1 electrolytes. For the ease of presentation, we also use c_n to characterize the electrolytes, although it should be noted that for a z_+:1 electrolyte, the concentration is generally defined as N_{p}/V.

In Table. 2.1 we list the systems studied with MD simulations and the relevant parameters associated with their models. For the study of ions near unpolarizable interfaces, we use the standard MD simulation procedure. The ionic degrees of freedom are evolved using the velocity Verlet algorithm with a time step $\Delta = 0.0005\tau$. Table. 2.1 also provides the simulation details associated with this study for various concentrations c_n and stoichiometric ratios. Here $\lambda_{\rm D}$ is the Debye length calculated assuming the background dielectric is water; a large value of $\lambda_{\rm D}$ indicates a longer range for Coulomb interactions in the system. The length L is chosen much greater than $\lambda_{\rm D}$ in each case study.

In the case of polarizable interfaces, due to the presence of induced charges at the interface, the simulations incur a cost of meshing the interface with discrete finite elements to represent the induced charge density. This sets a limit on the simulation cell size L and for all the case studies with polarizable interfaces we choose $L = 40\sigma$. As is evident from the values of the Debye length for various cases (see Table. 2.1), this choice for L is still much larger than $\lambda_{\rm D}$. The number of positive and negative ions that enter the simulation cell are computed via the relations: $N_{\rm n} \sim 367 \times c_n$ and $N_{\rm p} \sim N_{\rm n}/z_+$ where c_n is in molars.

The need to accurately compute the induced charges on the interfaces at every step of the simulation in order to correctly update the ionic configuration makes the use of conventional MD methods to extract equilibrium densities very time consuming and inefficient. Therefore, we employ a recently-developed Car-Parrinello molecular dynamics method that allows the propagation of ionic degrees of freedom in tandem with an accurate update of the polarization charges at the interfaces [**42, 45**]. Our Car-Parrinello molecular dynamics simulation scheme is based on the

variational functional introduced in Ref. [**42**]:

$$
\begin{aligned}
I[\omega] = & \frac{1}{2} \iint \rho_{\mathbf{r}} G_{\mathbf{r},\mathbf{r}'} \left(\rho_{\mathbf{r}'} + \Omega_{\mathbf{r}'}[\omega] \right) \mathrm{d}\mathbf{r}' \mathrm{d}\mathbf{r} \\
& - \frac{1}{2} \iint \Omega_{\mathbf{r}}[\omega] G_{\mathbf{r},\mathbf{r}'} \left(\omega_{\mathbf{r}'} - \Omega_{\mathbf{r}'}[\omega] \right) \mathrm{d}\mathbf{r}' \mathrm{d}\mathbf{r},
\end{aligned} \tag{2.1}
$$

where ρ and ω are the free and induced charge densities respectively. The function $G(\mathbf{r}, \mathbf{r}') = |\mathbf{r} - \mathbf{r}'|^{-1}$ is the bare Green's function and Ω is given by

$$
\Omega_{\mathbf{r}}[\omega] = \nabla \cdot \left(\chi_{\mathbf{r}} \nabla \int G_{\mathbf{r},\mathbf{r}'} \left(\rho_{\mathbf{r}'} + \omega_{\mathbf{r}'} \right) \mathrm{d}\mathbf{r}' \right), \tag{2.2}
$$

with χ being the dielectric susceptibility. The particular form for the functional in the case of two sharp, planar dielectric interfaces is shown in the Appendix A. In this form, $I[\omega]$ becomes a functional of the induced charge density residing at the interfaces.

The minimization of $I[\omega]$ leads to the equation: $\omega = \Omega$; the solution of this equation generates the correct induced density on the interfaces. Furthermore, owing to the fact that $I[\omega]$ is a true energy functional, it offers the possibility to be minimized dynamically, that is, we are allowed to perform a simultaneous update of the free charge (ionic) configuration and the induced charge densities on interfaces I and II. To do this, we include $I[\omega]$ as the potential energy part of the Lagrangian L whose kinetic part includes the kinetic energy associated with the ions and a fictitious kinetic energy assigned to the surface induced charge density ω which is treated as a dynamical variable of mass μ. The value of μ is chosen so as to make the energy contribution of the fake degrees of freedom small. In practice, we choose these masses to be proportional to the areas of the finite elements employed to discretize the interface. Further details of the method can be found in Ref. [**42**].

We mesh each flat interface with $M = 484$ points generating a uniform grid of finite elements that are dressed with induced charges. The area per finite element is $L^2/M \sim 3.3\sigma^2$ which is

roughly the same size as the effective cross-sectional area of the ion $\sim \pi\sigma^2$. Using the equations of motion derived from L, we generate the dynamics for the whole system – ions and the fake degrees of freedom corresponding to the induced charge values, using the standard MD technique with a time step $\Delta = 0.001\tau$. The ions couple to a Nosé-Hoover thermostat reservoir at temperature $T = 298K$ while the induced charge (fake) degrees of freedom couple to a second Nosé-Hoover thermostat at a much lower temperature $T_f = 0.002T$. The value for fictitious mass μ depends on the particular system under study (concentration, stoichiometric ratios, etc.) and we find μ to fall in the range $\mu = 60 - 1000$ to optimize the stability of the simulation. Finally, due to the overall electroneutrality associated with the system, the net induced charge at each interface vanishes. We enforce this constraint in each step of our CPMD simulation via the shake-rattle routine [**86**].

As mentioned above, in CPMD simulations the amount of induced charge at a given interfacial grid point is treated as a dynamical variable and the overall system is described by an extended Lagrangian that includes the (fake) degrees of freedom associated with these induced charge variables in addition to the ionic degrees of freedom. As a result, a system with N ions confined by unpolarized interfaces effectively translates into a system with $2M$ additional degrees of freedom in the case of polarized interfaces (recall that M is the number of finite elements meshing each interface). As we do not employ any acceleration strategies such as Ewald sums or particle-mesh methods, the scaling associated with either of the MD methods employed is the typical $O(n^2)$ scaling characteristic of charge simulations. While the time complexity for the conventional MD simulation of ions confined by unpolarized interfaces is $O(N^2)$, the computational costs for CPMD simulations of ions confined by polarized surfaces scales roughly as $O((N + 2M)^2)$. Hence, on average, we find our CPMD simulations to be slower than conventional MD simulations roughly by a factor of $(N/(N + 2M))^2$. For instance, in the case of the CPMD simulations of monovalent electrolyte at $c_n = 0.5$ M with $N = 368$ ions and $M = 484$ grid points, the CPU time is 61.4

milliseconds per time step while for the MD simulation of the same system (with unpolarized interfaces), the CPU time is 9.4 milliseconds per time step. We note that these CPU times are for a simulation performed on a 16 core CPU node with OpenMP shared memory multiprocessing.

2.2.3. Liquid state theory

We base our theoretical method on the work of Kjellander and Marčelja's [**46, 47**], referred to as the Anisotropic Hyper-Netted Chain (AHNC). The method is thoroughly and completely described in these articles, and subsequent works by these authors, and explains in detail how the Ornstein-Zernike (OZ) equation is solved in an inhomogeneous system of primitive model electrolytes in a planar confinement. A visual interpretation of the mathematical procedure is presented in the supplemental information of Ref. [**5**], together with a discussion of some characteristic results. The theory does not only focus on the 1-particle density profiles, as many density functional theories and field-theoretical approaches, but also allows for the calculation of the anisotropic pair-correlation functions. The only approximation in the method is the choice for the particular closure equation for the OZ equation, in this case the Hyper-Netted Chain (HNC). The pair-correlation functions $h(\mathbf{r}, \mathbf{r}')$ and $c(\mathbf{r}, \mathbf{r}')$ (respectively the total correlation function h and direct correlation function c), are iteratively solved with the OZ equation

$$h(\mathbf{r}, \mathbf{r}') = c(\mathbf{r}, \mathbf{r}') + \int \mathrm{d}\mathbf{r}''\, c(\mathbf{r}, \mathbf{r}'')\rho(\mathbf{r}'')h(\mathbf{r}'', \mathbf{r}') \tag{2.3}$$

and the HNC closure

$$c(\mathbf{r}, \mathbf{r}') = h(\mathbf{r}, \mathbf{r}') - \ln(1 + h(\mathbf{r}, \mathbf{r}')) - \beta u(\mathbf{r}, \mathbf{r}'), \tag{2.4}$$

for a given pair potential u (in our case, the Coulomb potential plus a hard core repulsion), and for a given particle distribution $\rho(\mathbf{r})$. The potential is divided by the thermal energy $k_{\mathrm{B}}T = 1/\beta$. The

1-particle distribution ρ is calculated with the (exact) Boltzmann distribution

$$\rho(\mathbf{r}) = \rho_0 \exp(-\beta V(\mathbf{r}) - \mu_{\text{exc}}(\mathbf{r})), \tag{2.5}$$

with an external field V, and the excess chemical potential μ_{exc} (over the ideal contribution, i.e. due to pair-correlations), related to the logarithm of the activity coefficient. The excess chemical potential can be expressed in terms of the pair-correlation functions, for example by solving the exact Lovett-Mou-Buff-Wertheim equation [**4**], or if one uses the HNC approximation to solve the OZ equation, one can use a specific expression that follows from that approximation;

$$\mu_{\text{exc}}(\mathbf{r}) = \rho(\mathbf{r}) \int \mathrm{d}\mathbf{r}' \, \frac{1}{2} h\left(\mathbf{r}, \mathbf{r}'\right) \left(h\left(\mathbf{r}, \mathbf{r}'\right) - c\left(\mathbf{r}, \mathbf{r}'\right)\right) - c\left(\mathbf{r}, \mathbf{r}'\right), \tag{2.6}$$

as derived in Ref. [**87**], and applied in the AHNC in Refs. [**46, 47**].

The set of equations (2.3)-(2.6) is solved iteratively, until self-consistency is achieved within a small numerical error. Equations (2.3) and (2.4) yield the pair-correlation functions h and c for a given ρ, and equation (2.5) yields the density ρ for given pair-correlation functions h and c that are required to calculate the excess chemical potential, equation (2.6). For notational convenience and readability we have been omitting indices that denote particle type, but actually one would have to calculate the density ρ_i of each particle type i, and pair-correlation functions h_{ij} and c_{ij} between each pair of types i and j. In the AHNC, one discretizes the z-axis (the axis perpendicular to the planar boundaries), and labels the densities according to the distance z_k with an additional index k, and likewise, the pair correlation functions with two indices. A more complete notation of a correlation function could look like $h_{ij}(z_k, z_l, r)$, denoting the total pair correlation between a particle of type i at position z_k and one of type j at z_l, with cylindrical coordinate r (parallel to the boundaries) separating the pair. The procedure is exactly as described above, except that the

equations become (high-dimensional) matrix equations. Again, Refs. [**46, 47**] provide a complete description, with some application and interpretation in e.g. Refs. [**88, 5**].

The Coulombic part of the pair-potential should satisfy Poisson's equation. In the presence of different dielectric boundaries, we use the so-called method of images to achieve this. The result of this method is an infinite summation of Coulomb potentials $\propto \sum 1/r_i$ (that decay with the inverse of the distance r_i) between the particles within the slit, and between the particles and their infinite set of images [**5**]. The interaction between a particle and all its images can be interpreted as an external force acting on the particle that depends on the dielectric contrast, distance to the boundary, and separation between the boundaries [**5**]. The interaction between a particle and the images of another particle are included in the total pair-potential u [**46, 5**]. For the interaction between the ion and the interfaces we use a "soft" Lennard-Jones repulsive potential, the same potential as in the case of the simulations,

$$U(z) = 1 + \sum_{\mathrm{I}=1,2} 4\left(\left(\frac{\sigma}{|z - z_{\mathrm{I}}|}\right)^{12} - \left(\frac{\sigma}{|z - z_{\mathrm{I}}|}\right)^{6}\right), \tag{2.7}$$

for $|z - z_{\mathrm{I}}| < 2^{\frac{1}{6}}\sigma$ with z_{I} being the location of the interfaces. Otherwise, the particles are treated as perfectly hard spheres with a positive or negative charge. We expect this difference in the treatment of the short range repulsion to contribute towards small differences between the results of the CPMD and the AHNC. The electrostatic attractions could enable the ions to overcome a small region of the steep LJ-repulsion. The distance of closest approach is therefore smaller between oppositely charged ions with a LJ repulsion than between two ions with a perfectly hard core. This would result in a slightly stronger electrostatic coupling between LJ particles than between two hard spheres with a same diameter.

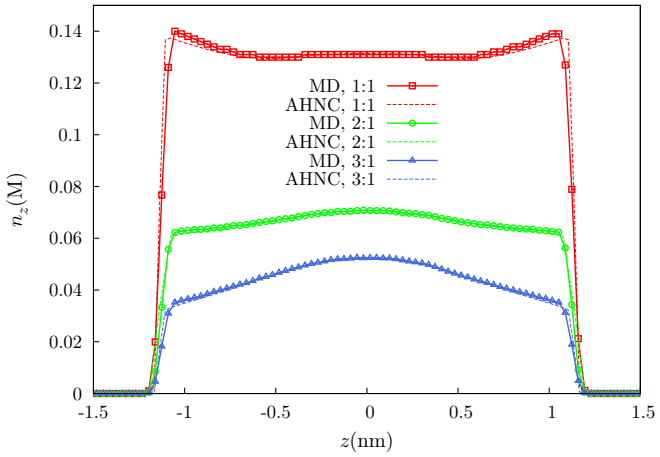

Figure 2.2. Density n_z of positive ions for a electrolyte at $c_n = 0.1$ M confined within two unpolarizable planar interfaces. Symbols correspond to MD results and dashed lines to AHNC calculations.

2.3. Results

2.3.1. Unpolarizable Interfaces

We begin by presenting our simulation and theoretical results for the case of ions confined within unpolarizable planar interfaces that separate media of the same dielectric (water) on either side. We first show how the equilibrium ionic structure in these systems deforms upon changing the stoichiometric ratio (ion valency) and/or electrolyte concentration. The ionic structure is represented by the number density n_z of ions in the z direction (in molars) and in some cases by their charge density ρ_z (in units of eM). In all our plots we show this density as a function of the z coordinate in nanometers.

2.3.1.1. Effect of ion valency and concentration. In Fig. 2.2, we plot the density profiles of positive ions for a $z_+ : 1$ electrolyte ($z_+ = 1, 2,$ and 3) with concentration $c_n = 0.1$ M. Note the reduction in the total number of positive ions as the valency of the positive ions is increased due to the constraint of electroneutrality. We find that the MD results and the AHNC lines are in good agreement aside from a small discrepancy at distances very close to either interfaces. We

attribute this mismatch to the differences in the modeling of ions in the two approaches. While in MD simulations we model ion-ion steric interactions via soft LJ forces, for the AHNC calculations these interactions are treated as hard-sphere interactions.

For the 1:1 electrolyte, we find the ion density (red squares) peaks near the interfaces as Fig. 2.2 shows. This implies that the positive ions corresponding to the 1:1 electrolyte tend to accumulate near the interfaces. This accumulation, as will be demonstrated later in this section, is the result of stronger steric interactions between the ions which dominate the weak interionic Coulomb interactions between the monovalent ions. Further, we observe the presence of a weak modulation in the density profile near the center of the confinement. As we will soon see, this modulation or layering in the ionic structure becomes more prominent as the average ion concentration is increased. The situation is different for the 2:1 and 3:1 electrolyte. We find that the multivalent ions associated with these electrolytes are depleted near the interface with the depletion more pronounced in case of the trivalent cations (blue triangles) as compared with the divalent ones (green circles). We attribute this depletion to stronger ionic correlations that are present in the case of multivalent ions. A graphic description of the microscopic mechanisms is shown Sec. 2.4.

We next show the results for the same systems as above but with higher electrolyte average concentrations. In Fig. 2.3 we plot the ion density profiles for the case where $c_n = 0.5$ M. Once again we observe a good agreement between MD (symbols) and AHNC (dashed lines) results with minor differences in the density values closer to the interface. We find that for the 1:1 electrolyte, the accumulation of ions (red squares) is enhanced near the interfaces as compared to the case of $c_n = 0.1$ M. We attribute this enhancement to the stronger steric effects present in the ionic system at $c_n = 0.5$ M. While in the $c_n = 0.1$ M case we observed a depletion in the ionic density of the 2:1 electrolyte close to the interface, for $c_n = 0.5$ M electrolyte the ion density of divalent ions (green circles) is enhanced near the interface which indicates the dominance of steric interactions over

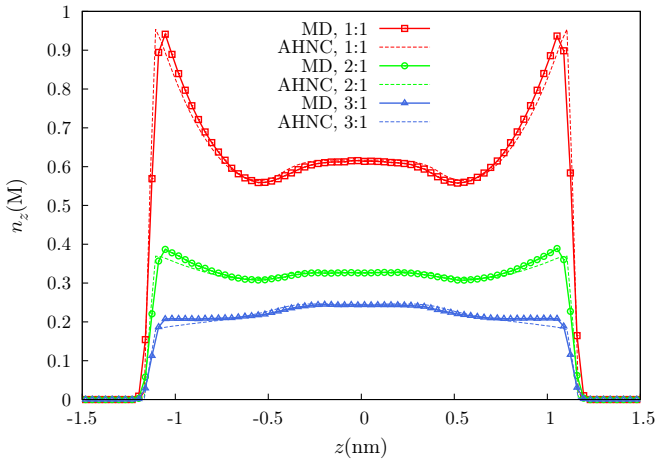

Figure 2.3. Density n_z of positive ions for a electrolyte at $c_n = 0.5$ M confined within two unpolarizable planar interfaces. Symbols correspond to MD results and dashed lines to AHNC calculations.

the Coulomb interactions. This competition between steric and electrostatic forces is seen to also produce the nearly flat (constant) density profile of trivalent ions (blue triangles) near the interface in the case of 3:1 salt in stark contrast to the situation in Fig. 2.2. In the $c_n = 0.1$ M case, the Coulomb interactions were sufficient to wash out the layered structure for 2:1 and 3:1 electrolytes. On the other hand, at $c_n = 0.5$ M we observe that the modulations in the ionic structure for these electrolytes are more pronounced.

Fig. 2.4 shows the ionic density profiles for the same system at concentration $c_n = 0.9$ M. We only show the densities generated via MD simulations as at this concentration we find it more difficult to converge the AHNC, and other closures may be more effective [**4, 89, 90**]. We find that the trend of higher accumulation near interfaces upon increasing c_n continues. For 1:1 electrolyte (red squares), the ions strongly prefer to assemble near the interfaces. The accumulation near the interfaces for the 2:1 electrolyte (green circles) is further enhanced as compared to the $c_n = 0.5$ M case. More importantly, we find that the strong steric effects at $c_n = 0.9$ M dominate the Coulomb interactions even for the 3:1 electrolyte. As Fig. 2.4 shows, we find enhanced accumulation of

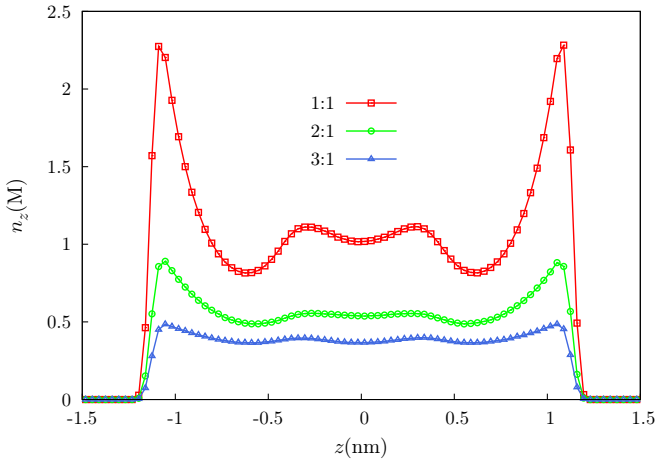

Figure 2.4. Density n_z of positive ions for a electrolyte at $c_n = 0.9$ M confined within two unpolarizable planar interfaces obtained from MD simulations.

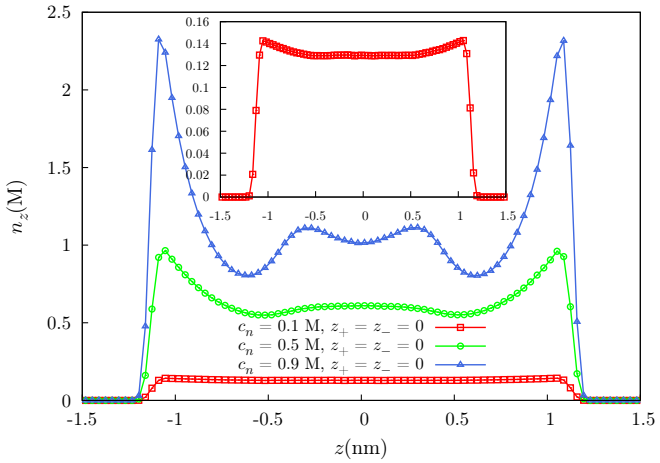

Figure 2.5. Density of particles obtained from MD simulations for a 0:0 electrolyte (no electrostatic forces) at concentration $c_n = c_p = 0.1, 0.5$, and 0.9 M confined within two unpolarizable planar interfaces.

trivalent cations (blue triangles) close to the interfaces in stark contrast to the $c_n = 0.1$ M case where electrostatics causes ion depletion near the interfaces. Furthermore, we find that at this concentration, for all three stoichiometric ratios, the modulations in the ionic structure become very prominent as compared to the aforementioned results at lower c_n.

It is useful to isolate and analyze the roles of steric and Coulomb interactions to understand why in the above studied systems the ions distribute as shown in Figs. 2.2–2.4. To achieve this, we turn off the charge on the ions in our simulations and obtain the densities for "ions" interacting via only the purely repulsive LJ forces. In other words, we replace both the positive and negative ions with electroneutral particles. We denote this system as the 0:0 electrolyte for the sake of brevity. In Fig. 2.5 we show the density profiles for this system at different concentrations $c_n = c_p = 0.1, 0.5$, and 0.9 M. The plots confirm our earlier assertion that the accumulation of ions near the interfaces is the result of strong steric interactions. Furthermore we find that the densities of 0:0 electrolyte at $c_n = 0.9$ M (blue triangles), $c_n = 0.5$ M (green circles), and $c_n = 0.1$ M (red squares, see inset) are nearly identical to the densities of 1:1 electrolyte at the same concentrations (red squares in Figs. 2.2–2.4), implying that the distribution of ions for the 1:1 case is largely determined by steric interactions. In addition, we find that the layering (modulations) of the ionic structure observed at the higher concentrations in Figs. 2.3 and 2.4 is indeed driven by steric interactions as similar modulations are seen in Fig. 2.5 at those concentrations as well.

By comparing the densities for the 2:1 and 3:1 multivalent salts with the plots in Fig. 2.5, we find that electrostatic forces dramatically alter the situation in these cases with their primary effect being to cause depletion of ions from the interfacial region as asserted before. For $c_n = 0.1$ M, electrostatics clearly dominates over the steric interactions leading to a fully depleted ionic density profile for the multivalent ions near the interfaces (see Fig. 2.2). For higher concentrations of $c_n = 0.5$ and 0.9 M, the two forces are more evenly matched and in some cases (see, for example, the density of trivalent ions at $c_n = 0.5$ M in Fig. 2.3) they appear to more or less cancel each other leading to a nearly uniform looking profile. In summary, we find that the steric interactions push the ions towards the interfaces and drive the layering (modulations) of the ionic structure while Coulomb forces deplete the ions from the interfacial regions. The competition between these two

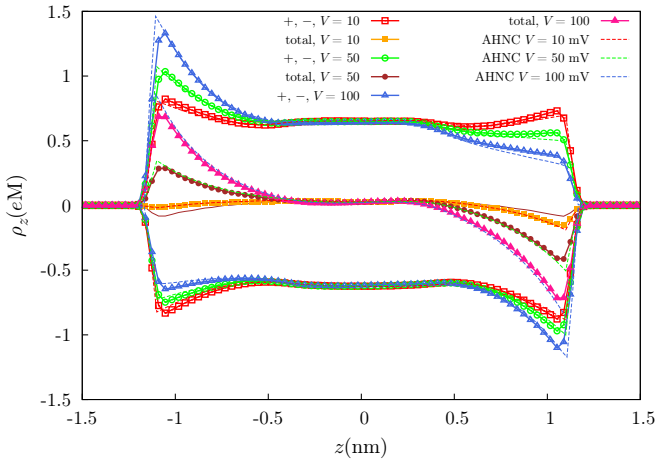

Figure 2.6. Charge density ρ_z of positive ions, negative ions, and all ions as a function of z for a 2:1 electrolyte at $c_n = 0.5$ M confined within two unpolarizable planar interfaces. The effect of increasing the external electric field (applied by creating a potential difference V between the two interfaces) is shown for $V = 10$, 50, 100 mV. The brown solid line is the total charge density at $V = 0$ mV (no external electric field). Symbols are MD simulation results and dashed lines are AHNC results.

forces, tuned to varying degrees by controlling parameters such as the concentration or ion valency, leads to a rich gallery of equilibrium ionic structures confined within the planar interfaces.

2.3.1.2. Effect of electric field. In electrochemical capacitors, the charging process creates a potential difference between the parallel plates which drives the ions present in the electrolyte towards the plate surfaces leading to the formation of electrical double layers[**91, 92, 93**]. The capacitive power of such devices comes from the energy stored in the electrical double layers. Thus, in order to understand the physics of electrical double layers formation and suggest improvements in the design and working of such devices, it is important to study the effects of an external electric field on the ionic structure formed in the electrolyte under confinement. Such a study also aids in understanding the effective forces between charged colloids in the presence of electrolyte ions [**12**].

We introduce a uniform electric field pointing from the right to the left interface. Its strength is measured by the potential difference V between the two interfaces. We analyze the ionic distributions of a 2:1 electrolyte with a concentration of $c_n = 0.5$ M at $V = 10, 50$, and 100 mV. In Fig. 2.6, we plot the charge densities (not the number densities) for positive ions, negative ions, and all the ions. The results for $V = 0$ case (depicted in Fig. 2.3) are also plotted for the sake of comparison. We first note that for all cases the center of the slit (near $z = 0$) is electroneutral, that is, it is populated with ions such that the net charge vanishes in the region. Next, we find that for $V = 10$ mV the densities are very similar to the case of neutral boundaries (no electric field) and we only observe a slight accumulation of positive ions on the left interface. However, in the total charge density we observe a slight asymmetry in the distribution about the $z = 0$ plane, finding a net negative charge near the right interface which is not balanced by a net positive charge on the left interface, but by a very wide peak of positive charge in the center of the slit. We attribute this to the inherent bias of the neutral system (for 2:1 salt at $c_n = 0.5$ M) towards a net negative total charge density near the interface as shown by the brown solid line near $\rho_z = 0$. We note that a mean field theory like Poisson-Boltzmann theory would predict a perfect anti-symmetric density profile for such a system.

As the potential difference between the two plates is increased to 50 mV, we see a more clear separation of ions in the system. The accumulation of positive ions in the neutral case near the right interface is now suppressed almost completely by the electric field working against it. The (absolute value of) charge density for the negative ($z_- = -1$) ions is still found to be maximum near the interfaces. The total charge density reflects the separation of charge with a near-antisymmetric distribution of ions. For $V = 100$ mV, the effects of electric field are the strongest of the studied cases which is to be expected. The positive ions prefer the left interface while the negative ions are

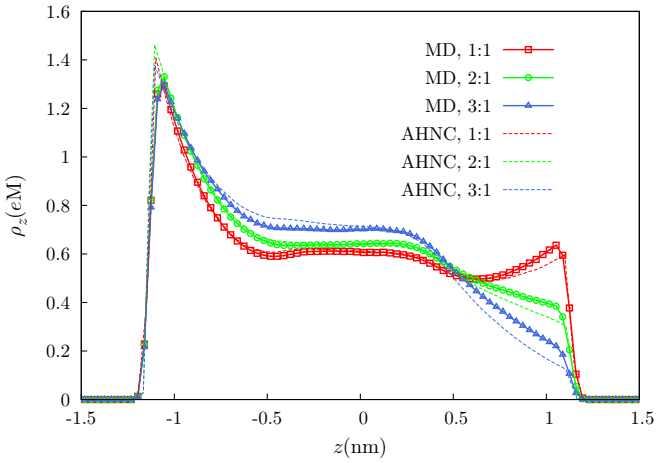

Figure 2.7. Charge density of positive ions for a $z_+ : 1$ electrolyte at $c_n = 0.5$ M and under the influence of an external uniform electric field corresponding to a 100 mV potential difference between the two interfaces and pointing from the right to the left interface. Interfaces are considered unpolarizable. Symbols are MD simulation results and dashed lines are AHNC calculations.

accumulated on the right. A clear separation of net charge is seen in the total density which has an antisymmetric form about the $z = 0$ center plane.

In Fig. 2.7 we plot the charge density of positive ions associated with 1:1, 2:1, and 3:1 electrolyte which is in the presence of an electric field corresponding to a potential difference of 100 mV between the left and right interfaces. The concentration is $c_n = 0.5$ M for all systems. We first find that the charge density near the $z = 0$ region increases as the valency of the positive ions is incremented. Note that for a fixed stoichiometric ratio, as Fig. 2.6 shows, the charge density near the central region remained unaffected by an increase of the electric field strength. Next we observe that the electric field is strong enough to push the positive ions towards the left interface. The peak value of the density near the left interface is seen to be independent of the valency of positive ions. Near the right interface, the charge density shows a much stronger dependence on z_+. We find that for the 1:1 electrolyte, the positive ions still accumulate near the right interface against the potential gradient. Recall that for the same system with neutral boundaries (that is without the electric field, see Fig. 2.3), ions preferred to assemble near the interfaces, a finding that

was attributed to the stronger steric forces at $c_n = 0.5$ M. It appears that this accumulation is not suppressed for the 1:1 case even with the potential bias of 100 mV. On the other hand, for the 2:1 and 3:1 electrolyte, the density plots show ion depletion near the right interface in contrast with the profiles that showed peak accumulation near the interfaces in the case of neutral boundaries. The depletion for trivalent cations is found to be stronger as compared with the divalent ions.

2.3.2. Polarizable Interfaces

We now study systems with polarizable planar interfaces, in other words, with interfaces that separate media of different dielectric permittivity on either side[**82, 76**]. We consider three different cases ($\epsilon_1|\epsilon_2|\epsilon_3$): case i) = $20|80|20$, case ii) = $40|80|10$, and case iii) = $20|80|160$ where ϵ_1, ϵ_2, and ϵ_3 are the dielectric constants of left, central, and right media respectively (see Fig. 2.1). These three examples are chosen to showcase the different effects that can arise due to the two polarizable interfaces. In the $20|80|20$ case, we expect the interfaces to cause depletion of the density near the interface with a symmetric final density profile owing to the equal dielectric contrasts at the two interfaces. The case of $40|80|10$ introduces the element of asymmetric depletion from the left and the right interface. The third scenario with $20|80|160$ is considered to introduce the possibility of one interface repelling the ions and the other attracting them. For each of these cases we investigate how the equilibrium ionic structure deforms upon changing the stoichiometric ratio and/or electrolyte concentration. The simulation results are obtained from CPMD method outlined in Sec. 2.2.2 where the averages for the ion densities are computed from runs with nearly 30 million steps (time step $\Delta = 0.001\tau$). While the polarization charge is treated in a discrete manner in the CPMD method, it is considered continuous in the AHNC method. The infinite sum of image charge contributions can be performed conveniently in k-space and results in a single exact expression. The AHNC therefore provides a reference for potential effects caused by the discretization of

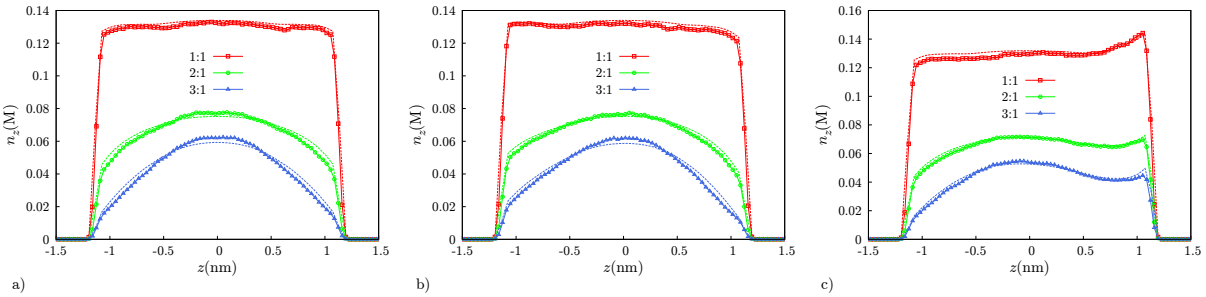

Figure 2.8. Density n_z of positive ions for a $c_n = 0.1$ M electrolyte confined within two polarizable planar interfaces with dielectric profile (a) $20|80|20$, (b) $40|80|10$, and (c) $20|80|160$ (see text for the meaning of the notation). Symbols correspond to CPMD results and dashed lines to AHNC calculations.

the polarization charge in the CPMD. Once again, we represent the ionic structure by the number density of ions in the z direction and show this density in molars as a function of the z coordinate in nanometers.

2.3.2.1. Low salt concentration: $c_n = 0.1$ M. In Fig. 2.8 we plot the density profiles of positive ions for a $z_+ : 1$ electrolyte ($z_+ = 1, 2$, and 3) with a concentration of $c_n = 0.1$ M and dielectric configurations of $20|80|20$, $40|80|10$, and $20|80|160$ respectively. We find that the CPMD predictions and AHNC results are in very good agreement. Recall that for this same system with unpolarizable interfaces, we found the monovalent positive ions to assemble near the interfaces while the divalent and trivalent ions stayed away from the interfaces (see Fig. 2.2). From Fig. 2.8(a) we see that the density of monovalent ions (red squares) is depleted near the interfaces for the $20|80|20$ system. Further, we find that the depletion of multivalent ions (green circles for divalent ions and blue triangles for trivalent ions) is stronger as compared with the unpolarizable interface case. This enhanced depletion is due to the fact that the ion in water (central medium) induces a charge on either interface of the same sign because of the lower dielectric constants of media adjacent to the central medium. This same charge repulsion reinforces the already present depletion due to strong electrostatic ion-ion correlations which is sufficient to overcome the accumulation near the

interfaces favored by the steric forces for the case of monovalent ions. Additionally, we find that the profiles for the $20|80|20$ are symmetric about the $z = 0$ plane as in Fig. 2.2.

We next examine the density profiles for the $40|80|10$ system which are shown in the plot of Fig. 2.8(b). We first notice the asymmetric nature of the densities owing to the different values for the dielectric contrasts at the left ($40|80$) and the right ($80|10$) interface. As the dielectric media adjacent to the central region still have a lower dielectric constant, we find the ionic density profiles to be depleted relative to the unpolarizable interface case. We find that due to a stronger contrast at the $80|10$ (right) interface, the depletion is stronger near it as compared with the $40|80$ (left) interface. The density for monovalent ions (red squares) near the left interface is nearly uniform implying that the depletion of ions near the interface caused by the repulsion due to the induced charges at this interface is not so strong to completely overcome the accumulation caused by the steric interactions. Next, in Fig. 2.8(c) we show the profiles for $20|80|160$ case. Here, while the left polarized interface causes ions to repel away from the interface, the right interface attracts them owing to fact that the media right to the central medium has a higher dielectric constant and thus leads to the induction of a charge of opposite sign on the interface due to the ion in water. Hence, we find that the density profiles show an accumulation near the right interface and depletion near the left one, the depletion becoming stronger with rising z_+. Unlike Fig. 2.8(a) and Fig. 2.8(b), we observe an additional non-monotonicity in the density profile for the multivalent ions where the density starts to first drop as one moves away from the central ($z = 0$) region and then rises again close to the right interface.

2.3.2.2. High salt concentration: $c_n = 0.5$ M and $c_n = 0.9$ M. We next show the results for the same systems as above but at higher electrolyte concentrations. Here, the effects due to the polarized interfaces are similar to the above discussed case of $c_n = 0.1$ M and hence we will be

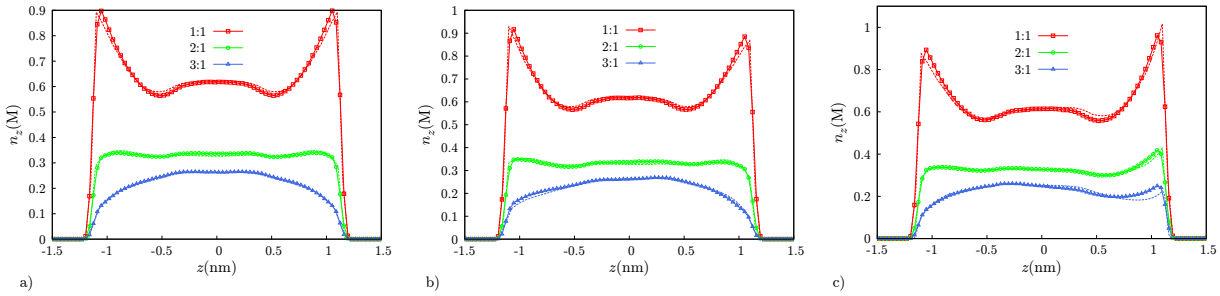

Figure 2.9. Density n_z of positive ions for a $c_n = 0.5$ M electrolyte confined within two polarizable planar interfaces with dielectric profile (a) $20|80|20$, (b) $40|80|10$, and (c) $20|80|160$ (see text for the meaning of the notation). Symbols correspond to CPMD results and dashed lines to AHNC calculations.

brief in their description, although, in contrast to the previous case, the effects may be secondary to the effects of the ionic correlations.

In Fig. 2.9, we plot the ion density profiles for the case where $c_n = 0.5$ M. Once again the agreement between CPMD (symbols) and AHNC (dashed lines) results is good with minor differences in the profiles closer to the interfaces. Recall that for this system with unpolarizable boundaries we observed that monovalent and divalent cations preferred to be near the interfaces while the trivalent ions stayed away from the interfaces, and we also saw enhanced modulations in the ionic structure (see Fig. 2.3). We find a similar overall trend for the density of monovalent ions (red squares) for all the three systems with polarizable interfaces studied, with some subtle differences near the interfaces which arise due to the induced charge repulsion or attraction as explained above. On the other hand, for the divalent ions (green circles) we find that the dielectric effects are strong enough to alter the density profiles obtained for unpolarizable boundaries. In the case of $20|80|20$, the density is depleted very close to the interface (see Fig. 2.9(a)) and appears to exhibit more modulations relative to the unpolarized systems. For the $40|80|10$ system, as Fig. 2.9(b) shows, the density is depleted near the right interface (strong induced charge effect) and rises near the left interface (weak induced charge effect unable to overcome steric effects) in accordance with

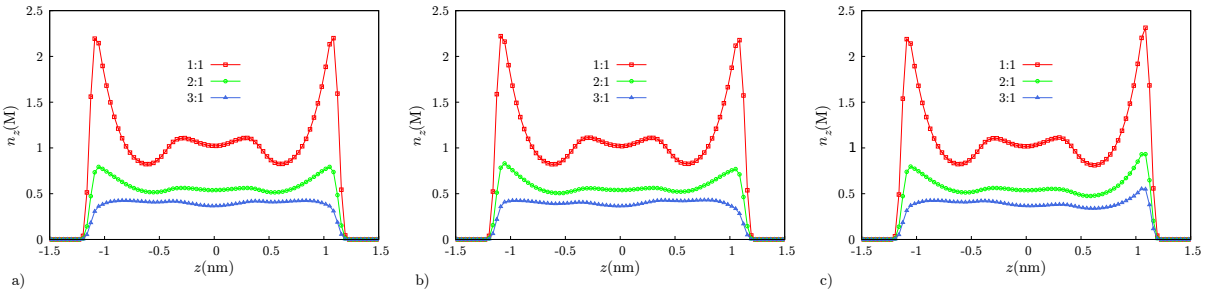

Figure 2.10. Density n_z of positive ions for a $c_n = 0.9$ M electrolyte confined within two polarizable planar interfaces with dielectric profile (a) $20|80|20$, (b) $40|80|10$, and (c) $20|80|160$ (see text for the meaning of the notation). Symbols correspond to CPMD results.

the induced charge effects suggested by the dielectric contrasts at the two interfaces. Finally, for the $20|80|160$ case we find that the divalent ion density peaks near the right interface and is suppressed close to the left interface in alignment with our expectations from the dielectric response of the two interfaces (see Fig. 2.9(c)). In the case of 3:1 salt (blue triangles), we find that the ion-ion electrostatic forces and the Coulomb (dielectric) interactions between the ions and the interfaces dominate the ionic structure near the interfaces in all the dielectric profiles studied.

Fig. 2.10 shows the ionic density profiles for the same system as analyzed above but now with a concentration $c_n = 0.9$ M. We only show the densities generated via MD simulations. We find that for the monovalent and divalent ions the effects of polarizable interfaces on the density profiles are weak and the steric interactions dominate the physics at this concentration as they did in the case of the unpolarized interfaces at $c_n = 0.9$ M illustrated by Fig. 2.4. Ion accumulation near interfaces for 1:1 and 2:1 salts is seen across the board with the polarized interface only slightly diminishing or enhancing the density near the interface based on the sign of the induced charge. Further, the modulations in the ionic structure for these systems continue to be present in the case of polarized interfaces as well. We find that the dielectric contrasts mainly influence the structure of trivalent cations (blue triangles) close to the interfaces. In stark contrast to the $c_n = 0.9$ M case with no dielectric contrasts where steric interactions cause ion accumulation near the interfaces for 3:1

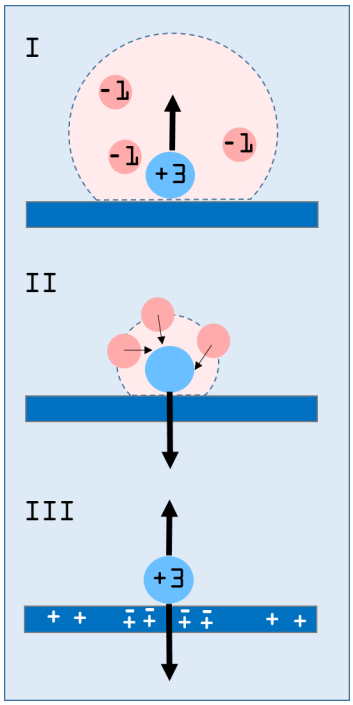

Figure 2.11. Mean forces acting on an ion near a dielectric boundary. Deformation of the double layer tends to pull ions away from the boundary (effect I), but steric interactions tend to push ions against the boundary (effect II). Surface charge and polarization charge can attract or repel ions, depending on the relative sign of the charges (effect III). We find that effects I and II, which are absent in mean field theories, can compete with and overcome surface charge effects (effect III). The effects are shown for a 3:1 electrolyte, but apply to both symmetric and asymmetric electrolytes.

electrolyte (see Fig. 2.4), we find that the repulsion due to induced charges in conjunction with the existing ion-ion electrostatic forces cause the suppression of the density close to the interfaces for $20|80|20$ and $40|80|10$ systems and near the $20|80$ interface of the $20|80|160$ system. In addition, the overall density of trivalent cations appears to be nearly uniform in between the interfaces aside from the strong rise seen near the $80|160$ interface for the $20|80|160$ system.

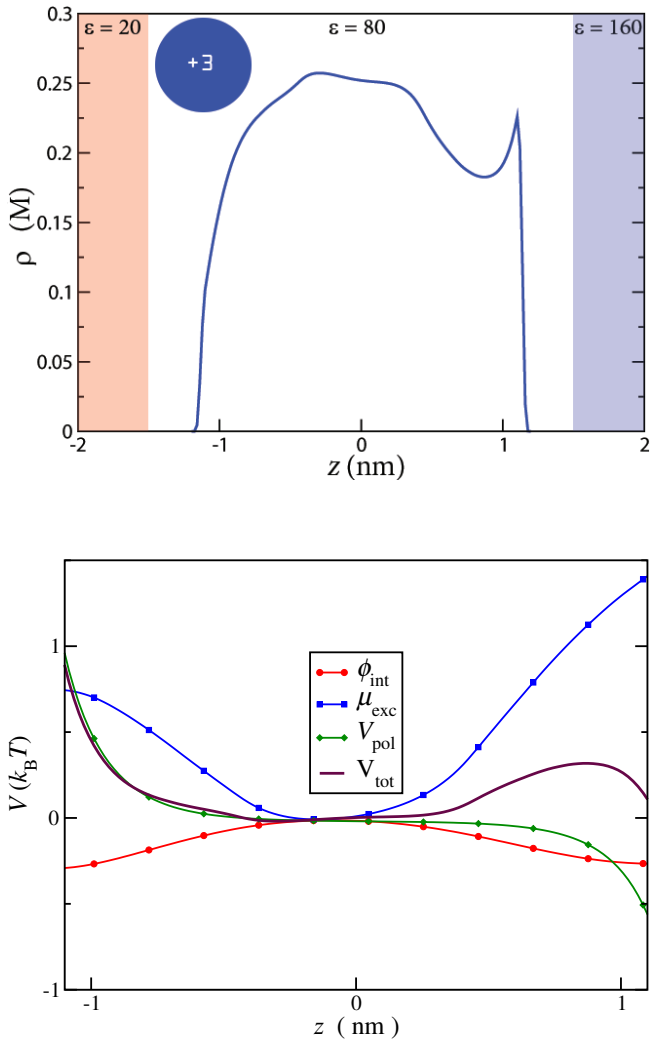

Figure 2.12. Concentration profile of trivalent ions in a 3:1 electrolyte with a mean concentration of $c_n = 0.5$ M, in a slit with dielectric profile $20|80|160$ (a). The corresponding potentials acting on the trivalent ions are shown separately, calculated by the AHNC (b). The electric potential generated by local charge segregation is shown as the red line ϕ_{int}. Charge segregation is driven by the excess chemical potential μ_{exc} resulting from electrostatic and steric correlations (effects I and II in figure 2.11), and V_{pol}, the polarization charge at the boundaries (effect III in figure 2.11). The total potential is the sum of the contributions, $V_{\text{tot}} = 3\phi_{\text{int}} + \mu_{\text{exc}} + V_{\text{pol}}$. The excess chemical potential from ionic correlations can overcome that of the polarization charge, $|\mu_{\text{exc}}| > |V_{\text{pol}}|$, typically at higher concentrations.

2.4. Discussion

2.4.1. Structural features from ion-ion correlations

Figures 2.2 - 2.5 show several structural features in the ion density profiles that become more pronounced with ion concentration and valency. Ions are found to deplete from the boundaries, adsorb to the boundaries at higher concentrations, and show density oscillations at high concentrations. The forces that govern these structural features are not directly exerted by the boundaries, which are charge neutral and dielectrically matched in Figs. 2.2 - 2.5, but arise from the thermal motion of the ions and the geometric constraints that the boundaries impose.

The explanation for the adsorption behavior can be understood by investigating the average local environment of an ion. In addition to yielding density profiles that are in close agreement with the MD and CPMD simulations, the AHNC also calculates the anisotropic pair correlation functions between the ions. These functions yield direct information about the mean forces that the ions experience between the boundaries, resulting from a combination of thermal motion and direct interactions. The main assumption of mean field theories is to put these forces to zero by assuming the pair correlation functions to be constant. Such theories will therefore never distinguish the structural features of Figs. 2.2 - 2.5, and many widely-applied Poisson-Boltzmann theories, for example, would predict uniform ion density profiles. Still it is possible to refer to the seminal work of Debye and Hückel to explain the features in a qualitative fashion. However, for quantitative predictions and a more complete picture of the phenomenology it is necessary to invoke the AHNC.

For a qualitative explanation it is sufficient to know that electrolytes in a charged fluid are on average surrounded by compensating opposite charge. The “cloud” of screening charges (the “double layer”) is spherical in bulk by symmetry arguments, but needs to deform close to a hard boundary because the cloud cannot penetrate the boundary. In what follows, we consider the 3:1

electrolyte at $c_n = 0.5$ M as an example system to discuss our explanation. Similar arguments can be invoked for all the other systems studied. Figure 2.11 shows the average charge distribution around an ion near the boundary (effect I). The asymmetric screening cloud exerts a force on the central ion, away from the boundary, resulting in an average depletion from the boundary. This (microscopic) depletion mechanism, which we attribute to electrostatic interactions, would apply to confined ionic fluids in general, except that its effect may be additive to those of other mechanisms. A second mechanism, driven by steric interactions, is related to the volume fraction of ions or, in other words, to their entropy. Adsorption of ions increases the free volume of the remaining ions, which can be entropically favorable at high densities. An alternative way to rationalize the adsorption is to realize that ions near the boundary experience more collisions with other ions towards the boundary than away from it, resulting in a mean force towards the boundary (effect II of Fig. 2.11). Both effects are visible in Fig. 2.12. The potential $\phi_{\rm int}$ is the electrostatic potential that is caused by the mean segregation of charge, whereas $V_{\rm pol}$ is the electrostatic potential generated by the polarization charge. The excess chemical potential $\mu_{\rm exc}$ is the mean potential that an ion experiences from the average interactions with the other ions, subtracted by the mean potential $\phi_{\rm int}$. By defining $\mu_{\rm exc}$ in this way, it measures a mean potential purely caused by the local ordering of charge. The total potential that a trivalent ion experiences is the sum of these contributions: $V_{\rm tot}(z) = V_{\rm pol}(z) + 3\phi_{\rm int}(z) + \mu_{\rm exc}(z)$. For the parameters of a 3:1 electrolyte, the variation in the excess chemical potential $\mu_{\rm exc}$ is larger than the variation in the mean potential $\phi_{\rm int}$. This demonstrates the importance of calculating the anisotropic correlation functions that are required to get an accurate value for $\mu_{\rm exc}$, as opposed to a majority of mean field methods that ignore the existence of $\mu_{\rm exc}$ and solve for $\phi_{\rm int}$ in a self-consistent manner. For the trivalent ions, the effect of $\mu_{\rm exc}$ is also opposite to that of $\phi_{\rm int}$, and contributes to the spontaneous formation of a double layer near the boundaries. Although the double layer near the boundary is unfavorable from a global

perspective of ion entropy and electrostatic energy ($\phi_{\rm int}$), it is compensated by a more favorable local configuration of charge ($\mu_{\rm exc}$), because the trivalent ions are more favorably screened in the center of the slit. The electrostatics-driven depletion is found to increase with density and valency, with a range corresponding to the electrostatic correlation length (which decreases with density). The hard-core-driven adsorption is found to increase sharply at high densities, with a range corresponding to the ion size.

We ascribe the oscillations in the ionic density to a balance between two mechanisms: a maximization of free volume (entropy) and minimization of total electrostatic energy. In a recent work, Nygård *et al.* investigated density oscillations of a hard sphere fluid in a narrow slit [**4**]. In our case, the Coulomb interactions enrich the phenomenology, but at high densities we see similar effects, especially for monovalent ions.

Figures 2.8 - 2.10 show the additional influence of surface polarization. This effect has been analyzed in many contexts, and is often approached with the "method of images". Figures 2.8 - 2.10 show however that it is a secondary effect at higher ion concentrations[**94**] which only slightly modifies the structure imposed by ionic correlations (effects I and II in figure 2.11). At the same time, the spatial variation of the dielectric properties of the environment, particularly in the case of electrolytes with low concentrations and multivalent ions, was found to have profound effects on the ionic structure. Hence coarse-grained models and associated theoretical/computational procedures to study charged soft matter systems should include dielectric heterogeneities to accurately capture the physical properties of these materials.

2.4.2. Features in the total charge density

We point out another important feature of the ionic structure that, for the sake of brevity, we did not discuss in Sec. 2.3. It is tempting to conclude, especially in the case of neutral, unpolarizable

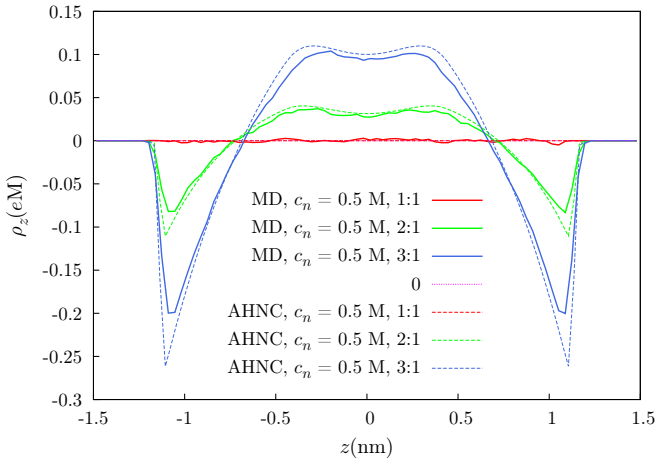

Figure 2.13. Charge density corresponding to all the ions in the system for a $z_+ : 1$ electrolyte at concentration $c_n = 0.5$ M within two unpolarizable planar interfaces with dielectric profile $80|80|80$ (see text for the meaning of the notation). Solid lines are MD results and dashed lines correspond to AHNC calculations.

boundaries, that while the rich variations in the density profile for the positive ions of a $z_+ : 1$ electrolyte can be expected as a result of the aforesaid competition between electrostatic and steric interactions, the total charge density should be featureless owing to the cancellations coming from the considerations of both positive and negative ions. Indeed, Poisson-Boltzmann theory and many of its modifications [**95**] would predict a uniform distribution coincident with the $\rho_z = 0$ line for the charge density of the total number of ions. This was found to be the case in our AHNC and MD calculations for the 1:1 electrolyte system at all concentrations where the result is to be expected from symmetry considerations as well. As Fig. 2.13 shows, our AHNC calculations found that the total charge density ρ^t was identically zero everywhere and our MD result for ρ^t was seen to fluctuate around zero, the small deviations from zero arising from the statistical noise present in the simulations. However, deviations from mean field theory predictions were observed for total charge densities of systems with asymmetric electrolytes containing multivalent ions [**96, 97**]. We found features in ρ^t similar to those seen in the density of positive ions n_z in the figures shown

in Sec. 2.3.1.1 with the modulations in the density and the depletion/accumulation near the interfaces becoming significant as c_n increased. For example, in Fig. 2.13, we show the total charge density as a function of z for 1:1, 2:1, and 3:1 electrolytes at $c_n = 0.5$ M. Clearly, for the 2:1 and 3:1 systems, the ionic structure is not washed out because of the cancellations predicted by a mean field approach. Since the steric interactions in all these systems can be assumed to be the same, we conclude that the features in ρ^t arise as a result of the electrostatic correlations between ions which are neglected in a typical mean field theory. We do, however, expect that in the case of systems under the influence of external electric field of high strength, these variations in the density will be overpowered by the external bias and in such situations Poisson-Boltzmann theory results will yield more accurate predictions of the total charge density. Some examples of modified Poisson-Boltzmann theories, such as by dos Santos and Levin [**98, 43**], actually estimate the excess chemical potentials of the ions and incorporate those self-consistently in the Boltzmann distribution. These theories actually distinguish features caused by electrostatic correlations between the ions, and would capture the features in Fig. 2.13.

2.5. Conclusion

We calculate the non-monotonic density profiles of primitive model electrolytes in a dielectric confinement, with standard molecular dynamics and Car-Parrinello molecular dynamics simulations and a theoretical method known as the AHNC. Both methods are free of adjustable parameters and show excellent agreement. We observe several features in the density profiles, such as adsorption at the ionic length scale, depletion over the electrostatic correlation length, and density oscillations over the entire profile, and connect a rich phenomenology of effects to three simple microscopic mechanisms. Two of these mechanisms result purely from ionic correlations and symmetry breaking at the interface, and are missed entirely in mean field theories (by assumption). We

show here that polarization charge at the confining boundaries can modify the ionic profiles significantly, although it appears to generate a smaller force on the ions compared to the thermal forces culminating from steric and electrostatic interactions between the ions, i.e. the ionic correlations, roughly above 0.1 M concentrations. These mechanisms can induce charge segregation in asymmetric electrolytes that can increase, decrease, or reverse the effective charge of the boundary, and can induce non-monotonic forces between the boundaries[**13, 14**]. Although we postpone the discussion of these forces to future work [**99**], we reduced the origin to three mechanisms that span the range of possible interfacial phenomena in the primitive model of electrolytes. The results of the CPMD and AHNC shed light on the origin of ion-specific and dielectric effects in confinement, which can be meaningful in the interpretation of effective interactions between nanoparticles, biomolecules, and membranes, and for the evaluation of interfacial activity in separation and process technologies.

Our MD simulations and AHNC did not use any adjustable parameters, and should in principle yield numerically exact results for the primitive model, which is corroborated by the excellent agreement. The AHNC has the advantage of being numerically efficient, and converges generally within a few minutes on a single CPU. The algorithm, however, relies on many coupled numerical procedures, and the numerical parameters need to be chosen carefully to guarantee convergence, such that algorithm development is relatively involved (compared to e.g. PB theory). The AHNC also yields the thermodynamic potentials on the fly, which are expensive to calculate with the CPMD, as well as the anisotropic correlation functions and potentials of mean force, which allow us to identify and separate the underlying mechanisms that are responsible for the observed features in the density profiles (as in Figs. 2.11 and 2.12). The AHNC does however rest on an approximation for the closure of the Ornstein-Zernike equation, the so-called Hyper-Netted Chain or HNC, which could lead to deviations that are likely to be nihil for the chosen parameters. In the case of

polarized interface systems, the accuracy on the density profiles is determined by the interfacial grid spacing, both for the simulations and the AHNC (lower grid spacing implies finer resolution of the interface and leads to higher accuracy). In some cases, the assumption of planar shapes for the dielectric interfaces may break down and curvature effects may become strong. We note that our CPMD simulations are well suited for systems with curved interfaces as demonstrated in Ref. [**42**] where ion distributions near a spherical interface were computed. More complex shapes will benefit from clever ways of meshing the interface but the overall CPMD procedure is similar to the method presented here for the two planar interfaces. Furthermore, the costs associated with the CPMD simulations of ions near interfaces of complex geometry would be similar to the costs incurred in the simulations for planar interfaces because the CPU time primarily depends on the interface area rather than its shape. We realize that, although our methods are numerically accurate for the primitive model, the model system itself assumes a homogeneous structureless medium without impurities, and will not describe certain effects common in aqueous electrolytes [**100**]. The model system also assumes infinitely sharp dielectric boundaries, which may oversimplify the molecular width of e.g. liquid-liquid or liquid-gas interfaces [**63**]. However, the CPMD and AHNC could offer pathways to quantify those additional effects, and derive effective potentials given that the ion thermodynamics within the model system is correctly treated. In the end, we note that our simulations and theory are versatile enough to treat the case of other multivalent salts (2:2, 3:3), asymmetric ion sizes, mixture of electrolytes, and the dynamical evolution of the soft ionic structure.

CHAPTER 3

Ionic structure and electric field at the oil-water interface with size-asymmetric monovalent ions

3.1. Introduction

The ionic cloud at the interface between two immiscible electrolyte solutions (ITIES) is the so-called electrical double layer. This accumulation of diffuse charge can arise from the difference in the ionic solvation energy in each liquid medium or from the application of an electric field. In living organisms, different dielectric properties and ion concentrations can be maintained inside cells in contrast to the external medium via molecular pumps, which can induce transmembrane ion diffusion metabolizing energy. The molecular details of the ionic distribution near the interfaces determine the properties of the electric field generated by these charged particles. The relevance of the electric field (or the electrostatic interactions) to the adsorption and self-assembly properties of charged colloidal micro/nanoparticles at liquid interfaces has been demonstrated in recent experimental studies as a novel avenue to design more complex molecular structures[**101, 102**]. In fact, colloidal nanoparticles can be used to stabilize emulsions producing so-called microcapsules[**103**], which could be used to deliver encapsulated materials in biomedical applications. Label-free detection based on liquidliquid interfaces has also been proposed[**104**].

In order to gain a better understanding of the molecular structure of the ITIES, simulation studies have been conducted considering explicitly solvent particles. Nevertheless, the vast number of solvent particles required to study the ITIES under experimental ion concentrations (typically in the range of millimoles) makes this kind of calculation non-attainable, despite the current advances

in computing capability. On the other hand, the classical Poisson-Boltzmann theory of point ions has been used since last century to describe the electrical double layer at the ITIES[**91**]. One important limitation of this approach is that it does not take into account the ion correlations and excluded volume effects[**105, 106**]. The former is related to the physical fact that an ion likes to be surrounded by ions of opposite charge, whereas the latter means that two ions cannot occupy exactly the same position in space. In the classical PoissonBoltzmann theory of point ions, the two double layers that meet at the ITIES do not interact, and the corresponding polarization effects due to dielectric heterogeneities are completely neglected[**91**]. These effects are relevant if the dielectric properties of the two immiscible liquids in contact significantly differ. In the most simple case, polarization effects can produce the attraction (repulsion) of a single charge toward a macroscopic sharp interface limiting another medium with a higher (lower) dielectric constant[**107**].

Given the evident limitations of the classical Poisson Boltzmann picture of point ions, several theoretical approaches have been proposed to successfully describe the experimental results of the ITIES[**108, 109, 110**]. Nevertheless, these improved schemes are also restricted by ad-hoc adjustable parameters, which limits their predictive use. Thus, we perform here coarse-grained Monte Carlo simulations of an experimental oil-water interface in the presence of an electric field - including realistic ionic size-asymmetry, ion correlations, excluded volume of ions, and image charges to study its thermodynamic and microscopic properties without needing any adjustable parameter. In particular, these Monte Carlo simulations are used to study the surface tension of oil-water interfaces in the presence of size asymmetric monovalent salts with the goal of determining the effects of ion correlations, polarization, and ionic excluded volume in the diffuse electrical double layer. At the molecular level, we observe that the electrolyte concentration and the ionic size-asymmetry can be used to tune the electric field near the liquid-liquid interface. Thus, the electric field can be significantly increased or even reversed in this region depending on the polarity of

the difference in the mean electrostatic potential in the bulk phases of oil and water. We reproduce surface tension experimental data of LiCl and TBATPB (tetrabutylammonium-tetraphenylborate) near an oil-water interface in the presence of an electric field in the Results and discussion section. We use only experimental values of all relevant physical parameters of the system, such as the ionic size and the dielectric constant in the bulk liquid media, without any additional adjustable parameter. In the Conclusions section, we argue that the enhancement and the reversal of the electric field at high electrolyte concentrations is analogous to the surface charge amplification[**111, 112**] and the charge inversion observed experimentally in macroscopic colloidal systems[**113, 114**]. If a difference due to ion partitioning exists in the mean electrostatic potential in the bulk phases of oil and water, these phenomena could also be present in synthetic and biomolecular interfaces, even in the absence of an applied electric field.

3.2. Model and methods

3.2.1. Model

We describe the ion distribution at the interface between two immiscible electrolyte solutions using the primitive model. In this scheme, the solvent is a continuum medium characterized by a dielectric constant, ϵ. Nitrobenzene and water, with dielectric constants $\epsilon_O = 34.8$ and $\epsilon_O = 78.4$, respectively, are the two immiscible adjacent solvents placed in contact. Ions are modeled as hard spheres with point-charges embedded in their centers. TBA^+, tetrabutylammonium, and TPB^-, tetraphenylborate, ions are submerged in nitrobenzene, while Li^+ and Cl^- ions are submerged in water. The diameter of the ionic species are: $d_{TBA^+} = 7.7$Å, $d_{TPB^-} = 8.2$Å, $d_{Li^+} = 4.2$Å, $d_{Cl^-} = 6.4$Å, for TBA^+, TPB^-, Li^+ and Cl^- respectively[**115**]. The sharp dielectric discontinuity is modeled as an impenetrable neutral hard wall (Fig. 3.1). We neglect the ion transfer between the two solvents because the standard Gibbs energies of transfer of LiCl from water to oil, and of

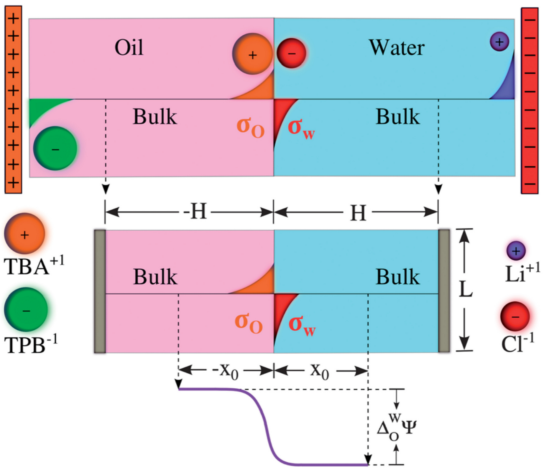

Figure 3.1. Schematic representation of the experimental system (top), the Monte Carlo setup used in the simulations (middle), and the difference in the mean electrostatic potential in the bulk phases of both immiscible electrolytes (bottom).

TBATPB from oil to water are significant[**116**]. Polarization effects are included via the image charge method, as described below.

In typical experiments, an electric field is applied to the liquidliquid interface. As a result, charge accumulation is observed on both sides of the dielectric discontinuity (see Fig. 3.1). Let us denote $E(\vec{x})$ as the electric field, and $\Psi^W_\infty - \Psi^O_\infty = \Delta^W_O \Psi$ as the difference in the mean electrostatic potential in the bulk phases of both immiscible electrolytes. The boundary conditions for this system are $\Psi^O_\infty = 0$ and $E^O_\infty = 0$ in oil, with $\Psi^W_\infty = \Delta^W_O \Psi$ and $E^W_\infty = 0$ in water. Physically, these boundary conditions establish that the difference in the mean electrostatic potential in the bulk phases of both electrolytes is constant, and the electric field vanishes in the bulk electrolytes. The original applied electric field in the experiments is replaced in our simulations by an imposed excess of surface charge density in nitrobenzene, σ_O, and water, σ_W (Fig. 3.1). As the experimental system is electroneutral, the global excess charge imposed is equal to zero, $\sigma_W + \sigma_O = 0$. From the ion distribution around the liquid interface, it is possible to calculate the electric field near the

dielectric discontinuity and the difference in the mean electrostatic potential in the bulk phases of the electrolytes, $\Delta_O^W\Psi$ for a given excess surface charge density in water, σ_W , using the Gauss law as described below. The advantage of this approach is that the specific details of the applied electric field producing the interfacial ionic accumulation are no longer required because, macroscopically, the electrodes are completely screened in the bulk phases of both immiscible electrolytes. Thus, the excess surface tension at the oil-water interface can be calculated as a function of $\Delta_O^W\Psi$ using the Lippmann equation[**117**]:

$$\sigma_W = -\frac{\partial\gamma}{\partial\Delta_O^W\Psi}. \tag{3.1}$$

3.2.2. Electrostatic interactions with a dielectric discontinuity-Image charge method

In the primitive model, interactions among charged particles can be grouped into two types: one-body and two-body. These interactions can also be separated into a hard sphere contribution and an electrostatic component. The two-body interaction for hard spheres is given by $S_{ij}(r_{ij}) = 0$ if particles i ($\vec{r}_i = (x_i, y_i, z_i)$) and j ($\vec{r}_j = (x_j, y_j, z_j)$) do not overlap, and $S_{ij}(r_{ij}) = \infty$ otherwise. The distance between the particles is defined as $r_{ij} = \sqrt{(x_i - x_j)^2 + (y_i - y_j)^2 + (z_i - z_j)^2}$. $\alpha = O, W$ and $\beta = O, W$ as the solvents in which particles i and j reside, respectively. These solvents have associated dielectric constants ϵ_α and ϵ_β. The two-body electrostatic interaction between particles i(with valence v_i) and j (with valence v_j) is given as

$$U_{ij}^{\alpha\beta}(\vec{r}_{ij}) = l_{\alpha\beta}\left(\frac{v_i v_j}{r_{ij}} + \frac{\epsilon_\alpha - \epsilon_{\alpha'}}{\epsilon_\alpha + \epsilon_{\alpha'}}\frac{v_i v_j}{r_{ij'}}\delta_{\alpha\beta}\right), \tag{3.2}$$

where α' is the complementary solvent to α, $\delta_{\alpha\beta}$ is the Kronecker delta, $l_{\alpha\beta} = \frac{e^2}{4\pi\epsilon_0(\epsilon_\alpha+\epsilon_\beta)/3}$,e is the protonic charge, $\epsilon_0$is the vacuum permittivity, and $\vec{r}_j = (-x_j, y_j, z_j)$ system is placed at the liquid interface according to the method of images[**107**].

The one-body hard sphere interaction can be written as $S_i^{\alpha}(\vec{r}_i) = 0$, if LiCl ions are in water and TBATPB ions are in nitrobenzene, and there is no overlapping between the ions and the hard planes located at $x = -H$, $x = 0$, and $x = H$. Otherwise, $S_i^{\alpha}(\vec{r}_i) = \infty$. This definition prohibits ion transfer between both solvents. The one-body electrostatic interaction is associated with the self-image electrostatic energy, which is defined as

$$U_i^{\alpha}(\vec{r}_i) = \frac{l_{\alpha\alpha}}{2}\frac{\epsilon_{\alpha} - \epsilon_{\alpha'}}{\epsilon_{\alpha} + \epsilon_{\alpha'}}\frac{v_i^2}{r_{ii'}}. \tag{3.3}$$

Here, $\alpha = O, W$ is the medium in which ion i is located, and α' is the complementary solvent[**107**]. The one-body and two-body interactions can be written as

$$H_i^{one-body}(\vec{r}_i) = S_i^{\alpha}(\vec{r}_i) + U_i^{\alpha}(\vec{r}_i) \tag{3.4}$$

and

$$H_{ij}^{two-body}(\vec{r}_{ij}) = S_{ij}(\vec{r}_{ij}) + U_{ij}^{\alpha\beta}(\vec{r}_{ij}). \tag{3.5}$$

The total energy of the system is then defined as

$$H_T = \sum_{i=1}^{N} H_i^{one-body}(\vec{r}_i) + \frac{1}{2}\sum_{i=1}^{N}\sum_{j=1}^{N} H_{ij}^{two-body}(\vec{r}_{ij}), \tag{3.6}$$

where $i \neq j$, and N is the total number of particles. Electrostatics were properly included via the Torrie and Valleau's charged-sheets method[**83**] using Boda's modification[**84**].

3.2.3. Monte Carlo simulations of the liquid interface

In order to efficiently access concentrated electrolyte solutions, Monte Carlo (MC) simulations of the liquidliquid interface are performed in the NVT ensemble. This approach has been discussed in

detail in a previous study considering size-symmetric ions[**118**], so we briefly sketch it here. A box of volume $2HL^2$ is used to perform the simulations (see Fig. 3.1). Periodic boundary conditions along the y- and z-directions, and a finite length of 2H along the x-axis are imposed. The sharp dielectric interface is modeled using an uncharged hard wall at the center of the simulation box at $x = 0$. This hard wall prevents ion transfer of TBATPB ions from oil to water and LiCl ions from water to oil. In addition, two impenetrable uncharged hard walls are located at $x = -H$ and $x = H$. The simulation box must be large enough to mimic a bulk electrolyte reservoir. We have monitored this condition, obtaining the desired bulk electrolyte concentration with an error of less than 1%. The total number of particles in the simulation box varied from 2,000 for low electrolyte concentrations to 5000 for high electrolyte concentrations. In all instances, 50,000 MC cycles were performed to equilibrate the system. The canonical average was calculated using 900,000 MC cycles for low ion concentrations and 300,000 MC cycles for high ion concentrations.

3.2.4. Calculation of the electric field and the surface tension

Let us consider a distance far enough from the dielectric discontinuity, at which the electrolyte can be considered in its bulk state. We denote this distance as x_0, which is shorter than half the length of the simulation box, H, in its finite dimension (see schematic representation in Fig. 3.1). In order to mimic the effect of an applied electric field in our Monte Carlo simulations, a number of TBA^+ or TPB^- ions are added to the bulk concentration of TBATPB in nitrobenzene. The corresponding excess surface charge density can be defined as

$$\sigma_O = \int_{-x_0}^{0} \sum_{i=TBA^+,TPB^-} \rho_i(x) e z_i \mathrm{d}, \tag{3.7}$$

where $\rho_i(x)$ is the density of ions per volume unit of species i, and e is the protonic charge. Adding the same number of inorganic ions with opposite charge to the bulk concentration of LiCl in water

allows us to satisfy the global electroneutrality condition. Thus, the excess surface charge density in water is given by

$$\sigma_W = \int_0^{\infty} \sum_{i=Li^+,Cl^-} \rho_i(x) e z_i \mathrm{d} = -\sigma_O. \tag{3.8}$$

If nitrobenzene is taken as a reference, we define the integrated excess surface charge density as

$$\sigma(x) = \int_{-x_0}^{x} \sum_i \rho_i(x) e z_i \mathrm{d}, \tag{3.9}$$

for $i = TBA^+, TPB^-, Li^+, Cl^-$ and $x \leq x_0$. Applying the Gauss law, the electric field (perpendicular to the dielectric discontinuity) is given by

$$E(x) = \frac{\sigma(x)}{\epsilon(x)\epsilon_0}, \tag{3.10}$$

where $\epsilon(x) = \epsilon_O$ if $x < 0$ and$\epsilon(x) = \epsilon_W$ if $x > 0$ .From this definition, the continuity of the perpendicular electric displacement

$$D_O^{\perp} = D_W^{\perp} = \lim_{x \to 0-} \epsilon_O E(x) = \lim_{x \to 0+} \epsilon_W E(x) \tag{3.11}$$

is fulfilled, in agreement with the Maxwell equations[**107**]. The difference in the mean electrostatic potential in the bulk phases of both immiscible electrolytes, $\Delta_O^W \Psi$, is calculated from the electric field as

$$\Delta_O^W \Psi = -\int_{-x_0}^{x_0} E(x) \mathrm{d}. \tag{3.12}$$

Notice that a zero value in the bulk phase of nitrobenzene has been taken as a reference. The interfacial excess surface tension, $\gamma - \gamma_0$ (γ_0 is the surface tension at the point of zero charge), can then be obtained from the Lippmann equation 3.1.

3.3. Result and discussion

In Fig. 3.2, experimental results of the excess surface tension at the nitrobenzenewater interface [**6**], $\gamma - \gamma_0$, are collated with Monte Carlo results and theoretical calculations obtained via the non-linear PoissonBoltzmann theory[**117**] for several electrolyte concentrations. In Fig. 3.2(A), the concentration of TBATPB ions in nitrobenzene is fixed and the concentration of LiCl ions in water is varied, while in Fig. 3.2(B) the opposite process is performed, that is, the concentration of LiCl ions in water is fixed and the concentration of TBATPB ions in nitrobenzene is varied. For all salt concentrations, Monte Carlo data agree with experimental results. The non-linear PoissonBoltzmann results resemble experimental data at low electrolyte concentrations, even though they deviate significantly at large values of the difference in the mean electrostatic potential in the bulk phases of the electrolytes, $\Delta_O^W \Psi$. These deviations are magnified at higher concentrations, contrasting with the good agreement between the Monte Carlo simulations and the experimental results.

In Fig. 3.3, the electric field and the ion distribution around the liquid interface are presented for several concentrations of LiCl ions in water, while the concentration of TBATPB ions in nitrobenzene is fixed. In Fig. 3.2(B), a positive excess surface charge density in oil, $\sigma_O > 0$, is considered, while the opposite value, $\sigma_W = -\sigma_O$, is considered in water. For all LiCl concentrations, the contact value of Cl_- is larger than the contact value of Li^+ (see Fig. 3.3(B)). This is consistent with the fact that the negative Cl ions are counterions of the positive excess surface charge in nitrobenzene, $\sigma_O > 0$. On the other hand, a very interesting behavior of the electric field

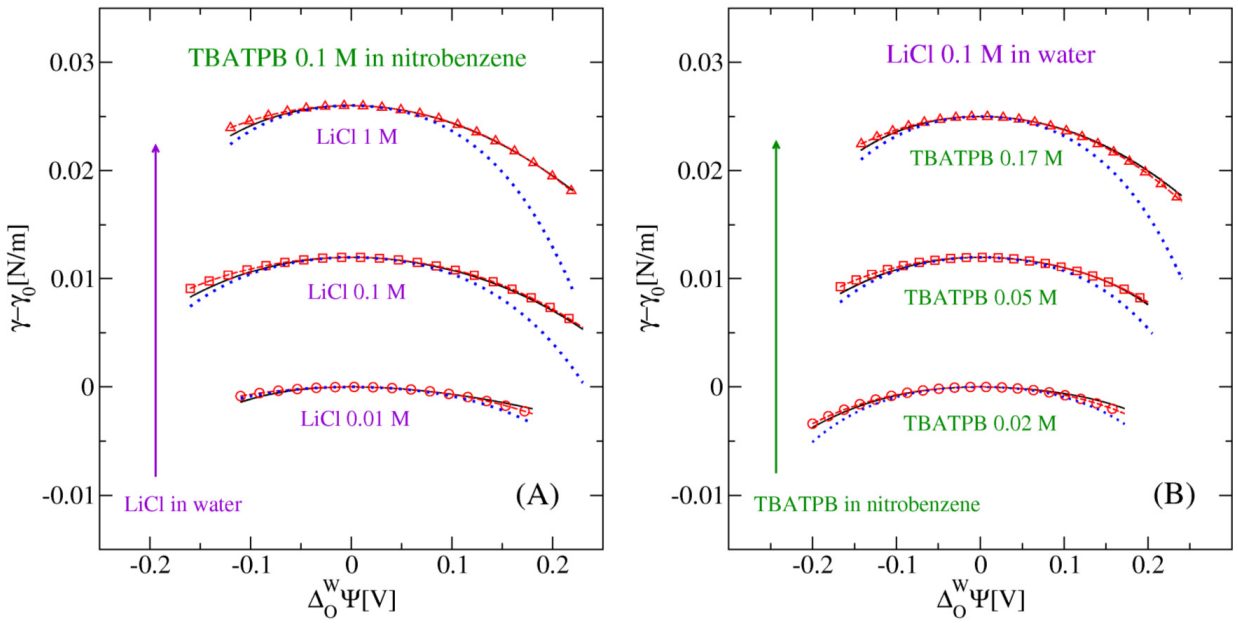

Figure 3.2. Excess surface tension, $\gamma - \gamma_0$, at the oilwater interface as a function of the difference in the mean electrostatic potential in the bulk phases of both immiscible electrolytes, $\Delta_O^W \Psi$, for several electrolyte concentrations. g0 is the surface tension at the point of zero charge. In (A), the bulk concentration of TBATPB in nitrobenzene is 0.1 M in all instances, while the bulk concentration of LiCl in water is (from bottom to top) 0.01 M, 0.1 M, and 1 M. In (B), the bulk concentration of LiCl in water is 0.1 M in all cases, while the bulk concentration of TBATPB in nitrobenzene is (from bottom to top) 0.02 M, 0.05 M, and 0.17 M. Black solid and blue dotted lines correspond to the experimental electrocapillary data reported in ref. [**6**], and non-linear PoissonBoltzmann calculations, respectively. Red empty symbols with dashed lines correspond to Monte Carlo simulation results. The excess surface tension is shifted for clarity.

in water can be observed in Fig. 3.3(A) when the concentration of LiCl increases. Near the dielectric discontinuity, the electric field peaks at the closest approach distance of $Cl\_$ when the salt concentration of LiCl increases. As the dielectric constant is larger in water than in nitrobenzene ($\sigma_W = -\sigma_O$), the electrostatic screening in water should be larger accordingly. Nevertheless, in Fig. 3.3(A) we observe that the magnitude of the electric field in water can be even larger than its maximum value in nitrobenzene for the highest salt concentration. This behavior can be understood noting that there is a significant amount of small positive Li^+ ions adsorbed to the dielectric

interface at high electrolyte concentrations. These adsorbed cations, which are co-ions of the positive excess surface charge density in nitrobenzene, $\sigma_O > 0$, enhance significantly the electric field in the aqueous phase near the liquid interface.

In Fig. 3.3(D), the ion profiles of organic and inorganic ions are displayed as a function of the distance to the dielectric discontinuity. In this case, a negative excess surface charge density in oil, $\sigma_O < 0$, is considered, while the opposite value, $\sigma_W = -\sigma_O$, is considered in water. For electrolyte concentrations 0.01 M and 0.1 M of LiCl, the contact values of Li^+ are larger than those of Cl^- . This is consistent with the fact that positive Li^+ ions are counterions of the negative excess surface charge density, $\sigma_O < 0$, in nitrobenzene. Nevertheless, at a concentration 1 M of LiCl, the previous trend inverts: the contact value of large Cl^- ions (co-ions of the negative excess surface charge in nitrobenzene, σ_O) is larger than the contact value of small Li^+ cations (which are the counterions of σ_O). The inversion of roles between counterions and co-ions is the so-called charge inversion[**111, 119**]. The overcompensation of the negative excess surface charge in nitrobenzene promotes a reversal of the electric field in water, which peaks again at the closest approach distance of Cl^- (see Fig. 3.3(C)).

The significant adsorption of Li^+ ions to the liquid interface at high electrolyte concentrations is mainly due to the ionic size asymmetry and excluded volume effects (or depletion forces). This behavior occurs for both polarities of the difference in the mean electrostatic potential in the bulk phases of the electrolytes, $\Delta_O^W \Psi$, in the presence of weak electric fields. Under these conditions, small cations (Li^+) can be significantly adsorbed to the liquid interface in a region that is not allowed to large anions (Cl^-) in water. If the smallest ions are counterions of the excess surface charge density in nitrobenzene, σ_O, this adsorbed layer of small counterions can overcompensate σ_O near the dielectric discontinuity, generating the so-called charge reversal[**111**] and the inversion

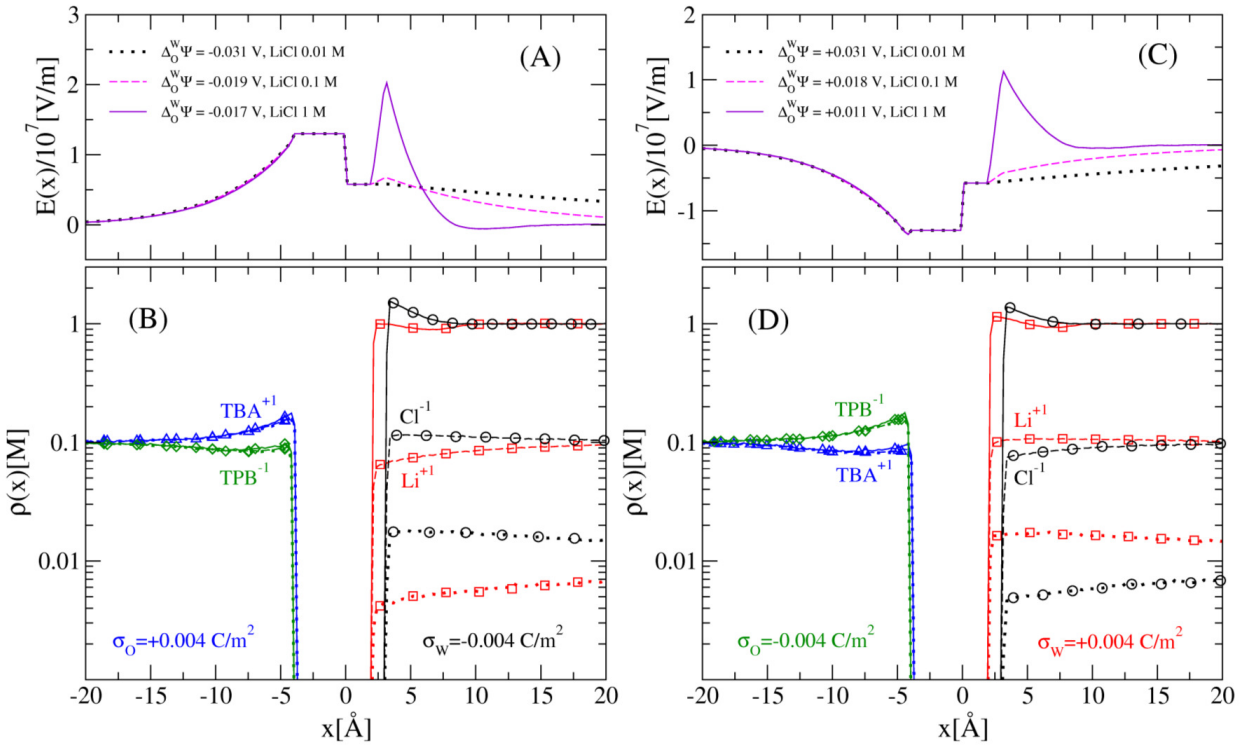

Figure 3.3. Monte Carlo calculations of the electric field and ion distribution as a function of the distance to the oilwater interface. The bulk concentration of TBATPB in nitrobenzene is 0.1 M in all instances, while the bulk concentration of LiCl in water is 0.01 M (dotted lines), 0.1 M (dashed lines) and 1 M (solid lines) for all panels. In (B) and (D), Li^+, Cl^-, TBA^+ and TPB^- are represented by squares, circles, triangles, and diamonds, respectively. In (A) and (B), the excess surface charge density in water is negative, $\sigma_W = -0.004 C/m^2$, while in (C) and (D), the excess surface charge density in water is positive, $\sigma_W = +0.004 C/m^2$. The difference in the mean electrostatic potential in the bulk phases of both immiscible electrolytes, $\Delta_O^W \Psi$, is displayed in the insets of (A) and (C) for each ionic concentration.

of the electric field in the aqueous region (see Fig. 3.3(C)). In contrast, if the smallest ions are co-ions of σ_O then the net excess surface charge density in water can be larger than σ_O close to the dielectric discontinuity, producing the phenomenon of surface charge amplification[**111**] and the enhancement of the electric field (see Fig. 3.3(A)).

Finally, the interfacial behavior of the electric field for larger excess surface charge densities in water, σ_W, is displayed in Fig. 3.4(A) and (B). In order to facilitate the comparison of our results with future experimental data, the corresponding differences in the mean electrostatic potential in

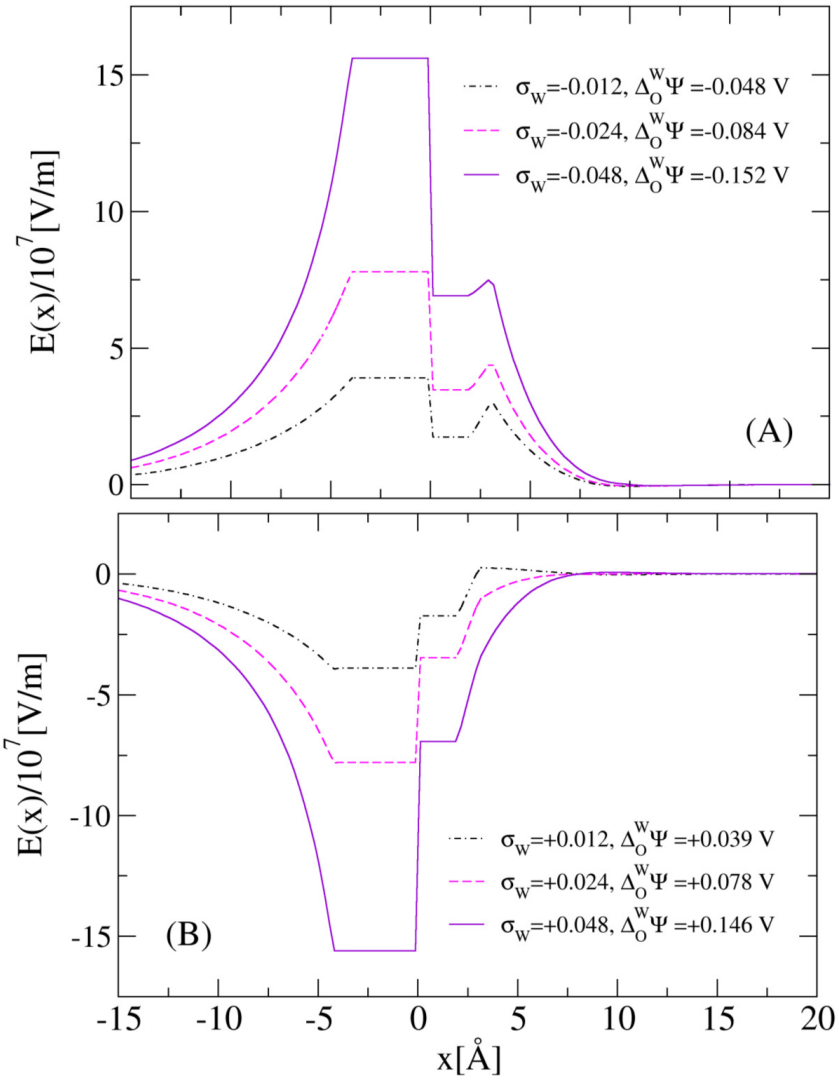

Figure 3.4. Monte Carlo calculations of the electric field as a function of the distance to the oil-water interface for several excess surface charge densities, sW, in water. The bulk concentration of TBATPB in nitrobenzene is 0.1 M and the bulk concentration of the LiCl in water is 1 M, in both panels. The difference in the mean electrostatic potential in the bulk phases of both immiscible electrolytes, $\Delta_O^W \Psi$, is displayed in the insets of (A) and (B) for each excess surface charge density in water.

the bulk phases of both immiscible electrolytes, $\Delta_O^W \Psi$, are also displayed for each ionic concentration of LiCl in water. In Fig. 3.4(A), we observe that even though the enhancement of the electric

field still persists for large negative differences of the mean electrostatic potential, $\Delta_O^W \Psi$, its magnitude is less pronounced. This means that the increase of positive excess charge in nitrobenzene increases the electrostatic repulsion exerted over Li^+ cations in water, thus gradually overcoming the attraction of Li^+ ions to the interface due to excluded volume effects. In contrast, Fig. 3.4(B) shows that the reversal of the electric field disappears at large positive differences in the mean electrostatic potential in the bulk phases of both immiscible electrolytes, $\Delta_O^W \Psi$.

3.4. Conclusion

In this study, we provide an enhanced description of the ion distribution and the electric field near a liquidliquid interface, including realistic ionic size-asymmetry, ion correlations, excluded volume of ions, and image charge effects via Monte Carlo simulations. This approach goes well beyond the classical PoissonBoltzmann picture, in which such effects are completely neglected. The adequacy of this treatment is demonstrated via a comparison with experimental results of the excess surface tension at the nitrobenzene-water interface, without needing any adjustable parameter. We observe that the non-linear PoissonBoltzmann theory is limited to low electrolyte concentrations, deviating significantly from experimental results in the opposite limit. We have also evinced that the ionic size-asymmetry and excluded volume effects play fundamental roles in the structure of the electrical double layer around a liquidliquid interface at high electrolyte concentrations. In particular, we have shown that at a 1 M concentration of LiCl in water and a 0.1 M concentration of TBATPB in nitrobenzene, the significant adsorption of small Li+ ions to the liquid interface is able to (i) enhance the electric field in the aqueous phase for positive excess surface charge densities in nitrobenzene and (ii) reverse the electric field in the aqueous phase for negative excess surface charge densities in nitrobenzene. These phenomena are analogous to the surface

charge amplification and charge inversion reported by our research group in size-asymmetric electrolytes around a charged nanoparticle (even in the absence of image charge effects)[**111**]. In that study, we showed that the surface charge amplification (or the adsorption of coions on the surface of a charged nanoparticle increasing its original bare charge) and the charge inversion (or the overcompensation of the original bare charge of the nanoparticle by counterions) can appear at high ion concentrations in the vicinity of the point of zero charge. We demonstrated that these effects are mainly driven by the ionic size asymmetry and excluded volume effects, and that they disappear at large valences of the nanoparticle. Here, we have shown that an analogous mechanism can produce the enhancement and the inversion of the electric field at a liquid interface near the point of zero charge (that is, for small differences in the mean electrostatic potential in the bulk phases of both immiscible electrolytes). These findings emphasize the relevance of the proper inclusion of ionic size-asymmetry, ion correlations and image charge effects in the description of the diffuse ionic distribution around charged surfaces and interfaces.

It is important to point out that these phenomena are not limited to occur only when an electric field is applied. The use of an electric field is one possibility to produce ionic charge accumulation at a liquid interface. In fact, such an ion distribution can also be induced by other mechanisms, such as ion partitioning, in which ions move from one liquid medium to another depending on their standard Gibbs energy of transfer [**120**] or via molecular pumps in cells [**121**]. These mechanisms are highly non-equilibrium processes since the ion's mobility and the resulting induced polarizability respond at different time scales [**5**]. As the distribution of ions around fluid interfaces is a common scenario in biological systems, our findings suggest that interesting phenomena such as the enhancement and reversal of the electric field, as well as the surface charge amplification [**111, 112**] and charge inversion (already observed experimentally in macroscopic colloidal systems [**40, 113, 114**] may also be present in nanoscopic biological liquid interfaces. We have

also shown how the tuning of the electric field, enhancing or reversing its strength near the liquid interface, depends on the ion concentration and ionic size asymmetry. This suggests a new reversible physical mechanism to control the adsorption, self-assembly, and trapping/release of small charged nanoparticles, globular proteins, dendrimers or polyelectrolytes at the interface between two immiscible liquids in the presence of weak electric fields. Experimental techniques of atomic resolution [**122, 123**] and recent theoretical improvements [**124, 42, 42**] will play an important role in gaining further insights into these phenomena at the molecular level.

CHAPTER 4

Effects of size asymmetry and electric field on ion distribution at polarized interfaces by coarse grained molecular dynamics simulations

4.1. Introduction

Inorganic metal-oxygen clusters anions, called polyoxometalates (POMs), represent an important class of compounds with remarkable fundamental structural functionality, such as catalysis, electron transfer in solution and at metal oxide interfaces, self-assembly and association with biological systems[**125, 126, 127**]. The tunability of their size, structure, and elemental composition render them particularly interesting for design of functional nanomaterials. In most circumstances, POMs inhabit in solutions in contact with solid or liquid interfaces. A precise understanding of such complex system requires an analysis of the surrounding solvent, local ionic organization and the structure of POMs themselves. Considering their high negative charge, large size, and their chemical properties, it is very challenging to model and simulate POMs effectively.

In the following part, we start with a coarse-grained model that consider POMs as large highly charged anions while with relatively small cations in the the aqueous solution. We study the effects of size asymmetry and charge asymmetry on ion distribution at a dielectric interface using coarse-grained MD developed in section 1.3. The goal is to explore charge amplification with exact consideration of surface polarization. In particular, we choose POM as large anions (e.g. $[PW_{12}O_{40}]^{3-}$, for which force fields are available), and compare with smaller anions (e.g. Cl^{-}). Different cations of similar sizes but different valence are studied.

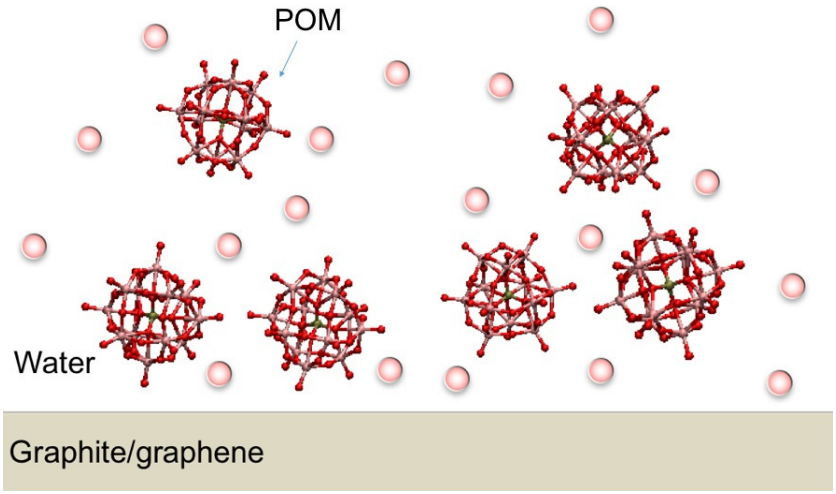

Figure 4.1. Schematic of the coarse grain simulation of ion distribution, and atomic details of the large keggin ion by MD.

4.2. Model and simulation setup

We study $X_x[PW_{12}O_{40}]_y$ solution at 300 K using a Nose-Hover chain, with concentrations of 0.1 M. We choose to study K^+ and Eu^{3+} as the metal cation X. We also compare $[PW_{12}O_{40}]^{3-}$ with Cl^-, a smaller anion. The diameter of $[PW_{12}O_{40}]^{3-}$, K^+ , Eu^{3+}, and Cl^- are listed in Table 4.1. To separately investigate the effects of size asymmetry, charge asymmetry, strength of ion correlation and volume fraction, we study the cases listed in Table 4.2.

The box size is 7.14 nm $\times$ 7.14 nm with periodic boundary conditions in x- and y- directions. The z- direction is divided into three parts by two hard walls with permittivity of $\epsilon_1 = 15$, $\epsilon_2 = 80$, and $\epsilon_3 = 80$, respectively. $\epsilon_1 = 15$ is corresponding to graphite and $\epsilon_3 = 80$ is corresponding to water. Ions are confined between the two walls, and the distance between the walls is 30 nm, which is much larger than the Debye length. Ewald summation is used for long-range electrostatic interactions[**128**]. To account for non-periodicity of the z-direction, dipole correction is applied, and the box size in the z-direction is three times larger than the distance between the walls[**129**].

Table 4.1. Ion diameter[**1, 2**]

Ion	$[PW_{12}O_{40}]^{3-}$	K^+	Eu^{3+}	Cl^-
Diameter (nm)	1.12	0.24	0.24	0.24

Table 4.2. Ion sizes, ion charges and volume fraction for 7 cases.

Case ID	Cation diameter/anion diameter (nm)	Cation charge/anion charge	Volume fraction
(a)	0.24/0.24	+1/-1	0.00087
(b)	0.24/1.12	+1/-1	0.045
(c)	0.24/0.24	+3/-3	0.00087
(d)	0.24/1.12	+3/-3	0.045
(e)	0.24/0.24	+1/-3	0.0017
(f)	0.714/0.714	+1/-3	0.046
(g)	0.24/1.12	+1/-3	0.046

The hydrophobic interactions between ions, and between ions and the interfaces are modeled using repulsive Lenard-Jones (LJ) interactions:

$$V_{LJ} = \begin{cases} 4\epsilon \left[\left(\frac{\sigma}{r}\right)^{12} - \left(\frac{\sigma}{r}\right)^{6} \right] + \epsilon & \text{for } r \leq 2^{\frac{1}{6}}\sigma \\ 0 & \text{for } r > 2^{\frac{1}{6}}\sigma \end{cases} \tag{4.1}$$

The timestep is 1 fs. The system is equilibriated for 1 ns before data-collecting simulations.

4.3. Result and discussion

The results of ion distribution for cases (a) and (b) are shown in Figure 4.2. In both cases, the charge ratio is +1/-1. When the cation/anion sizes are 0.24 nm/0.24 nm, both cations and anions are depleted from the interface, while when the cation sizes are 0.24 nm/1.12 nm, the large anions aggregate at the interface and the small cations are depleted further from the interface.

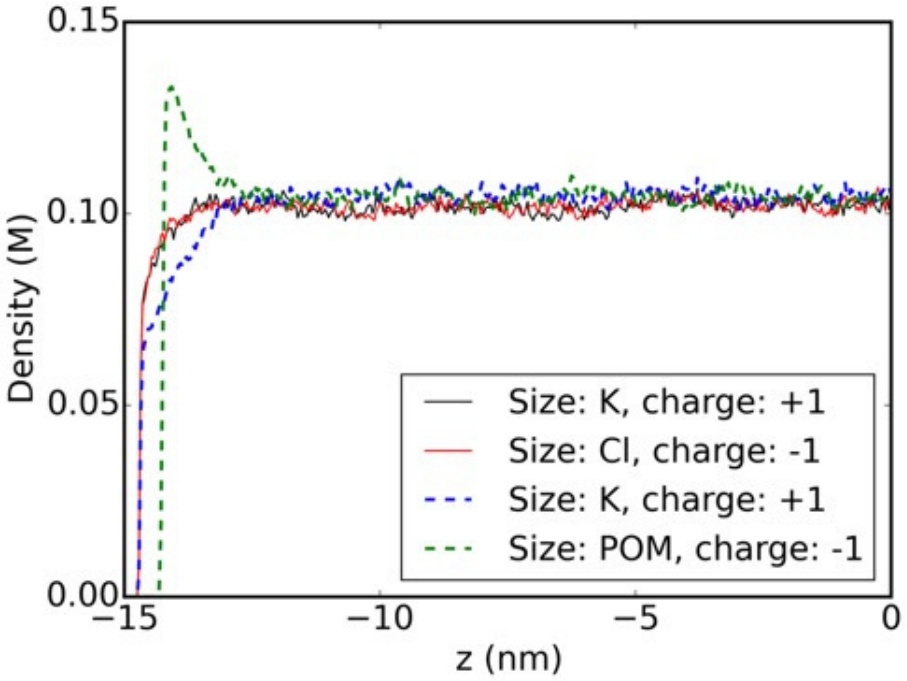

Figure 4.2. Ion distribution for 0.1 M salt at the $\epsilon_1/\epsilon_2 = 15/80$ interface with charge ratio of +1/-1, and cation/anion sizes of 0.24 nm/0.24 nm (solid lines) and cation/anion sizes of 0.24 nm/1.12 nm (dashed lines).

To understand the mechanisms for the ion distributions, we point out that the forces acting on an ion at a dielectric interface can be divided into three categories: steric interactions, ion-ion correlation and surface polarization-ion interactions[**130**]. To investigate the separate effects of the three types of forces on the ion distribution, we simulate the cases with only steric effects by removing charges from the ions, and only steric effects and ion correlation by making 1 = 2 = 80. As shown in Figure 4.3, when there are only steric effects, both cations and anions aggregate at the interface. This is because when uncharged ions are close to interfaces, they feel more collision against the interface than from the interface, leading to an entropic force pushing the ions towards the interface[**131**]. Note the pure steric effects are more pronounced at higher volume fractions. While when ions have a charge ratio of +1/-1 but $\epsilon_1 = \epsilon_2 = 80$ more of large anions aggregate at the interfaces, and small cations start to deplete from the interfaces. The depletion at interfaces

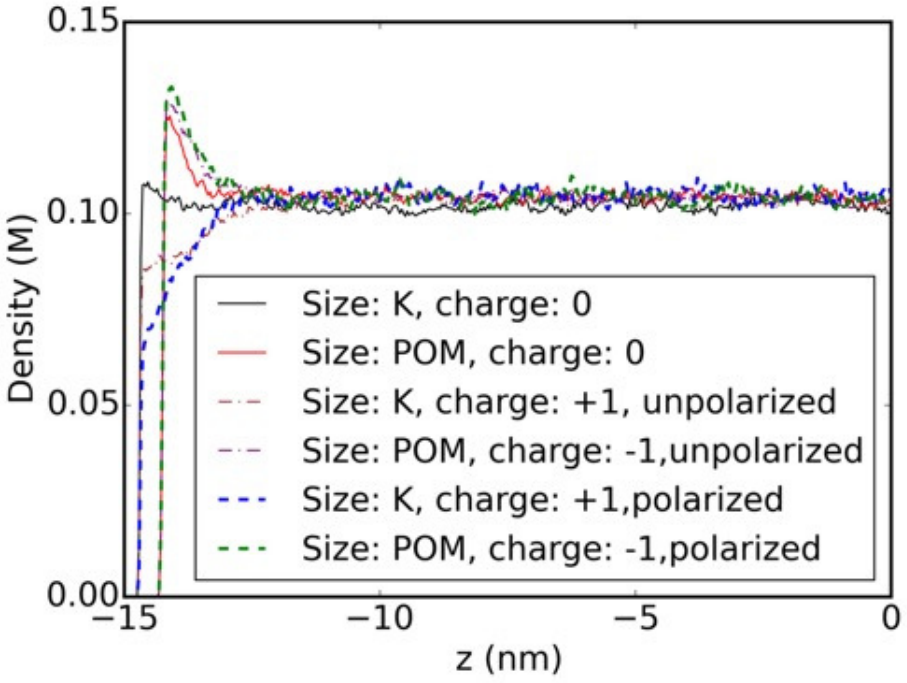

Figure 4.3. Ion distribution for 0.1 M salt, cation/anion sizes of 0.24 nm/1.12 nm, and charge ratio of 0/0 (solid lines), charge ratio of +1/-1 and $\epsilon_1 = \epsilon_2 = 80$ (dashed dot lines) and charge ratio of +1/-1 and $\epsilon_1 = 15$ and $\epsilon_2 = 80$ (dashed lines).

is due to ion-ion correlation[**130**]. The size asymmetry induces a net force on the small cations, making cations to deplete from the interface. On the other hand, steric effects prevail for larger anions since they have a larger volume fraction. The aggregation of large anions is even elevated when ion correlation is present, because depletion of small cations from the interface enhances the entropic depletion force that pushes large anions towards the interface. When $\epsilon_1 = 15$ and $\epsilon_2 = 80$, the interface polarization repels ions approaching the interface. Since small cations approach the interfaces closer than large anions, the polarization is dominated by the small cations. As a result, small cations are more depleted comparing with non-polarized interfaces, and large anions are more aggregated. This analysis indicates that the depletion of small cations in Figure 4.2 stems from ion correlation and interface polarization; while the aggregation of large anions results from steric effects.

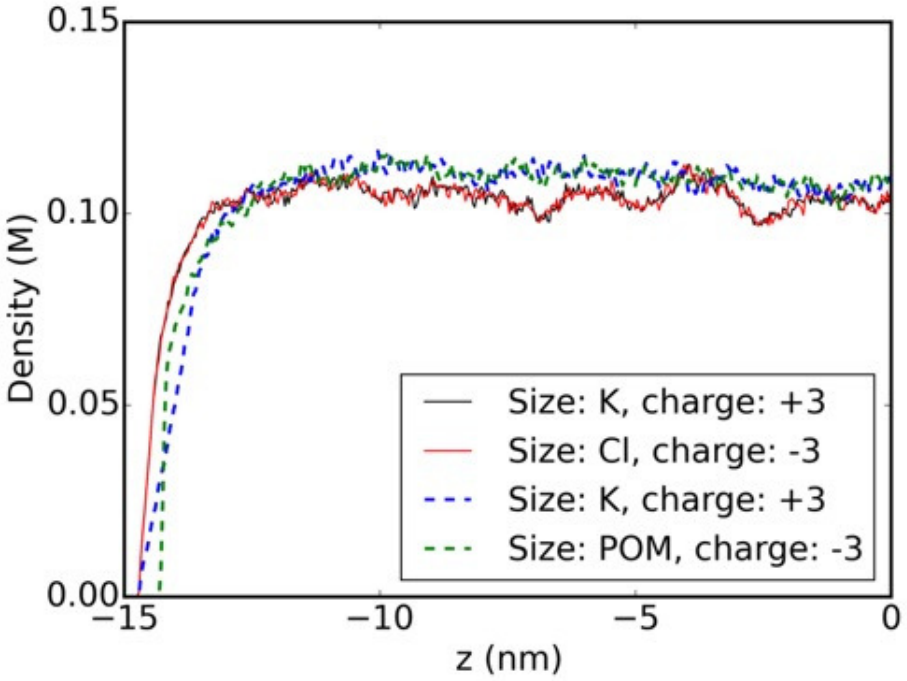

Figure 4.4. Ion distribution for 0.1 M salt at the 1/2 = 15/80 interface with charge ratio of +3/-3, and cation/anion sizes of 0.24 nm/0.24 nm (solid lines) and cation/anion sizes of 0.24 nm/1.12 nm (dashed lines).

We also study stronger ion correlations by simulating the charge ratio of +3/-3, in cases (c) and (d). As is shown in Figure 4.4, when the cation/anion sizes are 0.24 nm/0.24 nm, both cations and anions are depleted from the interface, similar to what we observe in case (a) in Figure 4.2. On the other hand, for cation/anion sizes of 0.24/1.12 nm (case (d)), both types of ions are depleted from the interface. This is different from case (b) in Figure 4.2, where large anions are aggregated at the interface. The depletion of large anions at interfaces in case (d) is not surprising, because of stronger ion-ion correlations in this case. We note that the ion distribution for case (c) is rougher than in cases (a), (b) and (d). This is possibly because strongly correlated cations and anions bind to neutral clusters that reduces the effective degrees of freedom.

To separately study the effect of charge asymmetry, we study the cases when cations and anions have the same sizes, but charge ratio +1/-3. The results are shown in Figure 4.5. Note that the

density of cations is scaled by 1.0/3.0 for comparison. When cations and anions are both as small as 0.24, cations are closer to the interface than anions, although both types of ions are depleted from the interface. This is because anions are three times more charged than cations, they are more repelled by polarization, which in turn attracts the cations[**132**]. Similarly, cations are closer to the interface than anions when sizes of both types of ions is increased to 0.714 nm (case (f)). However, there is a peak for both types of ions, though at separate locations. Figure 4.6 shows charge density distribution at the interface, showing a double layer without directly charging the interface. We note the volume fraction in case (f) is the same as in case (b) (Table 4.2), where steric effects are important, which explains why ions start to aggregate in case (f).

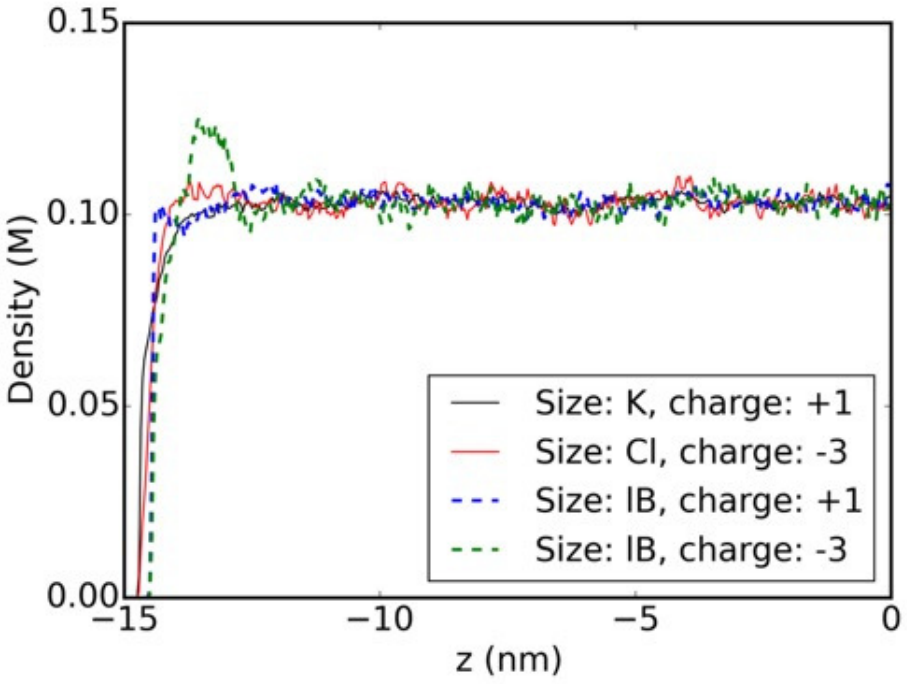

Figure 4.5. Ion distribution for 0.1 M salt at the $\epsilon_1/\epsilon_2 = 15/80$ interface with charge ratio of +1/-3, and cation/anion sizes of 0.24 nm/0.24 nm (solid lines) and cation/anion sizes of 0.714 nm/0.714 nm (dashed lines).

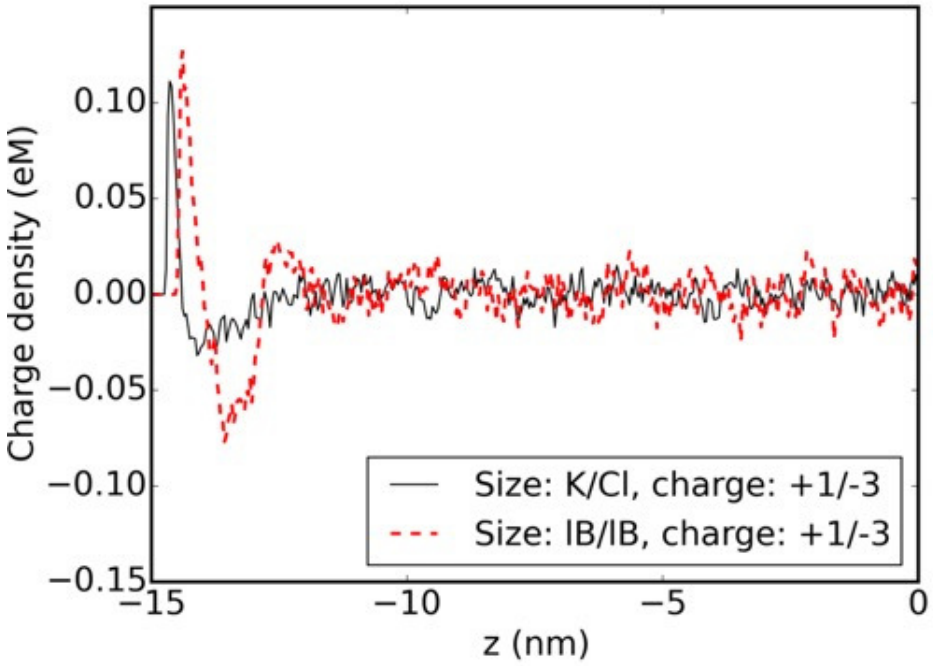

Figure 4.6. Charge density distribution for 0.1 M salt at the $\epsilon_1/\epsilon_2 = 15/80$ interface with charge ratio of +1/-3, and cation/anion sizes of 0.24 nm/0.24 nm (solid lines) and cation/anion sizes of 0.714 nm/0.714 nm (dashed lines).

We take a step further and introduced both size and charge asymmetry in case (g). In Figure 4.7, comparing with case (b), where there is only size asymmetry, the aggregation peak of large anions for case (f) are bended and higher than case (b). This is a result of stronger repulsion from interface polarization, as well as stronger ion-ion correlation for +1/-3 charge ratio.

4.4. Summary

In this section we have studied ion distribution at dielectric interfaces using coarse-grained MD based on the energy functional considering polarization. We find that both size asymmetry and charge asymmetry lead to charge separation (Figure 4.6) at the interfaces. In addition, charge separation is enhanced by interface polarization. We are currently extending the research to charged interfaces that has broad applications such as batteries and supercapacitors for energy

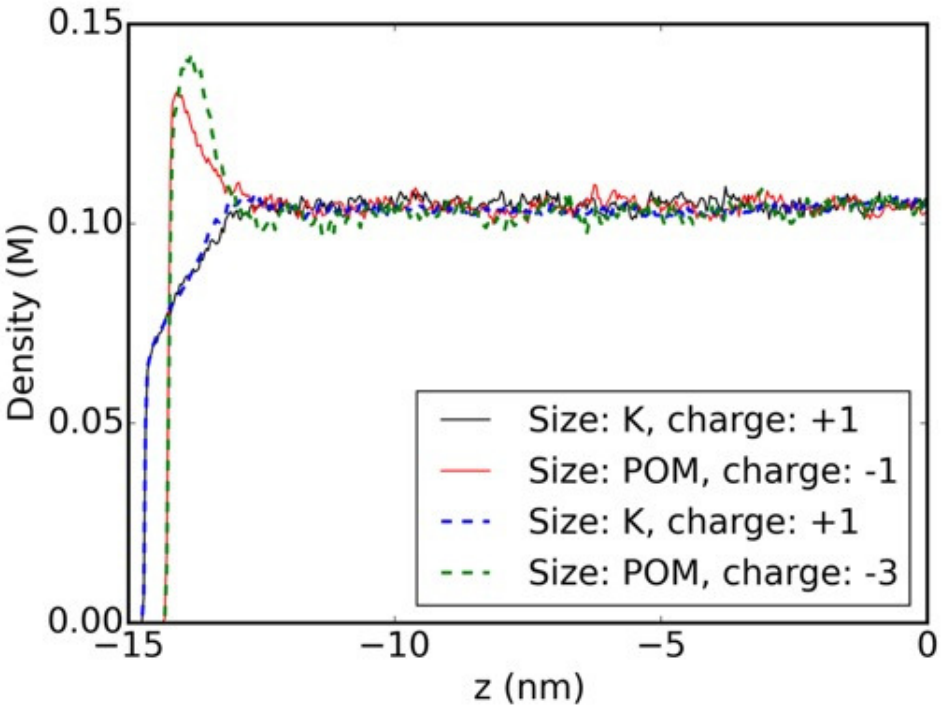

Figure 4.7. Ion distribution for 0.1 M salt at the $\epsilon_1/\epsilon_2 = 15/80$ interface with cation/anion sizes of 0.24 nm/1.12 nm and charge ratio of +1/-1 (solid lines) and charge ratio of +1/-3 (dashed lines).

storage. In fact, charge separation (Figure 4.6) found at neutral interfaces serves as a fundamental basis for charge amplification at charged interfaces. The MD simulations can also be adapted to study dynamic processes such as charging/uncharging processes. Another direction is curved interfaces that are ubiquitous in biological systems, where polarization plays a more important role. This line of studies will provide the foundation for the studies of self-assembly of colloids and biological building blocks.

CHAPTER 5

Summary and Future works

5.1. Summary

The structural and dynamical properties of many biological and synthetic soft materials are determined by the interaction between the constituent macromolecules which is often dependent on the nature of the ionic structure near the macromolecular surfaces. Coarse-grained models of these materials involve ions in an environment consist of piecewise-uniform dielectric media separated by thin boundaries. A key obstacle in finding the ion distributions in such models via numerical simulation is the need to solve the Poisson equation at every simulation step.

The ultimate goal of my PhD project was to develop modeling and simulation approaches to simulate electrostatic problems with dielectric heterogeneities for the understanding of ionic structure near interfaces and underlying physical mechanism throughout the course of this program. Car-Parrinello molecular dynamics simulation method is designed specifically to efficiently simulate charges in the presence of inhomogeneous dielectric response and accurately extract their density profiles. This method is founded based on an energy functional of the induced charge density that enables the replacement of the expensive solution of the Poisson equation at each simulation step with an on-the-fly computation of polarization effects. It demonstrates many features of this method including the tracking of exact induced density at all times, excellent energy conservation, and accurate implementation of constraints stemming from Gauss law.

I have implemented the code including long-range correction designed for one arbitrary interface and two or more interfaces. Ion distributions is computed in a variety of models: ions confined

between two planar dielectric interfaces, size-asymmetric ions near interfaces with/without electric field and ions in two liquid-liquid spherical water droplet immersed in oil. The effect of different dielectric contrasts, ion concentrations, ion valencies, external electric field and different interfacial on the ion distributions is systematically studied. In addition, I investigate the ionic structure and electric field at the oil-water interface with size-asymmetric monovalent ions using Monte Carlo simulation based on image charge method. It showed that the ionic size asymmetry between small cations and large anions can significantly increase or reverse locally the electric field near a liquid-liquid interface at high salt concentrations. This suggests a robust ionic trapping/release mechanism at oil-water interfaces.

5.2. Future works

5.3. Ion transport in nanochannel

If charged interfaces immersed in an electrolyte solution, compensating opposite counterions will accumulate near the interfaces and co-ions are electrostatically repelled. This screening effect will result in the formation of double layer and the electrostatic effects will decays to its bulk value over a characteristic length. The characteristic length is known as the Debye length. In aqueous solutions it is typically 1-100 nanometers and it decreases with increasing concentration of the electrolyte. In microfluidics, the Debye length is usually much smaller than the systems dimensions, and the bulk of the solution is shielded from the surface charge. Nanofluidics is the study and application of fluid flow in channels/pores with at least one characteristic dimension below 100nm [**133, 134, 135**]. Compared with traditional microfluidics, nanofluidics exhibits several novel transport phenomena at nanoscale which result from some unique features. For example, the high surface to volume ratio results in capillarity-induced negative pressure in wate [**136**]. The small characteristic length of nanochannel leads to electrical double layers overlapping and

thereby results in ion transport manipulating [**137, 138, 139**]. The proximity of system dimension and the size of important biomolecules like DNA give rise to selective molecule transport and DNA separation [**140, 141**]. Given these unique features, nanofluidic devices have been used for many chemical or biological applications, such as biosensors [**142, 143, 144, 145**], water desalinization [**146, 147**], and energy conversion/storage [**148, 149**].

A pressure driven flow through a microfluidic or nanofluidic channel will bring the ions in the diffuse layer downstream, thus generating an electrical current[**150**]. This phenomenon can potentially be harnessed for mechanical-to-electrical energy conversion. Alternatively, electrical-to-mechanical energy conversion is possible by applying an electric field across the length of the nanochannel, thereby driving fluid through by electroosmosis. However, current flow through nanofluidic channels at a given pressure, or source-drain voltage, is severely limited due to the no-slip boundary condition that characterizes most such systems. The reason that no-slip boundary condition has a lower energy conversion efficiency is that there is no fluid or ion flow at the surface, where the counter-ion concentration is the highest [**150**]. If the no-slip boundary condition in nanochannels could be surmounted, greatly enhanced streaming currents and energy conversion efficiencies would be possible, making energy conversion in such systems far more feasible.

The ionic structure of the confinement systems in our earlier work intrigue us to study the ionic transport properties in nanometer-sized dielectric confined systems. Nanofluidics systems like nanochannels , which have one dimension comparable to or even smaller than the Debye length, possess an electrostatic potential that can be significantly modulated by soft ionic structure inside and on the other side, external field and dielectric heterogeneity will affect the transport properties dramatically. The nanometer scale of the structure allows the discovery of a new range of phenomena that has not been possible in traditional microfluidics. Most of the present studies on nanofluidics only deal with a simple symmetric monovalent electrolytes because it is a simple

physical system that can be easily understood by Poisson Boltzmann theory. However, real applications may involve multivalent ion species as well as the dielectric interfaces. We need to figure out how fluid and ions flow through nanochannels and in what ways such transport differs from expectations based on classical hydrodynamics and the Poisson-Boltzmann equation. The effect of correlations, finite size of molecules, hydrogen bonding and other short range interactions are all expected to play a role in understanding of fluid flow and ion transport. Including ion correlations, finite size of molecules and dielectric heterogeneity, our MD simulations do not use any adjustable parameters, and should in principle yield numerically exact results for the primitive model. We note that our simulations, which based on a true energy functional, are versatile enough to treat the case of multiple and curved interfaces, multivalent salts, asymmetric ion sizes to study the dynamical evolution of the soft ionic structure. Therefore, one direction of next step is to use our CPMD method to study the ionic transport properties of electrolytes under dielectric confinement and understand how different concentrations, multivalency, dielectric heterogeneity etc influence the transport properties in confinement systems, which will give valuable information for manipulating and designing relevant nanofluidic devices.

The MD simulation of ion transport presents several problems. The first problem regards the time scale. The translocation of a single ion across a typical ion channel takes place on the order of a microsecond, which is extremely long compared to the typical length of a calculation trajectory. Because it is impractical to simulate the entire ion and solvent penetration through nanoscale channels by using non-equilibrium MD simulations, some other process to simulate must be chosen. The second problem is how to deal with thermostat dynamically when there is an external pressure/electric field. This last problem frames the difficulty in identifying the process to simulate. At last, hydrodynamics needs to be taken into consideration for liquids under confinement.

Bibliography

[1] Paul Chi Fu. Pau, J. O. Berg, and W. G. McMillan. Application of stokes' law to ions in aqueous solution. *The Journal of Physical Chemistry*, 94(6):2671–2679, 1990.

[2] Michael T. Pope and Gideon M. Varga. Heteropoly blues. i. reduction stoichiometries and reduction potentials of some 12-tungstates. *Inorganic Chemistry*, 5(7):1249–1254, 1966.

[3] K. Nygård, R. Kjellander, S. Sarman, S. Chodankar, E. Perret, J. Buitenhuis, and J. F. van der Veen. Anisotropic pair correlations and structure factors of confined hard-sphere fluids: An experimental and theoretical study. *Phys. Rev. Lett.*, 108:037802, Jan 2012.

[4] Kim Nygård, Sten Sarman, and Roland Kjellander. Local order variations in confined hard-sphere fluids. *The Journal of Chemical Physics*, 139(16):–, 2013.

[5] Jos W. Zwanikken and Monica Olvera de la Cruz. Tunable soft structure in charged fluids confined by dielectric interfaces. *Proceedings of the National Academy of Sciences*, 110(14):5301–5308, 2013.

[6] Kakiuchi Takashi and Senda Mitsugi. Structure of the electrical double layer at the interface between nitrobenzene solution of tetrabutylammonium tetraphenylborate and aqueous solution of lithium chloride. *Bulletin of the Chemical Society of Japan*, 56(6):1753–1760, 1983.

[7] Luis G. Morelli, Koichiro Uriu, Saúl Ares, and Andrew C. Oates. Computational approaches to developmental patterning. *Science*, 336(6078):187–191, 2012.

[8] B. Honig and A. Nicholls. Classical electrostatics in biology and chemistry. *Science*, 268(5214):1144–1149, 1995.

[9] Yan Levin. Strange electrostatics in physics, chemistry, and biology. *Physica A: Statistical Mechanics and its Applications*, 352(1):43 – 52, 2005.

[10] David E. Clapham. Calcium signaling. *Cell*, 131(6):1047 – 1058, 2007.

[11] Bob Eisenberg. Ionic interactions in biological and physical systems: a variational treatment. *Faraday Discuss.*, 160:279–296, 2013.

[12] Jean-Pierre Hansen and Hartmut Löwen. Effective interactions between electric double-layers. *Annual Review of Physical Chemistry*, 51(1):209–242, 2000. PMID: 11031281.

[13] Lars Guldbrand, Bo Jönsson, Håkan Wennerström, and Per Linse. Electrical double layer forces. a Monte Carlo study. *The Journal of chemical physics*, 80(5):2221–2228, 1984.

[14] Per Linse and Vladimir Lobaskin. Electrostatic attraction and phase separation in solutions of like-charged colloidal particles. *Physical review letters*, 83(20):4208, 1999.

[15] Zhigang Suo. Mechanics of stretchable electronics and soft machines. *MRS Bulletin*, 37:218–225, 3 2012.

[16] Francisco J. Solis, Graziano Vernizzi, and Monica Olvera de la Cruz. Electrostatic-driven pattern formation in fibers, nanotubes and pores. *Soft Matter*, 7:1456–1466, 2011.

[17] Roger H French, V Adrian Parsegian, Rudolf Podgornik, Rick F Rajter, Anand Jagota, Jian Luo, Dilip Asthagiri, Manoj K Chaudhury, Yet-ming Chiang, Steve Granick, et al. Long range interactions in nanoscale science. *Reviews of Modern Physics*, 82(2):1887, 2010.

[18] Jae-Sung Kim, Lihua He, and John J. Lemasters. Mitochondrial permeability transition: a common pathway to necrosis and apoptosis. *Biochemical and Biophysical Research Communications*, 304(3):463 – 470, 2003.

[19] Katherine M. Tyner, Raoul Kopelman, and Martin A. Philbert. " Nanosized voltmeter" enables cellular-wide electric field mapping. *Biophysical Journal*, 93(4):1163 – 1174, 2007.

[20] Joseph C. Ojingwa and R. Rivkah Isseroff. Electrical stimulation of wound healing. *Journal of Investigative Dermatology*, 121(1):1 – 12, 2003.

[21] B. E. Conway. Electrochemical supercapacitors: Scientific fundamentals and technological applications,. *Plenum Press, New York*, 1999.

[22] Frdric Reymond, David Fermn, Hye Jin Lee, and Hubert H. Girault. Electrochemistry at liquid/liquid interfaces: methodology and potential applications. *Electrochimica Acta*, 45(1516):2647 – 2662, 2000.

[23] Mark A. Shannon, Paul W. Bohn, Menachem Elimelech, John G. Georgiadis, Benito J. Marinas, and Anne M. Mayes. Science and technology for water purification in the coming decades. *Nature*, 452(7185):301–310, 03 2008.

[24] J. F. Hester, P. Banerjee, Y.-Y. Won, A. Akthakul, M. H. Acar, and A. M. Mayes. ATRP of amphiphilic graft copolymers based on PVDF and their use as membrane additives. *Macromolecules*, 35(20):7652–7661, 2002.

[25] Dwight S. Seferos, David A. Giljohann, Haley D. Hill, Andrew E. Prigodich, and Chad A. Mirkin. Nano-flares: probes for transfection and mrna detection in living cells. *Journal of the American Chemical Society*, 129(50):15477–15479, 2007. PMID: 18034495.

[26] Jos W. Zwanikken, Peijun Guo, Chad A. Mirkin, and Monica Olvera de la Cruz. Local ionic environment around polyvalent nucleic acid-functionalized nanoparticles. *The Journal of Physical Chemistry C*, 115(33):16368–16373, 2011.

[27] Ceclia Leal, Nathan F. Bouxsein, Kai K. Ewert, and Cyrus R. Safinya. Highly efficient gene silencing activity of sirna embedded in a nanostructured gyroid cubic lipid matrix. *Journal of the American Chemical Society*, 132(47):16841–16847, 2010. PMID: 21028803.

[28] Ralph H. Colby. Polyelectrolyte gels: Ionic partners split up. *Nature Materials*, 6(6):401–402, 06 2007.

[29] Wolfgang H. Meyer. Polymer electrolytes for lithium-ion batteries. *Advanced Materials*, 10(6):439–448, 1998.

[30] Shrayesh N. Patel, Anna E. Javier, Greg M. Stone, Scott A. Mullin, and Nitash P. Balsara. Simultaneous conduction of electronic charge and lithium ions in block copolymers. *ACS Nano*, 6(2):1589–1600, 2012. PMID: 22324447.

[31] Masashi Kawasaki and Yoshihiro Iwasa. Electronics: ”cut and stick” ion gels. *Nature*, 489(7417):510–511, 09 2012.

[32] Keun Hyung Lee, Moon Sung Kang, Sipei Zhang, Yuanyan Gu, Timothy P. Lodge, and C. Daniel Frisbie. cut and stick rubbery ion gels as high capacitance gate dielectrics. *Advanced Materials*, 24(32):4457–4462, 2012.

[33] Per Linse. Electrostatics in the presence of spherical dielectric discontinuities. *The Journal of Chemical Physics*, 128(21):214505, 2008.

[34] Mark J. Stevens. Simple simulations of DNA condensation. *Biophysical Journal*, 80(1):130–139, 2001.

[35] S. Liu and M. Muthukumar. Langevin dynamics simulation of counterion distribution around isolated flexible polyelectrolyte chains. *The Journal of Chemical Physics*, 116(22):9975–9982, 2002.

[36] Qi Liao, Andrey V. Dobrynin, and Michael Rubinstein. Molecular dynamics simulations of polyelectrolyte solutions: osmotic coefficient and counterion condensation. *Macromolecules*, 36(9):3399–3410, 2003.

[37] Markus Deserno, Felipe Jimnez-ngeles, Christian Holm, and Marcelo Lozada-Cassou. Overcharging of DNA in the presence of salt: theory and simulation. *The Journal of Physical Chemistry B*, 105(44):10983–10991, 2001.

[38] Francisco J. Solis and Monica Olvera De La Cruz. Collapse of flexible polyelectrolytes in multivalent salt solutions. *Journal of Chemical Physics*, 112(4):2030–2035, 1 2000.

[39] Yan Levin. Criticality in strongly correlated fluids. *Journal of Physics: Condensed Matter*, 14(9):2303, 2002.

[40] E. Raspaud, M. Olvera de la Cruz, J.L. Sikorav, and F. Livolant. Precipitation of DNA by polyamines: a polyelectrolyte behavior. *Biophys J*, 74(1):381–93, 1998.

[41] Arindam Kundagrami and M. Muthukumar. Theory of competitive counterion adsorption on flexible polyelectrolytes: Divalent salts. *The Journal of Chemical Physics*, 128(24), 2008.

[42] Vikram Jadhao, Francisco J. Solis, and Monica Olvera de la Cruz. Simulation of charged systems in heterogeneous dielectric media via a true energy functional. *Phys. Rev. Lett.*, 109:223905, Nov 2012.

[43] Alexandre P. dos Santos and Yan Levin. Electrolytes between dielectric charged surfaces: Simulations and theory. *The Journal of Chemical Physics*, 142(19):–, 2015.

[44] Jos W. Zwanikken and Monica Olvera de la Cruz. Correlated electrolyte solutions and ion-induced attractions between nanoparticles. *Phys. Rev. E*, 82:050401, Nov 2010.

[45] Vikram Jadhao, Francisco J. Solis, and Monica Olvera de la Cruz. A variational formulation of electrostatics in a medium with spatially varying dielectric permittivity. *The Journal of Chemical Physics*, 138(5):054119, 2013.

[46] R. Kjellander and S. Marcělja. Correlation and image charge effects in electric double layers. *Chemical physics letters*, 112(1):49–53, 1984.

[47] R. Kjellander and S. Marčelja. Inhomogeneous coulomb fluids with image interactions between planar surfaces. i. *The Journal of chemical physics*, 82(4):2122–2135, 1985.

[48] Eriko Sato Matsuo and Toyoichi Tanaka. Patterns in shrinking gels. *Nature*, 358(6386):482–485, 08 1992.

[49] Fumiyoshi Ikkai and Mitsuhiro Shibayama. Gel-size dependence of temperature-induced microphase separation in weakly-charged polymer gels. *Polymer*, 48(8):2387–2394, 2007.

[50] Fumiyoshi Ikkai, Takuya Suzuki, Takeshi Karino, and Mitsuhiro Shibayama. Microstructure of n-isopropylacrylamideacrylic acid copolymer gels having different spatial configurations of weakly charged groups. *Macromolecules*, 40(4):1140–1146, 2007.

[51] Juan Jose Lietor-Santos, Benjamin Sierra-Martin, Urs Gasser, and Alberto Fernandez-Nieves. The effect of hydrostatic pressure over the swelling of microgel particles. *Soft Matter*, 7:6370–6374, 2011.

[52] Murat Guvendiren and Kenneth R. Shull. Self-assembly of acrylic triblock hydrogels by vapor-phase solvent exchange. *Soft Matter*, 3:619–626, 2007.

[53] S. K. De, N. R. Aluru, B. Johnson, W. C. Crone, D. J. Beebe, and J. Moore. Equilibrium swelling and kinetics of ph-responsive hydrogels: models, experiments, and simulations. *Journal of Microelectromechanical Systems*, 11(5):544–555, Oct 2002.

[54] David J. Beebe, Jeffrey S. Moore, Joseph M. Bauer, Qing Yu, Robin H. Liu, Chelladurai Devadoss, and Byung-Ho Jo. Functional hydrogel structures for autonomous flow control inside microfluidic channels. *Nature*, 404(6778):588–590, 04 2000.

[55] Toyochi Tanaka, Izumi Nishio, Shao-Tang Sun, and Shizue Ueno-Nishio. Collapse of gels in an electric field. *Science*, 218(4571):467–469, 1982.

[56] Lisa H. Pope, Chee Xiong, and John F. Marko. Proteolysis of mitotic chromosomes induces gradual and anisotropic decondensation correlated with a reduction of elastic modulus and structural sensitivity to rarely cutting restriction enzymes. *Molecular Biology of the Cell*, 17(1):104–113, 2006.

[57] Guang Feng, Rui Qiao, Jingsong Huang, Bobby G. Sumpter, and Vincent Meunier. Ion distribution in electrified micropores and its role in the anomalous enhancement of capacitance. *ACS Nano*, 4(4):2382–2390, 2010. PMID: 20364850.

[58] Hctor D. Abrua, Yasuyuki Kiya, and Jay C. Henderson. Batteries and electrochemical capacitors. *Physics Today*, 61(12):43, 2008.

[59] Tom Vander Hoogerstraete, Sil Wellens, Katrien Verachtert, and Koen Binnemans. Removal of transition metals from rare earths by solvent extraction with an undiluted phosphonium ionic liquid: separations relevant to rare-earth magnet recycling. *Green Chem.*, 15:919–927, 2013.

[60] Matej Kanduč, Ali Naji, Jan Forsman, and Rudolf Podgornik. Attraction between neutral dielectrics mediated by multivalent ions in an asymmetric ionic fluid. *The Journal of Chemical Physics*, 137(17):–, 2012.

[61] Zhen-Gang Wang. Variational electrostatics for charge solvation. *Journal of Theoretical and Computational Chemistry*, 07(03):397–419, 2008.

[62] Markus Bier, Jos Zwanikken, and René van Roij. Liquid-liquid interfacial tension of electrolyte solutions. *Phys. Rev. Lett.*, 101:046104, Jul 2008.

[63] Guangming Luo, Sarka Malkova, Jaesung Yoon, David G. Schultz, Binhua Lin, Mati Meron, Ilan Benjamin, Petr Vansek, and Mark L. Schlossman. Ion distributions near a liquid-liquid interface. *Science*, 311(5758):216–218, 2006.

[64] John R. Miller and Patrice Simon. Electrochemical capacitors for energy management. *Science*, 321(5889):651–652, 2008.

[65] Rui Wang and Zhen-Gang Wang. Effects of image charges on double layer structure and forces. *The Journal of Chemical Physics*, 139(12), 2013.

[66] Yasuya Nakayama and David Andelman. Differential capacitance of the electric double layer: The interplay between ion finite size and dielectric decrement. *The Journal of chemical physics*, 142(4):044706, 2015.

[67] Rosalind Allen, Jean-Pierre Hansen, and Simone Melchionna. Electrostatic potential inside ionic solutions confined by dielectrics: a variational approach. *Phys. Chem. Chem. Phys.*, 3:4177–4186, 2001.

[68] Jörg Rottler and A. C. Maggs. Local molecular dynamics with coulombic interactions. *Phys. Rev. Lett.*, 93(17):170201, Oct 2004.

[69] Dezsö Boda, Dirk Gillespie, Wolfgang Nonner, Douglas Henderson, and Bob Eisenberg. Computing induced charges in inhomogeneous dielectric media: Application in a Monte Carlo simulation of complex ionic systems. *Phys. Rev. E*, 69(4):046702, Apr 2004.

[70] Alexandre P. dos Santos, Amin Bakhshandeh, and Yan Levin. Effects of the dielectric discontinuity on the counterion distribution in a colloidal suspension. *The Journal of Chemical Physics*, 135(4):044124, 2011.

[71] Zecheng Gan, Huanxin Wu, Kipton Barros, Zhenli Xu, and Erik Luijten. Comparison of efficient techniques for the simulation of dielectric objects in electrolytes. *Journal of Computational Physics*, 291(0):317 – 333, 2015.

[72] Mingge Deng and George Em Karniadakis. Electrostatic correlations near charged planar surfaces. *The Journal of Chemical Physics*, 141(9):–, 2014.

[73] Robin A. Curtis and Leo Lue. Depletion forces due to image charges near dielectric discontinuities. *Current Opinion in Colloid and Interface Science*, 20(1):19 – 23, 2015.

[74] MM Hatlo, RHHG Van Roij, and L Lue. The electric double layer at high surface potentials: The influence of excess ion polarizability. *EPL (Europhysics Letters)*, 97(2):28010, 2012.

[75] Roland R Netz and Henri Orland. Beyond poisson-boltzmann: Fluctuation effects and correlation functions. *The European Physical Journal E*, 1(2-3):203–214, 2000.

[76] Roland Kjellander and Stjepan Marčelja. Electrolyte solutions between uncharged walls. *Chemical physics letters*, 142(6):485–491, 1987.

[77] Erik Wernersson, Roland Kjellander, and Johannes Lyklema. Charge inversion and ion- ion correlation effects at the mercury/aqueous mgso4 interface: Toward the solution of a long-standing issue. *The Journal of Physical Chemistry C*, 114(4):1849–1866, 2010.

[78] Johannes Lyklema. Simple hofmeister series. *Chemical Physics Letters*, 467(4):217–222, 2009.

[79] J. Lyklema. Quest for ion–ion correlations in electric double layers and overcharging phenomena. *Advances in colloid and interface science*, 147:205–213, 2009.

[80] Christophe Labbez, Bo Jonsson, Michal Skarba, and Michal Borkovec. Ion- ion correlation and charge reversal at titrating solid interfaces. *Langmuir*, 25(13):7209–7213, 2009.

[81] R. Car and M. Parrinello. Unified approach for molecular dynamics and density-functional theory. *Phys. Rev. Lett.*, 55(22):2471–2474, Nov 1985.

[82] Adrian Parsegian. Energy of an ion crossing a low dielectric membrane: solutions to four relevant electrostatic problems. *Nature*, 221(5183):844–846, 1969.

[83] G. M. Torrie and J. P. Valleau. Electrical double layers. i. Monte Carlo study of a uniformly charged surface. *The Journal of Chemical Physics*, 73(11):5807–5816, 1980.

[84] Dezs Boda, Kwong-Yu Chan, and Douglas Henderson. Monte Carlo simulation of an ion-dipole mixture as a model of an electrical double layer. *The Journal of Chemical Physics*, 109(17):7362–7371, 1998.

[85] Guillermo Iván Guerrero-García, Yufei Jing, and Monica Olvera de la Cruz. Enhancing and reversing the electric field at the oil-water interface with size-asymmetric monovalent ions. *Soft Matter*, 9:6046–6052, 2013.

[86] Jean-Paul Ryckaert, Giovanni Ciccotti, and Herman J.C Berendsen. Numerical integration of the cartesian equations of motion of a system with constraints: molecular dynamics of n-alkanes. *Journal of Computational Physics*, 23(3):327 – 341, 1977.

[87] J.P. Hansen, G.M. Torrie, and P. Vieillefosse. Statistical mechanics of dense ionized matter. vii. equation of state and phase separation of ionic mixtures in a uniform background. *Physical Review A*, 16(5):2153–2168, 1977.

[88] R. Kjellander, T. Åkesson, B. Jönsson, and S. Marčelja. Double layer interactions in mono- and divalent electrolytes: A comparison of the anisotropic HNC theory and Monte Carlo simulations. *The Journal of chemical physics*, 97:1424, 1992.

[89] V. Boţan, F. Pesth, T. Schilling, and M. Oettel. Hard-sphere fluids in annular wedges: Density distributions and depletion potentials. *Physical Review E*, 79(6):061402, 2009.

[90] Simon Lang, Vitalie Boţan, Martin Oettel, David Hajnal, Thomas Franosch, and Rolf Schilling. Glass transition in confined geometry. *Physical review letters*, 105(12):125701, 2010.

[91] E.J.W. Verwey and K.F. Niessen. Xl. The electrical double layer at the interface of two liquids. *The London, Edinburgh, and Dublin Philosophical Magazine and Journal of Science*, 28(189):435–446, 1939.

[92] Oliver J Lanning and Paul A Madden. Screening at a charged surface by a molten salt. *The Journal of Physical Chemistry B*, 108(30):11069–11072, 2004.

[93] Alexei A Kornyshev. Double-layer in ionic liquids: paradigm change? *The Journal of Physical Chemistry B*, 111(20):5545–5557, 2007.

[94] S. L. Carnie and G. M. Torrie. The statistical mechanics of the electrical double layer. *Advances in Chemical Physics*, 56:141–253, 1984.

[95] Itamar Borukhov, David Andelman, and Henri Orland. Steric effects in electrolytes: A modified poisson-boltzmann equation. *Phys. Rev. Lett.*, 79:435–438, Jul 1997.

[96] Erik Wernersson and Roland Kjellander. Ion correlation forces between uncharged dielectric walls. *The Journal of chemical physics*, 129(14):144701, 2008.

[97] G. M. Torrie, J. P. Valleau, and C. W. Outhwaite. Electrical double layers. vi. image effects for divalent ions. *The Journal of Chemical Physics*, 81(12):6296–6300, 1984.

[98] Amin Bakhshandeh, Alexandre P. dos Santos, and Yan Levin. Weak and strong coupling theories for polarizable colloids and nanoparticles. *Phys. Rev. Lett.*, 107:107801, Sep 2011.

[99] Jos W. Zwanikken, Yufei Jing, Vikram Jadhao, and Monica Olvera de la Cruz. *In preparation*.

[100] B. W. Ninham. On progress in forces since the DLVO theory. *Advances in Colloid and Interface Science*, 83(1):1–17, 1999.

[101] Laurence Ramos, T. C. Lubensky, Nily Dan, Philip Nelson, and D. A. Weitz. Surfactant-mediated two-dimensional crystallization of colloidal crystals. *Science*, 286(5448):2325–2328, 1999.

[102] Eduardo Sanz, Kathryn A. White, Paul S. Clegg, and Michael E. Cates. Colloidal gels assembled via a temporary interfacial scaffold. *Phys. Rev. Lett.*, 103:255502, Dec 2009.

[103] Debabrata Patra, Amitav Sanyal, and Vincent M. Rotello. Colloidal microcapsules: Self-assembly of nanoparticles at the liquidliquid interface. *Chemistry An Asian Journal*, 5(12):2442–2453, 2010.

[104] Risa Matsui, Toru Sakaki, and Toshiyuki Osakai. Label-free amperometric detection of albumin with an oil/water-type flow cell for urine protein analysis. *Electroanalysis*, 24(5):1164–1169, 2012.

[105] Yan Levin. Electrostatic correlations: from plasma to biology. *Reports on Progress in Physics*, 65(11):1577, 2002.

[106] R. Messina, E. Gonzlez-Tovar, M. Lozada-Cassou, and C. Holm. Overcharging: The crucial role of excluded volume. *EPL (Europhysics Letters)*, 60(3):383, 2002.

[107] J. D. Jackson. *Classical Electrodynamics*. Wiley, New York, 3 edition, 1999.

[108] Qizhi Cui, Guoyi Zhu, and Erkang Wang. The application of the mpb4 theory to the interface between two immiscible electrolyte solutions. 2. the differential capacitance of the water — 1,2-dichloroethane interface. *Journal of Electroanalytical Chemistry*, 383(1):7 – 12, 1995.

[109] C.W. Monroe, M. Urbakh, and A.A. Kornyshev. Understanding the anatomy of capacitance at interfaces between two immiscible electrolytic solutions. *Journal of Electroanalytical Chemistry*, 582(12):28 – 40, 2005.

[110] Dmitry Momotenko, Carlos M. Pereira, and Hubert H. Girault. Differential capacitance of liquid/liquid interfaces of finite thicknesses: a finite element study. *Phys. Chem. Chem. Phys.*, 14:11268–11272, 2012.

[111] Guillermo Iván Guerrero-García, Enrique González-Tovar, and Monica Olvera de la Cruz. Effects of the ionic size-asymmetry around a charged nanoparticle: unequal charge neutralization and electrostatic screening. *Soft Matter*, 6:2056–2065, 2010.

[112] Zhi-yong Wang and Yu-qiang Ma. Insights from monte carlo simulations on charge inversion of planar electric double layers in mixtures of asymmetric electrolytes. *The Journal of Chemical Physics*, 133(6), 2010.

[113] K. Besteman, M. A. G. Zevenbergen, H. A. Heering, and S. G. Lemay. Direct observation of charge inversion by multivalent ions as a universal electrostatic phenomenon. *Phys. Rev. Lett.*, 93:170802, Oct 2004.

[114] Frank H. J. van der Heyden, Derek Stein, Koen Besteman, Serge G. Lemay, and Cees Dekker. Charge inversion at high ionic strength studied by streaming currents. *Phys. Rev. Lett.*, 96:224502, Jun 2006.

[115] Yizhak Marcus. Ionic radii in aqueous solutions. *Chemical Reviews*, 88(8):1475–1498, 1988.

[116] J. Koryta, P. Vansek, and M. Bezina. Electrolysis with electrolyte dropping electrode. *Journal of Electroanalytical Chemistry and Interfacial Electrochemistry*, 75(1):211 – 228, 1977.

[117] Wolfgang Schmickler and Elizabeth Santos. *Interfacial Electrochemistry*. Springer Berlin Heidelberg, 2010.

[118] Guillermo Iván Guerrero-García and Monica Olvera de la Cruz. Inversion of the electric field at the electrified liquidliquid interface. *Journal of Chemical Theory and Computation*, 9(1):1–7, 2013. PMID: 26589006.

[119] Erik Wernersson, Roland Kjellander, and Johannes Lyklema. Charge inversion and ionion correlation effects at the mercury/aqueous mgso4 interface: Toward the solution of a long-standing issue. *The Journal of Physical Chemistry C*, 114(4):1849–1866, 2010.

[120] Alexander G . Volkov. *Liquid Interfaces In Chemical, Biological And Pharmaceutical Applications*. CRC Press, 2001.

[121] B I H Scott. Electric fields in plants. *Annual Review of Plant Physiology*, 18(1):409–418, 1967.

[122] Nouamane Laanait, Jaesung Yoon, Binyang Hou, Petr Vanysek, Mati Meron, Binhua Lin, Guangming Luo, Ilan Benjamin, and Mark L. Schlossman. Communications: Monovalent ion condensation at the electrified liquid/liquid interface. *The Journal of Chemical Physics*, 132(17), 2010.

[123] Nouamane Laanait, Miroslav Mihaylov, Binyang Hou, Hao Yu, Petr Vansek, Mati Meron, Binhua Lin, Ilan Benjamin, and Mark L. Schlossman. Tuning ion correlations at an electrified soft interface. *Proceedings of the National Academy of Sciences*, 109(50):20326–20331, 2012.

[124] Sandeep Tyagi, Mehmet Suzen, Marcello Sega, Marcia Barbosa, Sofia S. Kantorovich, and Christian Holm. An iterative, fast, linear-scaling method for computing induced charges on arbitrary dielectric boundaries. *The Journal of Chemical Physics*, 132(15):154112, 2010.

[125] Michael T. Pope and Achim Mller. Polyoxometalate chemistry: An old field with new dimensions in several disciplines. *Angewandte Chemie International Edition in English*, 30(1):34–48, 1991.

[126] C. L. Hill. Introduction: polyoxometalatesmulticomponent molecular vehicles to probe fundamental issues and practical problems. *Chemical Reviews*, 98(1):1–2, 1998. PMID: 11851497.

[127] Anna Proust, Rene Thouvenot, and Pierre Gouzerh. Functionalization of polyoxometalates: towards advanced applications in catalysis and materials science. *Chem. Commun.*, pages 1837–1852, 2008.

[128] Daan Frenkel and Berend Smit. *Understanding Molecular Simulation*. Academic Press, 2 edition, 2001.

[129] In-Chul Yeh and Max L. Berkowitz. Ewald summation for systems with slab geometry. *The Journal of Chemical Physics*, 111(7):3155–3162, 1999.

[130] Yufei Jing, Vikram Jadhao, Jos W. Zwanikken, and Monica Olvera de la Cruz. Ionic structure in liquids confined by dielectric interfaces. *The Journal of Chemical Physics*, 143(19), 2015.

[131] Y. Mao, M.E. Cates, and H.N.W. Lekkerkerker. Depletion force in colloidal systems. *Physica A: Statistical Mechanics and its Applications*, 222(1):10 – 24, 1995.

[132] Guillermo Iván Guerrero-García and Monica Olvera de la Cruz. Polarization effects of dielectric nanoparticles in aqueous charge-asymmetric electrolytes. *The Journal of Physical Chemistry B*, 118(29):8854–8862, 2014. PMID: 24953671.

[133] Reto B. Schoch, Jongyoon Han, and Philippe Renaud. Transport phenomena in nanofluidics. *Rev. Mod. Phys.*, 80:839–883, Jul 2008.

[134] W. Sparreboom, A. van den Berg, and J. C. T. Eijkel. Principles and applications of nanofluidic transport. *Nat Nano*, 4(11):713–720, Nov 2009.

[135] JanC.T. Eijkel and Albertvanden Berg. Nanofluidics: what is it and what can we expect from it? *Microfluidics and Nanofluidics*, 1(3):249–267, 2005.

[136] H. Chang, F. Kosari, G. Andreadakis, M. A. Alam, G. Vasmatzis, and R. Bashir. Capillarity induced negative pressure of water plugs in nanochannels. *Nano Letters*, 3(11):1537–1540, 2003.

[137] Derek Stein, Maarten Kruithof, and Cees Dekker. Surface-charge-governed ion transport in nanofluidic channels. *Phys. Rev. Lett.*, 93:035901, Jul 2004.

[138] Rohit Karnik, Rong Fan, Min Yue, Deyu Li, Peidong Yang, and Arun Majumdar. Electrostatic control of ions and molecules in nanofluidic transistors. *Nano Letters*, 5(5):943–948, 2005. PMID: 15884899.

[139] Mario Tagliazucchi and Igal Szleifer. Salt pumping by voltage-gated nanochannels. *The Journal of Physical Chemistry Letters*, 6(18):3534–3539, 2015.

[140] Han J. and Craighead H. G. Separation of long dna molecules in a microfabricated entropic trap array. *Science*, 288:1026, 2000.

[141] Mathieu Foquet, Jonas Korlach, Warren Zipfel, Watt W. Webb, and Harold G. Craighead. Dna fragment sizing by single molecule detection in submicrometer-sized closed fluidic channels. *Anal. Chem.*, 74:1415, 2002.

[142] John J. Kasianowicz, Eric Brandin, Daniel Branton, and David W. Deamer. Characterization of individual polynucleotide molecules using a membrane channel. *Proc. Natl. Acad. Sci. U.S.A.*, 93:13770, 1996.

[143] Jiali Li, Derek Stein, Ciaran McMullan, Daniel Branton, Michael J. Aziz, and Jene A. Golovchenko. Ion-beam sculpting at nanometre length scales. *Nature*, 412:166, 2001.

[144] H. Chang, F. Kosari, G. Andreadakis, M. A. Alam, G. Vasmatzis, and R. Bashir. Dna-mediated fluctuations in ionic current through silicon oxide nanopore channels. *Nano. Lett.*, 4:1551, 2004.

[145] Daniel Branton, David W Deamer, Andre Marziali, Hagan Bayley, Steven A Benner, Thomas Butler, Massimiliano Di Ventra, Slaven Garaj, Andrew Hibbs, Xiaohua Huang,

Stevan B Jovanovich, Predrag S Krstic, Stuart Lindsay, Xinsheng Sean Ling, Carlos H Mastrangelo, Amit Meller, John S Oliver, Yuriy V Pershin, J Michael Ramsey, Robert Riehn, Gautam V Soni, Vincent Tabard-Cossa, Meni Wanunu, Matthew Wiggin, and Jeffery A Schloss. The potential and challenges of nanopore sequencing. *Nat Biotech*, 26(10):1146–1153, 10 2008.

[146] Jason K. Holt, Hyung Gyu Park, Yinmin Wang, Michael Stadermann, Alexander B. Artyukhin, Costas P. Grigoropoulos, Aleksandr Noy, and Olgica Bakajin. Fast mass transport through sub-2-nanometer carbon nanotubes. *Science*, 312(5776):1034–1037, 2006.

[147] Sung Jae Kim, Sung Hee Ko, Kwan Hyoung Kang, and Jongyoon Han. Direct seawater desalination by ion concentration polarization. *Nat Nano*, 5(4):297–301, 04 2010.

[148] Hirofumi Daiguji, Peidong Yang, Andrew J. Szeri, and Arun Majumdar. Electrochemomechanical energy conversion in nanofluidic channels. *Nano Letters*, 4(12):2315–2321, 2004.

[149] Wei Guo, Liuxuan Cao, Junchao Xia, FuQiang Nie, Wen Ma, Jianming Xue, Yanlin Song, Daoben Zhu, Yugang Wang, and Lei Jiang. Energy harvesting with single-ion-selective nanopores: A concentration-gradient-driven nanofluidic power source. *Advanced Functional Materials*, 20(8):1339–1344, 2010.

[150] Weihua Guan, Sylvia Xin Li, and Mark A Reed. Voltage gated ion and molecule transport in engineered nanochannels: theory, fabrication and applications. *Nanotechnology*, 25(12):122001, 2014.

APPENDIX A

Energy functional employed in the CPMD simulation

Our CPMD simulation scheme is based on the variational functional shown in Eq. (2.1) and rewritten below:

$$\begin{aligned} I[\omega] = & \frac{1}{2}\iint \rho_{\mathbf{r}} G_{\mathbf{r},\mathbf{r}'}\left(\rho_{\mathbf{r}'} + \Omega_{\mathbf{r}'}[\omega]\right) \mathrm{d}\mathbf{r}'\mathrm{d}\mathbf{r} \\ & - \frac{1}{2}\iint \Omega_{\mathbf{r}}[\omega] G_{\mathbf{r},\mathbf{r}'}\left(\omega_{\mathbf{r}'} - \Omega_{\mathbf{r}'}[\omega]\right) \mathrm{d}\mathbf{r}'\mathrm{d}\mathbf{r}. \end{aligned} \tag{A.1}$$

Here ρ and ω are the free and induced charge densities respectively. As noted earlier, $G(\mathbf{r}, \mathbf{r}')$ is the Green's function given by

$$G(\mathbf{r}, \mathbf{r}') = |\mathbf{r} - \mathbf{r}'|^{-1} \tag{A.2}$$

and Ω is

$$\Omega_{\mathbf{r}}[\omega] = \nabla \cdot \left(\chi_{\mathbf{r}} \nabla \int G_{\mathbf{r},\mathbf{r}'}\left(\rho_{\mathbf{r}'} + \omega_{\mathbf{r}'}\right) \mathrm{d}\mathbf{r}' \right), \tag{A.3}$$

where $\chi(\mathbf{r}) = (\epsilon(\mathbf{r}) - 1)/4\pi$ is the dielectric susceptibility and $\epsilon(\mathbf{r})$ is the permittivity at position $\mathbf{r}$ which in general is spatially dependent.

A.1. One interface case

In this section, we show the form of the above functional for the particular case of piecewise-uniform dielectric media with one dielectric interface. Interface separates the dielectric region $\mathcal{R}_1$ with permittivity ϵ_1 from the region $\mathcal{R}_2$ with permittivity ϵ_2. In other words, the dielectric profile

is given by

$$\epsilon(\mathbf{r}) = \epsilon_1 \qquad \mathbf{r} \in \mathcal{R}_1$$

$$= \epsilon_2 \qquad \mathbf{r} \in \mathcal{R}_2 \tag{A.4}$$

The case of planar interfaces, which we analyze in our simulations, then becomes a special case of the functional derived below for the above dielectric profile. We first introduce some notations. We define ϵ_d, and ϵ_m as:

$$\epsilon_m = \frac{\epsilon_1 + \epsilon_2}{2}, \epsilon_d \qquad = \frac{\epsilon_2 - \epsilon_1}{4\pi}, \tag{A.5}$$

ϵ_m represents the mean of the dielectric permittivities on either side of an interface and ϵ_d stores the amount of dielectric contrast at the interface. We denote $\hat{n}\left(\mathbf{s}_i\right)$ as the normal vector at $\mathbf{s}_i$ where $\mathbf{s}$ denotes the position vector of a point on the interface.

In order to express $I[\omega]$ in a more compact and physically clear way we first introduce two operators:

$$\mathcal{G}\left(\mathbf{a}, \mathbf{b}\right) = \int G(\mathbf{a}, \mathbf{s}) \hat{n}\left(\mathbf{s}\right) \cdot \nabla_s G\left(\mathbf{s}, \mathbf{b}\right) d^2 s, \tag{A.6}$$

and

$$\mathscr{G}\left(\mathbf{a}, \mathbf{b}\right) = \iint \hat{n}(\mathbf{s}) \cdot \nabla_s G(\mathbf{a}, \mathbf{s}) G(\mathbf{s}, \mathbf{s}') \hat{n}\left(\mathbf{s}'\right) \cdot \nabla_{s'} G\left(\mathbf{s}', \mathbf{b}\right) d^2 s d^2 s', \tag{A.7}$$

where a and b are position vectors. These operators can be thought of as a kind of renormalized electrostatic interactions between two unit charges mediated via the interface $\mathcal{I}$, just as the Green's function $G(\mathbf{a}, \mathbf{b})$ is the bare electrostatic potential of interaction between two unit charges.

One important thing to note here. The bare Green's function $G(\mathbf{a},\mathbf{b})$ is symmetric in its variables, i.e, $G(\mathbf{a},\mathbf{b}) = G(\mathbf{b},\mathbf{a})$. The same is not true for the function $\mathcal{G}(\mathbf{a},\mathbf{b})$. A simple glance at equation (A.6) confirms that in general

$$\mathcal{G}(\mathbf{a},\mathbf{b}) \neq \mathcal{G}(\mathbf{b},\mathbf{a}). \tag{A.8}$$

Looking at equations (1.10) we see that the energy functional is comprised of energies coming from three separate sources of interaction: the interaction energy between free charges (the $\rho(\mathbf{r})\ldots\rho(\mathbf{r}')$ terms), the interaction energy between free charges and induced charges (the $\rho(\mathbf{r})\ldots\omega(\mathbf{s})$ terms), and the interaction energy between induced charges (the $\omega(\mathbf{s})\ldots\omega(\mathbf{s}')$ terms).

Using the dielectric profile of Eq. (A.4) and the definitions of G and Ω from Eqs. (A.2) and (A.3) in Eq. (A.1), we can reduce $I[\omega]$ to a form that can be written as

(A.9)

$$\begin{aligned} I[\omega] = {} & \frac{1}{2}\iint \rho(\mathbf{r})\left(\frac{1}{\epsilon(\mathbf{r})}G(\mathbf{r},\mathbf{r}') + \frac{\epsilon_d}{\epsilon(\mathbf{r})}\mathcal{G}(\mathbf{r},\mathbf{r}')\frac{1}{\epsilon(\mathbf{r}')} + \frac{\epsilon_d^2}{\epsilon(\mathbf{r})}\mathscr{G}(\mathbf{r},\mathbf{r}')\frac{1}{\epsilon(\mathbf{r}')}\right)\rho(\mathbf{r}')\,d^3r d^3r' \\ & + \frac{1}{2}\iint \rho(\mathbf{r})\left(\left(1-\frac{\epsilon_m}{\epsilon(\mathbf{r})}\right)G(\mathbf{r},\mathbf{s}) - \frac{\epsilon_d(2\epsilon_m-1)}{\epsilon(\mathbf{r})}\mathcal{G}(\mathbf{r},\mathbf{s}) + \frac{\epsilon_d}{\epsilon(\mathbf{r})}\mathcal{G}(\mathbf{s},\mathbf{r}) + \frac{2\epsilon_d^2}{\epsilon(\mathbf{r})}\mathscr{G}(\mathbf{r},\mathbf{s})\right) \\ & \omega(\mathbf{s})\,d^3r d^2s \\ & + \frac{1}{2}\iint \omega(\mathbf{s})\left(\epsilon_m(\epsilon_m-1)G(\mathbf{s},\mathbf{s}') - \epsilon_d(2\epsilon_m-1)\mathcal{G}(\mathbf{s},\mathbf{s}') + \epsilon_d^2\mathscr{G}(\mathbf{s},\mathbf{s}')\right)\omega(\mathbf{s}')\,d^2s d^2s'. \end{aligned}$$

Defining

$$R_{\rho\rho}(\mathbf{r},\mathbf{r}') = \frac{1}{\epsilon(\mathbf{r})}G(\mathbf{r},\mathbf{r}') + \frac{\epsilon_d}{\epsilon(\mathbf{r})}\mathcal{G}(\mathbf{r},\mathbf{r}')\frac{1}{\epsilon(\mathbf{r}')} + \frac{\epsilon_d^2}{\epsilon(\mathbf{r})}\mathscr{G}(\mathbf{r},\mathbf{r}')\frac{1}{\epsilon(\mathbf{r}')}, \tag{A.10}$$

$$R_{\rho\omega}(\mathbf{r},\mathbf{s}) = \left(1-\frac{\epsilon_m}{\epsilon(\mathbf{r})}\right)G(\mathbf{r},\mathbf{s}) - \frac{\epsilon_d(2\epsilon_m-1)}{\epsilon(\mathbf{r})}\mathcal{G}(\mathbf{r},\mathbf{s}) + \frac{\epsilon_d}{\epsilon(\mathbf{r})}\mathcal{G}(\mathbf{s},\mathbf{r}) + \frac{2\epsilon_d^2}{\epsilon(\mathbf{r})}\mathscr{G}(\mathbf{r},\mathbf{s}), \tag{A.11}$$

and

$$R_{\omega\omega}(\mathbf{s},\mathbf{s}') = \epsilon_m\left(\epsilon_m - 1\right) G\left(\mathbf{s},\mathbf{s}'\right) - \epsilon_d\left(2\epsilon_m - 1\right)\mathcal{G}(\mathbf{s},\mathbf{s}') + \epsilon_d^2\mathscr{G}(\mathbf{s},\mathbf{s}'), \tag{A.12}$$

we express the functional for the different dielectric problem in the following compact form:

$$I[\omega] = \frac{1}{2}\iint \rho(\mathbf{r})R_{\rho\rho}(\mathbf{r},\mathbf{r}')\rho(\mathbf{r}')d^3r d^3r' + \frac{1}{2}\iint \rho(\mathbf{r})R_{\rho\omega}(\mathbf{r},\mathbf{s})\omega(\mathbf{s})d^3r d^2s + \frac{1}{2}\iint \omega(\mathbf{s})R_{\omega\omega}(\mathbf{s},\mathbf{s}')\omega(\mathbf{s}')d^2s d^2s'. \tag{A.13}$$

A.2. Two interfaces case

In this section, we show the form of Eq. (A.1) for the particular case of piecewise-uniform dielectric media with two (open) dielectric interfaces denoted as interfaces I and II. Interface I separates the dielectric region $\mathcal{R}_1$ with permittivity ϵ_1 from the region $\mathcal{R}_2$ with permittivity ϵ_2. Interface II separates $\mathcal{R}_2$ from the region $\mathcal{R}_3$ characterized by permittivity ϵ_3. In other words, the dielectric profile is given by

$$\begin{aligned} \epsilon(\mathbf{r}) &= \epsilon_1 \qquad \mathbf{r}\in\mathcal{R}_1 \\ &= \epsilon_2 \qquad \mathbf{r}\in\mathcal{R}_2 \\ &= \epsilon_3 \qquad \mathbf{r}\in\mathcal{R}_3. \end{aligned} \tag{A.14}$$

The case of planar interfaces, which we analyze in our simulations, then becomes a special case of the functional derived below for the above dielectric profile. We first introduce some notations.

We define $\epsilon_{m_{\rm I}}$, $\epsilon_{m_{\rm II}}$, $\epsilon_{d_{\rm I}}$, and $\epsilon_{d_{\rm II}}$ as:

$$\epsilon_{m_{\rm I}} = \frac{\epsilon_1 + \epsilon_2}{2}, \epsilon_{m_{\rm II}} = \frac{\epsilon_3 + \epsilon_2}{2}, \tag{A.15}$$
$$\epsilon_{d_{\rm I}} = \frac{\epsilon_2 - \epsilon_1}{4\pi}, \epsilon_{d_{\rm II}} = \frac{\epsilon_2 - \epsilon_3}{4\pi}.$$

ϵ_m represents the mean of the dielectric permittivities on either side of an interface and ϵ_d stores the amount of dielectric contrast at the interface. We denote $\hat{n}_i(\mathbf{s}_i)$ as the normal vector at $\mathbf{s}_i$ where $\mathbf{s}$ denotes the position vector of a point on the interface i. We will use indices i and j to identify an interface. On interface I the normal vector is chosen to point from $\mathcal{R}_1$ to $\mathcal{R}_2$ and on the interface II it is taken to point from $\mathcal{R}_3$ to $\mathcal{R}_2$. In the particular case of dielectric configuration with planar interfaces that we analyzed in this paper, we have $\mathcal{R}_1 : z \leq -H/2$, $\mathcal{R}_2 : -H/2 \leq z \leq H/2$, and $\mathcal{R}_3 : z \geq H/2$ with $z = -H/2$ plane as interface I and $z = H/2$ plane as interface II. As per our conventions, $\hat{n}_{\rm I}$ points in $(0, 0, 1)$ direction and $\hat{n}_{\rm II}$ points in $(0, 0, -1)$ direction.

Similarly, it is useful to introduce two functions $\mathcal{G}$ and $\mathscr{G}$ which we can be called indirect or renormalized Green's functions and are essentially interaction potentials between a pair of position coordinates. $\mathcal{G}_i$ is defined as

$$\mathcal{G}_i(\mathbf{a}, \mathbf{b}) = \int G(\mathbf{a}, \mathbf{s}_i)\, \hat{n}_i(\mathbf{s}_i) \cdot \nabla_{\mathbf{s}_i} G(\mathbf{s}_i, \mathbf{b})\, \mathrm{d}\mathbf{s}_i \tag{A.16}$$

and $\mathscr{G}_{ij}$ is given by

$$\mathscr{G}_{ij}(\mathbf{a}, \mathbf{b}) = \iint \hat{n}_i(\mathbf{s}_i) \cdot \nabla_{\mathbf{s}_i} G(\mathbf{a}, \mathbf{s}_i)\, G(\mathbf{s}_i, \mathbf{s}_j) \tag{A.17}$$
$$\hat{n}_j(\mathbf{s}_j) \cdot \nabla_{\mathbf{s}_j} G(\mathbf{s}_j, \mathbf{b})\, \mathrm{d}\mathbf{s}_i \mathrm{d}\mathbf{s}_j.$$

In the event of two interfaces (I and II), we have the following possibilities for these functions: $\mathcal{G}_{\rm I}$, $\mathcal{G}_{\rm II}$, $\mathscr{G}_{\rm I,I}$, $\mathscr{G}_{\rm II,II}$, $\mathscr{G}_{\rm I,II}$, and $\mathscr{G}_{\rm II,I}$.

Note that unlike G, $\mathcal{G}_i$ and $\mathscr{G}_{ij}$ are not symmetric, that is $\mathcal{G}_i(\mathbf{a},\mathbf{b}) \neq \mathcal{G}_i(\mathbf{b},\mathbf{a})$ and $\mathscr{G}_{ij}(\mathbf{a},\mathbf{b}) \neq \mathscr{G}_{ij}(\mathbf{b},\mathbf{a})$. Also, $\mathscr{G}_{ij}(\mathbf{a},\mathbf{b}) \neq \mathscr{G}_{ji}(\mathbf{a},\mathbf{b})$ for $i \neq j$. In Eq. (A.17), the self-interaction contributions (when $\mathbf{s}_i = \mathbf{s}_j$) coming from induced charges belonging to the same interface and same location (grid point) are approximated by a suitable analytical integral [**67**].

Using the dielectric profile of Eq. (A.14) and the definitions of G and Ω from Eqs. (A.2) and (A.3) in Eq. (A.1), we can reduce $I[\omega]$ to a form that can be written as

$$
\begin{aligned}
I[\omega] &= \frac{1}{2}\iint \rho(\mathbf{r}) R_{\rho\rho}(\mathbf{r},\mathbf{r}')\rho(\mathbf{r}')\mathrm{d}\mathbf{r}\mathrm{d}\mathbf{r}' + \frac{1}{2}\iint \rho(\mathbf{r}) R_{\rho\omega_{\mathrm{I}}}(\mathbf{r},\mathbf{s})\omega(\mathbf{s})\mathrm{d}\mathbf{r}\mathrm{d}\mathbf{s} \\
&+ \frac{1}{2}\iint \rho(\mathbf{r}) R_{\rho\omega_{\mathrm{II}}}(\mathbf{r},\mathbf{t})\omega(\mathbf{t})\mathrm{d}\mathbf{r}\mathrm{d}\mathbf{t} + \frac{1}{2}\iint \omega(\mathbf{s}) R_{\omega_{\mathrm{I}}\omega_{\mathrm{I}}}(\mathbf{s},\mathbf{s}')\omega(\mathbf{s}')\mathrm{d}\mathbf{s}\mathrm{d}\mathbf{s}' \\
&+ \frac{1}{2}\iint \omega(\mathbf{t}) R_{\omega_{\mathrm{II}}\omega_{\mathrm{II}}}(\mathbf{t},\mathbf{t}')\omega(\mathbf{t}')\mathrm{d}\mathbf{t}\mathrm{d}\mathbf{t}' + \frac{1}{2}\iint \omega(\mathbf{s}) R_{\omega_{\mathrm{I}}\omega_{\mathrm{II}}}(\mathbf{s},\mathbf{t})\omega(\mathbf{t})\mathrm{d}\mathbf{s}\mathrm{d}\mathbf{t},
\end{aligned}
\tag{A.18}
$$

where ω now denotes the surface charge density, and $\mathbf{s}$, $\mathbf{t}$ are position vectors associated with interfaces I and II respectively. Minimizing this functional gives the correct ω on the two interfaces. Below we describe the various R functions appearing in Eq. A.18.

The R functions characterize the effective interaction potential between two charges in different locations. The subscripts in the notation of these functions indicate the location of the charge and also whether it is a free charge or an induced charge. $R_{\rho\rho}$ denotes the effective potential between two free charges and is given by:

$$
\begin{aligned}
R_{\rho\rho}(\mathbf{r},\mathbf{r}') = \frac{1}{\epsilon_{\mathbf{r}'}} G(\mathbf{r},\mathbf{r}') &+ \frac{\epsilon_{d_{\mathrm{I}}}}{\epsilon_{\mathbf{r}}\epsilon_{\mathbf{r}'}}\mathcal{G}_{\mathrm{I}}(\mathbf{r},\mathbf{r}') + \frac{\epsilon_{d_{\mathrm{II}}}}{\epsilon_{\mathbf{r}}\epsilon_{\mathbf{r}'}}\mathcal{G}_{\mathrm{II}}(\mathbf{r},\mathbf{r}') \\
&+ \frac{\epsilon_{d_{\mathrm{I}}}^2}{\epsilon_{\mathbf{r}}\epsilon_{\mathbf{r}'}}\mathscr{G}_{\mathrm{I,I}}(\mathbf{r},\mathbf{r}') + \frac{\epsilon_{d_{\mathrm{II}}}^2}{\epsilon_{\mathbf{r}}\epsilon_{\mathbf{r}'}}\mathscr{G}_{\mathrm{II,II}}(\mathbf{r},\mathbf{r}') \\
&+ \frac{\epsilon_{d_{\mathrm{I}}}\epsilon_{d_{\mathrm{II}}}}{\epsilon_{\mathbf{r}}\epsilon_{\mathbf{r}'}}\mathscr{G}_{\mathrm{I,II}}(\mathbf{r},\mathbf{r}') + \frac{\epsilon_{d_{\mathrm{I}}}\epsilon_{d_{\mathrm{II}}}}{\epsilon_{\mathbf{r}}\epsilon_{\mathbf{r}'}}\mathscr{G}_{\mathrm{II,I}}(\mathbf{r},\mathbf{r}').
\end{aligned}
\tag{A.19}
$$

The first term on the right-hand side of the above equation contains the Green's pair interaction potential. In the evaluation of this term and the associated contribution to the total integral $I[\omega]$ of Eq. (A.18), we assume $\mathbf{r} \neq \mathbf{r}'$. The next two terms involve the first renormalized Green's function $\mathcal{G}$ and the final four terms comprise interactions of the form of $\mathscr{G}$. Note that for the computation of the terms involving $\mathcal{G}$ and $\mathscr{G}$, we take into account the self-terms ($\mathbf{r} = \mathbf{r}'$) as these are well defined. $R_{\rho\omega_{\mathrm{I}}}$ denotes the effective potential between a free charge and the induced charge on interface I and is given as:

$$
\begin{aligned}
R_{\rho\omega_{\mathrm{I}}}(\mathbf{r},\mathbf{s}) = {} & \frac{\epsilon_{\mathbf{r}} - \epsilon_{m_{\mathrm{I}}}}{\epsilon_{\mathbf{r}}} G(\mathbf{r},\mathbf{s}) + \frac{\epsilon_{d_{\mathrm{I}}}}{\epsilon_{\mathbf{r}}} \mathcal{G}_{\mathrm{I}}(\mathbf{r},\mathbf{s}) + \frac{\epsilon_{d_{\mathrm{II}}}}{\epsilon_{\mathbf{r}}} \mathcal{G}_{\mathrm{II}}(\mathbf{r},\mathbf{s}) \\
& - \frac{\epsilon_{d_{\mathrm{I}}}(2\epsilon_{m_{\mathrm{I}}} - 1)}{\epsilon_{\mathbf{r}}} \mathcal{G}_{\mathrm{I}}(\mathbf{s},\mathbf{r}) - \frac{\epsilon_{d_{\mathrm{II}}}(2\epsilon_{m_{\mathrm{I}}} - 1)}{\epsilon_{\mathbf{r}}} \mathcal{G}_{\mathrm{II}}(\mathbf{s},\mathbf{r}) \\
& + \frac{2\epsilon_{d_{\mathrm{I}}}^2}{\epsilon_{\mathbf{r}}} \mathscr{G}_{\mathrm{I,I}}(\mathbf{r},\mathbf{s}) + \frac{2\epsilon_{d_{\mathrm{II}}}^2}{\epsilon_{\mathbf{r}}} \mathscr{G}_{\mathrm{II,II}}(\mathbf{r},\mathbf{s}) \\
& + \frac{2\epsilon_{d_{\mathrm{I}}}\epsilon_{d_{\mathrm{II}}}}{\epsilon_{\mathbf{r}}} \mathscr{G}_{\mathrm{I,II}}(\mathbf{r},\mathbf{s}) + \frac{2\epsilon_{d_{\mathrm{I}}}\epsilon_{d_{\mathrm{II}}}}{\epsilon_{\mathbf{r}}} \mathscr{G}_{\mathrm{II,I}}(\mathbf{r},\mathbf{s}) .
\end{aligned}
\tag{A.20}
$$

Similarly, $R_{\rho\omega_{\mathrm{II}}}$ denotes the effective potential between a free charge and the induced charge on interface II and can be obtained from Eq. (A.20) by swapping I with II and replacing $\mathbf{s}$ with $\mathbf{t}$.

Next we provide the expressions for the functions that represent the effective interactions between the induced charges on the interfaces. The effective interaction potential between two induced charges on interface I, $R_{\omega_{\mathrm{I}}\omega_{\mathrm{I}}}$, is given by

$$
\begin{aligned}
R_{\omega_{\mathrm{I}}\omega_{\mathrm{I}}}(\mathbf{s},\mathbf{s}') = {} & \epsilon_{m_{\mathrm{I}}}(\epsilon_{m_{\mathrm{I}}} - 1) G(\mathbf{s},\mathbf{s}') + \epsilon_{d_{\mathrm{I}}}(1 - 2\epsilon_{m_{\mathrm{I}}}) \mathcal{G}_{\mathrm{I}}(\mathbf{s},\mathbf{s}') \\
& + \epsilon_{d_{\mathrm{II}}}(1 - 2\epsilon_{m_{\mathrm{I}}}) \mathcal{G}_{\mathrm{II}}(\mathbf{s},\mathbf{s}') + \epsilon_{d_{\mathrm{I}}}^2 \mathscr{G}_{\mathrm{I,I}}(\mathbf{s},\mathbf{s}') \\
& + \epsilon_{d_{\mathrm{II}}}^2 \mathscr{G}_{\mathrm{II,II}}(\mathbf{s},\mathbf{s}') + 2\epsilon_{d_{\mathrm{I}}}\epsilon_{d_{\mathrm{II}}} \mathscr{G}_{\mathrm{I,II}}(\mathbf{s},\mathbf{s}') .
\end{aligned}
\tag{A.21}
$$

The evaluation of self-interaction ($\mathbf{s} = \mathbf{s}'$) terms is, as noted earlier, carried out via an analytically computed approximate form. Swapping I and II, and replacing $\mathbf{s}, \mathbf{s}'$ with $\mathbf{t}, \mathbf{t}'$ in Eq. (A.21) leads

to the expression for $R_{\omega_{\text{II}}\omega_{\text{II}}}(\mathbf{t},\mathbf{t}')$. The last term on the right-hand side of Eq. (A.18) involves the effective potential $R_{\omega_{\text{I}}\omega_{\text{II}}}$ which represents the interaction between an induced charge on interface I and an induced charge on interface II. $R_{\omega_{\text{I}}\omega_{\text{II}}}$ is given as:

$$\begin{aligned} R_{\omega_{\text{I}}\omega_{\text{II}}}(\mathbf{s},\mathbf{t}) &= \epsilon_{m_{\text{I}}}\left(\epsilon_{m_{\text{II}}}-1\right)G\left(\mathbf{s},\mathbf{t}\right)+\epsilon_{m_{\text{II}}}\left(\epsilon_{m_{\text{I}}}-1\right)G\left(\mathbf{t},\mathbf{s}\right) \\ &+\epsilon_{d_{\text{I}}}\left(1-2\epsilon_{m_{\text{I}}}\right)\mathcal{G}_{\text{I}}\left(\mathbf{s},\mathbf{t}\right)+\epsilon_{d_{\text{II}}}\left(1-2\epsilon_{m_{\text{I}}}\right)\mathcal{G}_{\text{II}}\left(\mathbf{s},\mathbf{t}\right) \\ &+\epsilon_{d_{\text{I}}}\left(1-2\epsilon_{m_{\text{II}}}\right)\mathcal{G}_{\text{I}}\left(\mathbf{t},\mathbf{s}\right)+\epsilon_{d_{\text{II}}}\left(1-2\epsilon_{m_{\text{II}}}\right)\mathcal{G}_{\text{II}}\left(\mathbf{t},\mathbf{s}\right) \\ &+2\epsilon_{d_{\text{I}}}^{2}\mathscr{G}_{\text{I,I}}\left(\mathbf{s},\mathbf{t}\right)+2\epsilon_{d_{\text{II}}}^{2}\mathscr{G}_{\text{II,II}}\left(\mathbf{s},\mathbf{t}\right) \\ &+2\epsilon_{d_{\text{I}}}\epsilon_{d_{\text{II}}}\mathscr{G}_{\text{I,II}}\left(\mathbf{s},\mathbf{t}\right)+2\epsilon_{d_{\text{I}}}\epsilon_{d_{\text{II}}}\mathscr{G}_{\text{I,II}}\left(\mathbf{t},\mathbf{s}\right). \end{aligned} \tag{A.22}$$